



ATHENA Radiation Environment
Models and X-Ray Background
Effects Simulators

WP1
TN 1.1

Doc No: IASFMi-ATHENA-WP1
Date: 10 February 2017
Page: 1 of 78

AREMBES

ATHENA Radiation Environment Models and X-Ray Background Effects Simulators

ESA's Science Core Technology Programme (CTP)
ESA Contract No. 4000116655/16/NL/BW



WP1 TN 1.1

Radiation Background Data Analysis & Lessons Learned from Previous X-ray Missions

Coordinated by:

Silvano Molendi (IASF-Milano/INAF)

Edited by:

Simona Ghizzardi (IASF-Milano/INAF)
Mariachiara Rossetti (IASF-Milano/INAF)

With contributions from:

Andrea De Luca (IASF-Milano/INAF)
Fabio Gastaldello (IASF-Milano/INAF)
Simona Ghizzardi (IASF-Milano/INAF)
Martino Marelli (IASF-Milano/INAF)
Alberto Moretti (OAB/INAF)
Mariachiara Rossetti (IASF-Milano/INAF)
David Salvetti (IASF-Milano/INAF)
Andrea Tiengo (IUSS Pavia)



ATHENA Radiation Environment Models and X-Ray Background Effects Simulators	WP1 TN 1.1	Doc No: IASFMi-ATHENA-WP1 Date: 10 February 2017 Page: 2 of 78
---	-----------------------------	--



ATHENA Radiation Environment Models and X-Ray Background Effects Simulators	WP1 TN 1.1	Doc No: IASFMi-ATHENA-WP1 Date: 10 February 2017 Page: 3 of 78
---	-----------------------------	--

Contents

1	INTRODUCTION.....	6
2	B0: DATA PRODUCTION AND SELECTION	8
2.1	Introduction	8
2.1.1	XMM-Newton	8
2.1.2	Optical filters	8
2.1.3	XMM-Newton background	9
2.1.4	The aim of B0.....	9
2.2	Data set selection	11
2.2.1	Camera selection	11
2.2.2	Event selection	11
2.2.3	Exposures selection	12
2.3	Basic definitions and inputs	13
2.3.1	Basic definition: in field-of-view (<i>inFOV</i>)	13
2.3.2	Basic definition: out field-of-view (<i>outFOV</i>)	15
2.3.3	Inputs: from XSA and 3XMM to EXTraS.....	15
2.4	Light curves creation.....	15
2.4.1	<i>outFOV</i> / <i>inFOV</i> area rescale.....	15
2.4.2	General Preparation	16
2.4.3	<i>inFOV</i> and <i>outFOV</i> light curves computation	17
2.5	Spectra computation	18
2.6	Image computation	19
3	SPB1: CHARACTERIZING THE FOCUSED PARTICLES BACKGROUND	22
3.1	Introduction	22
3.2	Data preparation	22
3.2.1	Stacking of the data	23
3.2.2	<i>inFOV-outFOV</i> light curves computation	23
3.2.3	The Master SPB1 background file.....	23
3.2.4	Final data set selection	24
3.3	Analysis of the <i>inFOV-outFOV</i> distribution	25
3.3.1	<i>inFOV-outFOV</i> count rate distribution.....	25
3.3.2	Empirical characterization of the <i>inFOV</i> background components	26
3.3.3	<i>inFOV-outFOV</i> distribution as a function of filter	27
3.4	Evaluating systematic effects.....	28



ATHENA Radiation Environment Models and X-Ray Background Effects Simulators	WP1 TN 1.1	Doc No: IASFMi-ATHENA-WP1 Date: 10 February 2017 Page: 4 of 78
---	-----------------------	--

- 3.4.1 *inFOV-outFOV* distribution as a function of time 28
- 3.4.2 Closed exposures analysis 30
- 3.4.3 Discussion 31
- 3.5 Spectral analysis of the low-intensity and the flaring components 32**
- 3.6 Evolution of the flaring and low intensity components through the mission 35**
 - 3.6.1 Extraction of *inFOV-outFOV* count rate distribution per year 35
- 3.7 Summary 35**
- 4 SPB2: IMPACT OF THE MAGNETOSPHERIC ENVIRONMENT ON THE XMM-NEWTON BACKGROUND 37**
- 4.1 Introduction 37**
- 4.2 The dataset 37**
- 4.3 Method 37**
 - 4.3.1 Partition of the magnetosphere into magneto-zones 37
 - 4.3.1.1 Radiation belts: magneto-zone #1 and #2 38
 - 4.3.1.2 Plasma sheet: magneto-zone #3 39
 - 4.3.1.3 Magnetoplasma and magnetotail: magneto-zones #4 and #5 39
 - 4.3.1.4 Magnetosheath: magneto-zone #6 39
 - 4.3.1.5 Out of the bow shock: magneto-zone #7 40
 - 4.3.2 XMM-Newton orbit segmentation 40
- 4.4 Results 44**
 - 4.4.1 Soft protons rate, low-intensity background, and magnetospheric environment 44
 - 4.4.2 Dependence on the XMM-Newton altitude 50
 - 4.4.3 Dependence on the direction: Sunward and anti-Sunward 52
- 4.5 Conclusions 54**
- 5 SPB3: THE ORIGIN OF THE SOFT PROTON COMPONENT 55**
- 5.1 Introduction and data selection 55**
- 5.2 Comparison of the *inFOV-outFOV* MOS2 and ACE EPAM LEMS data 55**
- 5.3 The *inFOV-outFOV* MOS2 and ACE EPAM LEMS data during SEPS 56**
- 5.4 Comparison of the *inFOV-outFOV* MOS2 and ERM data 58**
- 5.5 Conclusions 59**
- 6 SPRD: RADIATION DAMAGE BY SOFT PROTONS 60**
- 6.1 Introduction 60**



ATHENA Radiation Environment Models and X-Ray Background Effects Simulators	WP1 TN 1.1	Doc No: IASFMi-ATHENA-WP1 Date: 10 February 2017 Page: 5 of 78
---	-----------------------	--

6.2 Radiation Damage in Chandra CCDs.....60

6.3 Radiation Damage in XMM-Newton detectors61

6.4 Conclusions.....62

7 UPB1: UNFOCUSED PARTICLE BACKGROUND FROM VARIOUS MISSIONS..... 64

7.1 Introduction64

7.2 Dataset65

7.3 Data comparison65

7.4 Spectral fit66

7.5 Summary67

8 UPB2: THE ORIGIN OF THE UNFOCUSED PARTICLE BACKGROUND 68

8.1 Introduction e data selection.....68

8.2 Dependence on solar cycle69

8.3 Filtering out SEPs and radiation belts71

8.4 Correlation of ERM and *outFOV* MOS2 data72

8.5 Absence of correlation with the magnetospheric environment73

8.6 The mechanism responsible for the instrumental background73

9 UPRD: RADIATION DAMAGE BY UNFOCUSED PARTICLES..... 74

9.1 Introduction74

9.2 Radiation Damage in XMM-Newton detectors74

9.3 Conclusions.....75

10 SUMMARY..... 76

11 REFERENCES..... 77

ATHENA Radiation Environment Models and X-Ray Background Effects Simulators	WP1 TN 1.1	Doc No: IASFMi-ATHENA-WP1 Date: 10 February 2017 Page: 6 of 78
---	-----------------------------	--

1 INTRODUCTION

The goal we wish to achieve within this work package is to characterize the effects of focused and non-focused particles on detectors: both in terms of contributions to their instrumental background and as source of radiation damage. The means by which we plan to achieve this is the analysis of data collected by current X-ray missions.

As will become apparent in the next sections, the bulk of our work has been performed on the XMM-Newton EPIC camera. More specifically we have constructed a dataset from the full mission archive with a total exposure time of roughly 100 Ms, about 2 orders of magnitude larger of those used in previous analysis. This has allowed us to address for the first time, in a statistically meaningful way, some rather important issues such as, for example, the probability distribution of flares over the full XMM-Newton lifetime. A point bearing some recognition is that the construction of our dataset is not a trivial task. Indeed, it has been possible only thanks to the synergy with EXTraS (Exploring the X-ray Transient and variable Sky), a project within the EU-FP7 framework. EXTraS, which like WP1 is led by IASF-Milano/INAF, has performed an analysis of the full XMM-Newton EPIC archive to search for X-ray transient and variable sources and, with relatively little work, it has been possible to adapt its reduction pipeline to produce our dataset. Another feature of the work presented here is that it has been performed by a relatively large number of people: we have a total of 9 team members and 6 sub-work-package leaders.

The work has been divided between focused and un-focused particle background and for each species of particles there have been 2 sets of activities: one dedicated to background characterization, the other to radiation damage. Each set has been addressed in one or more sub-work-packages, for a total of 8 distinct units, see Figure 1.1 for a schematic representation.

The remainder of this document is structured as follows. In Section 2 (sub-WP B0) we provide a detailed description of the reduction of the archival EPIC data that has been adopted to produce our background dataset. In Sections 3 to 5 we concentrate on the focused background component, more specifically in Section 3 (sub-WP SPB1) we provide a general chrono-spectral description of this component over the full mission timeline. In Section 4 (sub-WP SPB2) we search for correlations between it and the Earth magnetospheric environment and, in Section 5 (sub-WP SPB3), we attempt to relate measurements of particle fluxes by dedicated detectors with measurements made with EPIC onboard XMM-Newton. In Section 6 (sub-WP SPRD) we discuss the contribution of low energy protons, which can be focused by the mirrors, to the radiation damage incurred by X-ray detectors. In Sections 7 and 8 we concentrate on the non-focused background component, more specifically in Section 7 (sub-WP UPB1) we review the contribution of this component to several existing X-ray mission, while in Section 8 (sub-WP UPB2) we perform and in depth analysis of XMM-Newton data. In Section 9 (sub-WP UPRD) we address the role played by the non-focused penetrating component in producing radiation damage in X-ray detectors. Finally, in Section 10, we summarize our main findings.

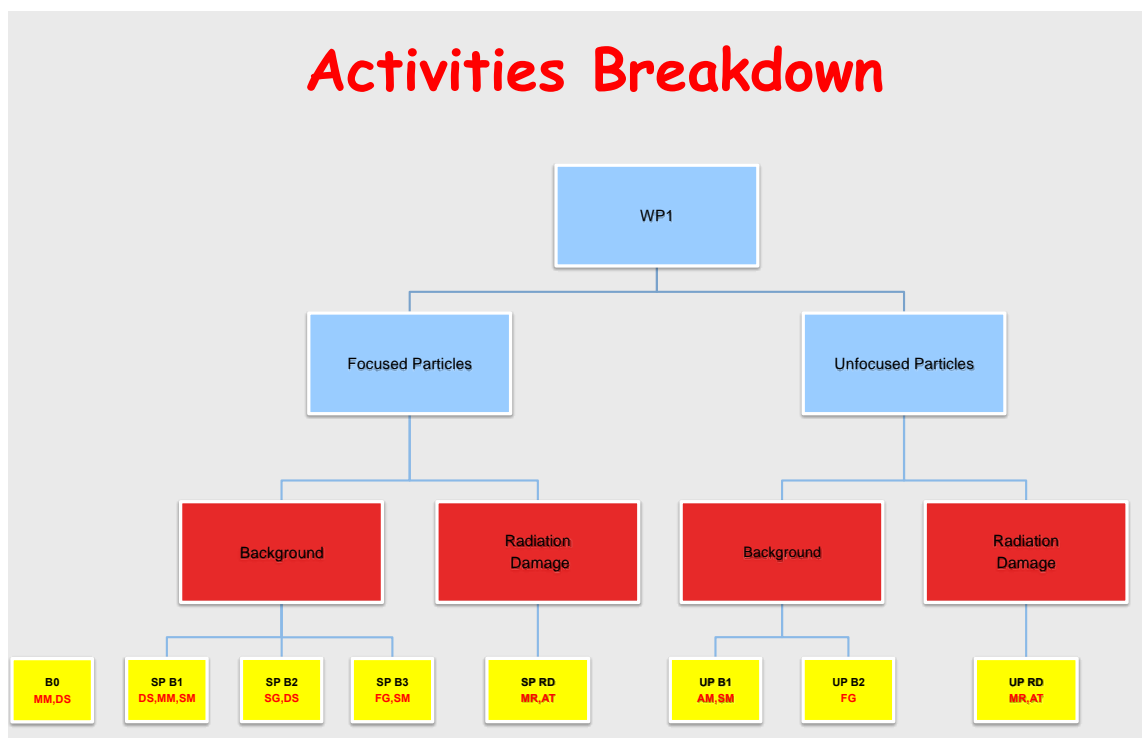


Figure 1.1: Schematic representation of activities in WP1. The bottom row reports sub-WPs and initials of involved workers. The first set of initials refers to the sub-WP leader.



2 B0: DATA PRODUCTION AND SELECTION

2.1 Introduction

2.1.1 XMM-Newton

The European Space Agency's X-ray Multi-Mirror satellite XMM-Newton was launched on the 10th December 1999 into a highly elliptical orbit, with an apogee of about 115,000 km and a perigee of ca. 6000 km. Due to several perturbations, the orbit changes with time.

The XMM-Newton spacecraft is carrying a set of three X-ray CCD cameras, comprising the European Photon Imaging Camera (EPIC). This offers the possibility to perform extremely sensitive imaging observations over the telescope's field of view (FOV) of 30 arcmin and in the energy range from 0.2 to 12 keV with moderate spectral ($E/\Delta E \sim 20-50$) and angular resolution (Point Spread Function FWHM ~ 6 arcsec).

Two of the cameras are Metal Oxide Semi-conductor (MOS) CCD arrays [Turner et al. 2001]. The third X-ray instrument uses pn CCDs and is referred to as the pn camera [Struder et al. 2001]. The two types of EPIC, however, differ in some major aspects. This does not only hold for the geometry of the CCD arrays and the instrument design but also for other properties, like e.g., their readout times.

All EPIC CCDs operate in photon counting mode with a fixed, mode dependent frame read-out frequency, producing event lists (tables with one entry line per received event, listing attributes of the events). Each CCD is nearly independent from the others, allowing for different configurations and can be independently shut off, thus resulting in CCD-dependent Good Time Intervals (lists of the time periods in which each CCD is operating correctly). The EPIC cameras allow several modes of data acquisition, with different FOV, spectral and timing resolution.

Another experiment on board of XMM-Newton is the EPIC Radiation Monitor (ERM). The main function of the ERM is the detection of the radiative belts and solar flares in order to supply particle environment information for the correct operation of the EPIC camera. In addition, the ERM provides detailed monitoring of the space radiative environment constituting a reference for the development of detectors to be used in future missions.

2.1.2 Optical filters

As the EPIC detectors are not only sensitive to X-ray photons but also to IR, visible and UV light, the cameras include aluminised optical blocking filters to reduce the contamination of the X-ray signal by those photons.

If such photons were registered by the EPIC detectors, the data analysis would be impeded in three ways:

- Shot noise on the optically generated photo-electrons will increase the overall system noise
- The energy scale will be incorrectly registered, because a nominally zero signal will have a finite offset. For each optically generated photo electron, the energy scale shifts by about 3.6 eV.
- Optically-generated photo electrons can lead to a saturation of electron traps, changing (improving) the charge transfer inefficiency.

There are four filters in each EPIC camera. Two are thin filters made of 1600 Å of polyimide film with 400 Å of aluminium evaporated on to one side; one is the medium filter made of the same material but with 800 Å of aluminium deposited on it; and one is the thick filter. This is made of 3300 Å thick Polypropylene with 1100 Å of aluminium and 450 Å of tin evaporated on the film. The remaining two positions on the filter wheel are occupied by the closed (1.05 mm of aluminium) and open positions, respectively. The open position could in principle be used for observations where the light flux is very low, and no filter is needed. The closed position can be used to study and model the instrumental background: about 1.5 Ms observations are publicly available and have been used in this work.

Comparison of focal plane organisation of EPIC MOS and pn cameras

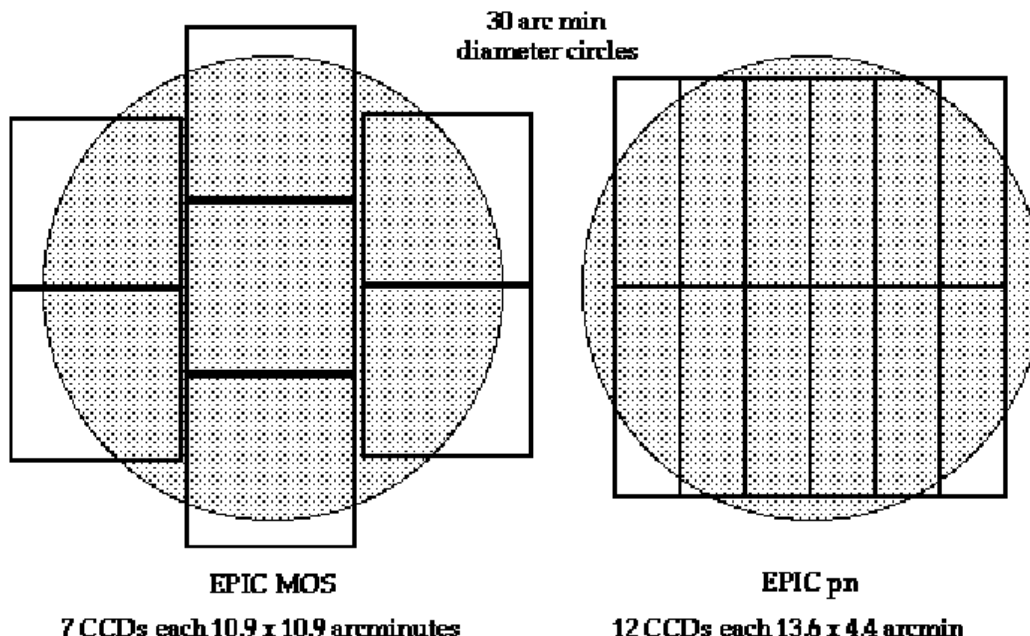


Figure 2.1: A rough sketch of the field of view of the two types of EPIC camera; MOS (*left*) and pn (*right*). The shaded circle roughly depicts the *inFOV* area.

2.1.3 XMM-Newton background

The EPIC background can be divided into two main components: a cosmic X-ray background (CXB), and an instrumental background. The latter component may be further divided into a detector noise component, which becomes important at low energies (< 200 eV) and a second component which is due to the interaction of particles with the structure surrounding the detectors and the detectors themselves. This component is characterized by a flat spectrum and is particularly important at high energies (above a few keV). The particle-induced background is usually further divided into two components: an external 'flaring' component, characterized by strong and rapid variability, which is often totally absent and a second more stable component. The flaring component is currently attributed to soft protons (with energies smaller than a few 100 keV), which are funnelled towards the detectors by the X-ray mirrors. The stable component is due to the interaction of high energy particles (with energies larger than some 100 MeV) with the structure surrounding the detectors and possibly the detectors themselves. Our comprehension of these processes on-board XMM-Newton is still incomplete, at now.

More details on the MOS quiescent instrumental background are given e.g. in Kuntz and Snowden [2008].

2.1.4 The aim of B0

Fifteen years of XMM-Newton data have been collected so far, allowing for detailed analysis of on-flight XMM-Newton characteristics and its response to photons and particle environment. Our aim is to produce the most complete and clean data set ever used to characterize XMM-Newton particle-induced background.

To this aim, we developed new python analysis tools. These scripts make use of a number of python libraries (numpy, pyfits, astropy), HEASOFT tools v.6.19¹, the XMM-Newton Science Analysis Software (SAS) v.14.0² and XMM-Newton calibration files as at 2016, April.

We select a conservative data set to reduce celestial sources contamination, CXB and instrumental noise. This is done through accurate camera, exposure and event filtering.

We disentangle the focused and non-focused components of the particle-induced background by studying different regions of the detector (inside and outside the Field-of-View). A region filter is applied in each observation to further reduce the celestial sources' contamination.

As final products, we compute clean light curves, spectra and images that allow for the deepest characterization ever of the XMM-Newton background.

Prescriptions, definitions and data sets from B0 sub-WP will be used for all the analysis of the other sub-WP, with their strengths and limits.

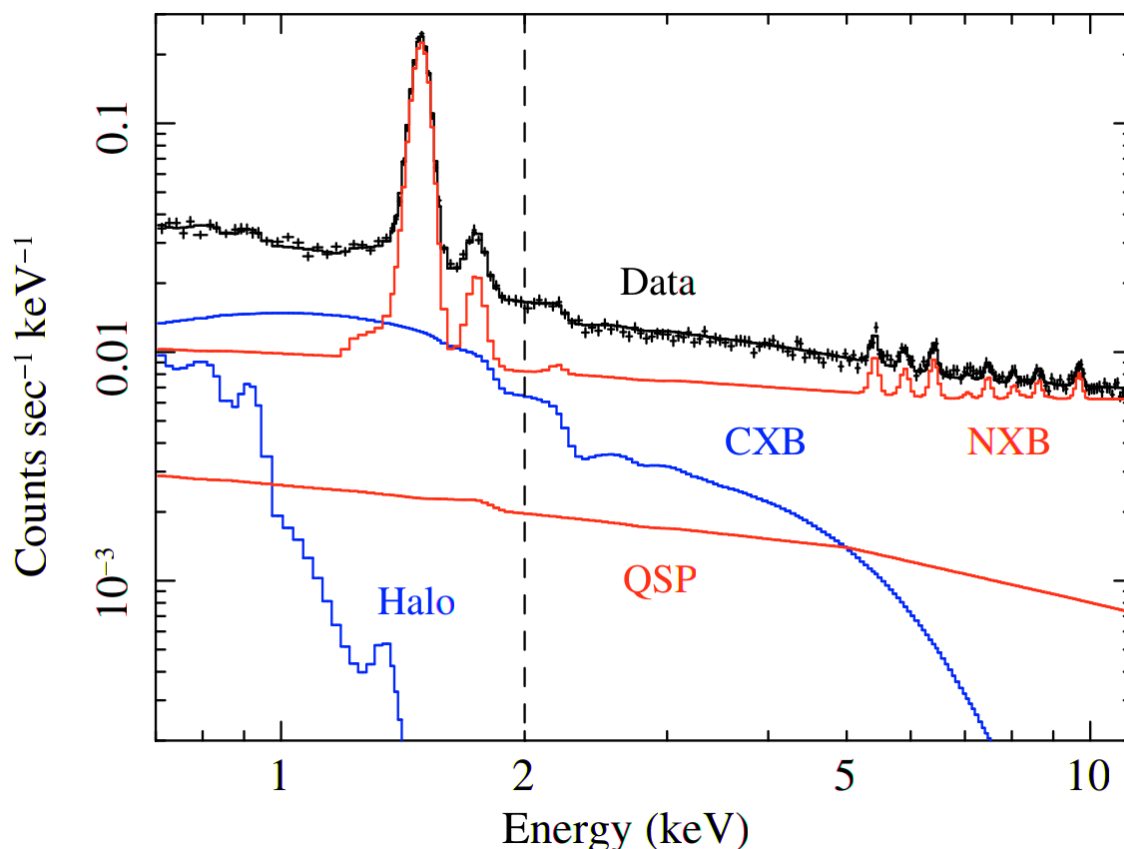


Figure 2.2: MOS spectrum from blank field observations in a 10'-12' annulus. The spectrum is fitted by using the different theoretical components: the Galactic Halo (Halo), the Cosmic X-Ray Background (CXB), the Cosmic-Ray-Induced continuum (NXB) and the so called "Quiescent Soft Protons" (QSP). From Leccardi and Molendi [2008].

¹ <https://heasarc.gsfc.nasa.gov/heasoft/>

² <http://www.cosmos.esa.int/web/xmm-newton/sas>

2.2 Data set selection

2.2.1 Camera selection

Among the three EPIC cameras, EPIC MOS have been usually preferred for studies of the background due to focused particles mainly because of the relatively small *outFOV* region (see Figure 2.1; from XMM-Newton Users Handbook³) of the pn and for its higher percentage of out-of-time (OOT) events. In fact, a minor fraction of *inFOV* events is wrongly assigned to the *outFOV* region as OOT. Contamination of the unexposed area of the pn detector due to a different camera geometry with respect to MOS is currently under investigation. We therefore exclude the pn camera from our analysis.

On March 2005, an event was registered in the EPIC MOS1 instrument, which was attributed to micrometeoroid impacts scattering debris into the focal plane. In the period immediately following the light flash it became apparent that MOS1 CCD6 was no longer recording events. From there, scientific observations are continuing normally with XMM-Newton, including MOS1, but with CCD6 switched off. A similar event took place in December 2012, causing the loss of MOS1 CCD3. In order to obtain a data set as uniform as possible with time, we exclude MOS1 camera from our analysis.

All the following results are therefore extracted and evaluated from the EPIC MOS2 camera.

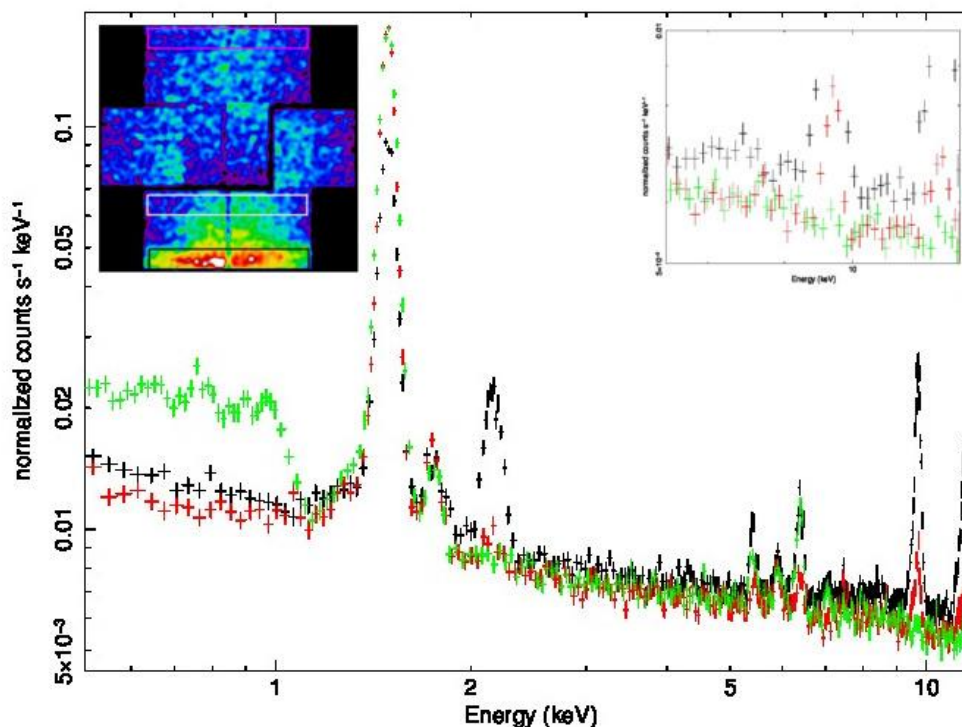


Figure 2.3: Spectra of closed observations for different regions of MOS2. The black line refers to the most affected region, the red one to a partially-affected region while the green one is not affected.

2.2.2 Event selection

We apply the standard filter on event patterns, using only single and double events. We also make use of the standard flags to avoid bright columns and pixels. See XMM-Newton Users Handbook for more details.

³ http://xmm-tools.cosmos.esa.int/external/xmm_user_support/documentation/uhb/

In order to isolate the instrumental background components, we make a conservative event selection based on energy. As apparent in Figure 2.2, showing the relative contribution of the different background components in MOS observations [Leccardi & Molendi 2008], the CXB spectrum measured by MOS has a break around 6 keV, its contribution becoming negligible above 7 keV: we therefore exclude the 0.2-7 keV energy band.

In the energy band $E > 7$ keV, one of the most prominent characteristics of the background spectrum is the gold fluorescence line at 9.7 keV (see Figure 2.3) and 11.4 keV. An analysis of closed observations reveals that such an emission is not spatially uniform, with an excess in CCDs 2 and 7 (Figure 2.4). Through the exclusion of the 9.4-10 and 11-12 energy band, we minimized this effect.

The resulting expression is:

```
(PATTERN<=12)&&((FLAG & 0x766a0f63)==0)&&(PI in [7000:9400]||PI in [10000:11000])
```

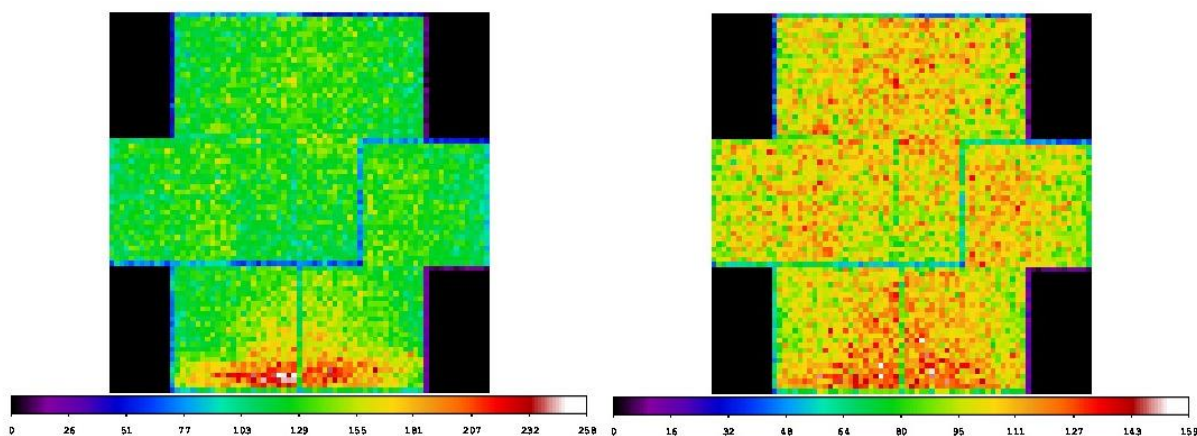


Figure 2.4 : Here we show the sum of the images of closed observations in the 7-11.8 keV and 7-9.4&10-11 keV bands, respectively. The improvement in uniformity, caused by the exclusion of the Gold line energy range, is apparent.

2.2.3 Exposures selection

For our analysis, we rely on twelve years of public XMM-Newton data, with source detection and characterization correctly and homogeneously performed through an official catalog. We reduce this data set both to lower the noise coming from e.g. celestial sources and to have a uniform data set, so that results from each observation can be compared.

In order to evaluate celestial sources' contamination, we rely on the 3XMM-DR4 source catalog⁴, that analyzes 7598 public XMM-Newton EPIC exposures made between 2000 February 3 and 2012 December 8.

We make the following selections:

- We make use of the preliminary results of the EXTras project⁵, therefore reducing our data set to the 7190 exposures available in EXTras at 2016 March.
- In order to avoid problems with the SAS attitude computation (e.g. for the exposure maps), we use only exposures with an attitude stability better than 5", as reported in the DAHPNT column of each exposure attitude file.
- To obtain a uniform data set, we select only exposures in the Full Window mode.

⁴ <http://xmmssc-www.star.le.ac.uk/Catalogue/3XMM-DR4/>

⁵ <http://www.extras-fp7.eu/index.php>

- d. In order to reduce celestial sources' contamination, we rely on the counts flux reported in the 3XMM catalog. We use their hardest band, 4.5-12 keV; under the hypothesis of a power-law spectral model with photon index 2, this flux is reduced to ~40% in our energy band. We exclude exposures in which the sum of the 3XMM counts flux (M2_RATE_5) coming from extended sources (source extension EP_EXTENT>12") is higher than 0.05 c/s (thus 0.02 c/s in our band).
- e. In order to reduce the PSF wings contribution [see Read et al. 2011], we exclude exposures containing point sources with a mean count flux (M2_RATE_5) higher than 0.5 c/s.
- f. In order to avoid problems with the 3XMM source detection due to the peculiar shape of the XMM-Newton PSF [see Read et al. 2011], we exclude exposures containing sources with a 0.2-12 keV mean count flux (M2_RATE_8) higher than 1 c/s.
- g. In order to exclude the Galactic Center diffuse contribution, we exclude observations centered in the box $|b| < 20^\circ$ & $|l| < 10^\circ$ [Krivonos et al. 2007].

Figure 2.5 reports the exposure we cut with each selection, and the remaining one.

We call "raw data set" the list of the exposures with filters a, b, c and "clean data set" the most conservative one, with all the listed filters. All the analysis in the other work packages are performed on the clean data set.

The python script we created, `FilterParams.py`, returns a fits table containing the main characteristics and selections of the good exposures for each data set.

2.3 Basic definitions and inputs

2.3.1 Basic definition: in field-of-view (*inFOV*)

We define as "In-Field-of-View" (*inFOV*) the detector area that is exposed to focused X-ray photons. For the MOS detectors, this area is roughly a 14.5'-radius circle composed by seven different squared

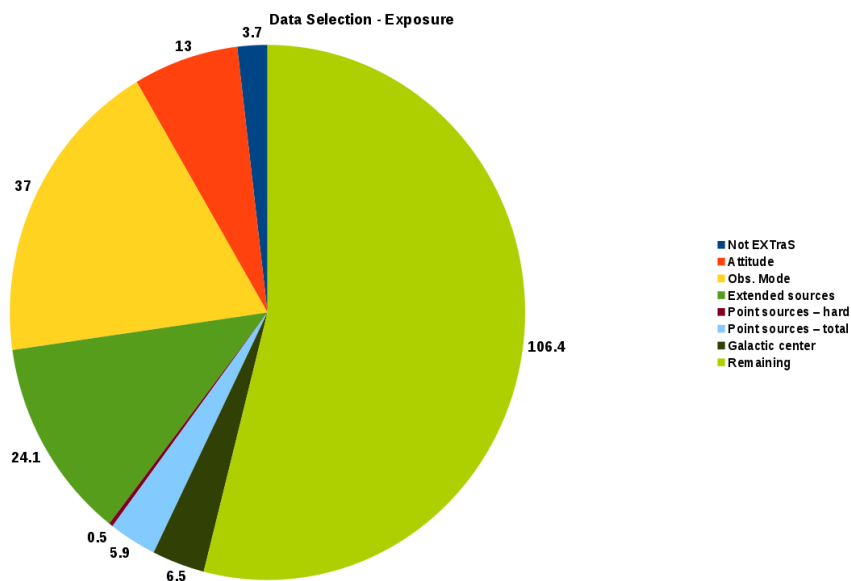


Figure 2.5: Simple representation of the XMM-Newton total exposure (in megaseconds) excluded after each selection.

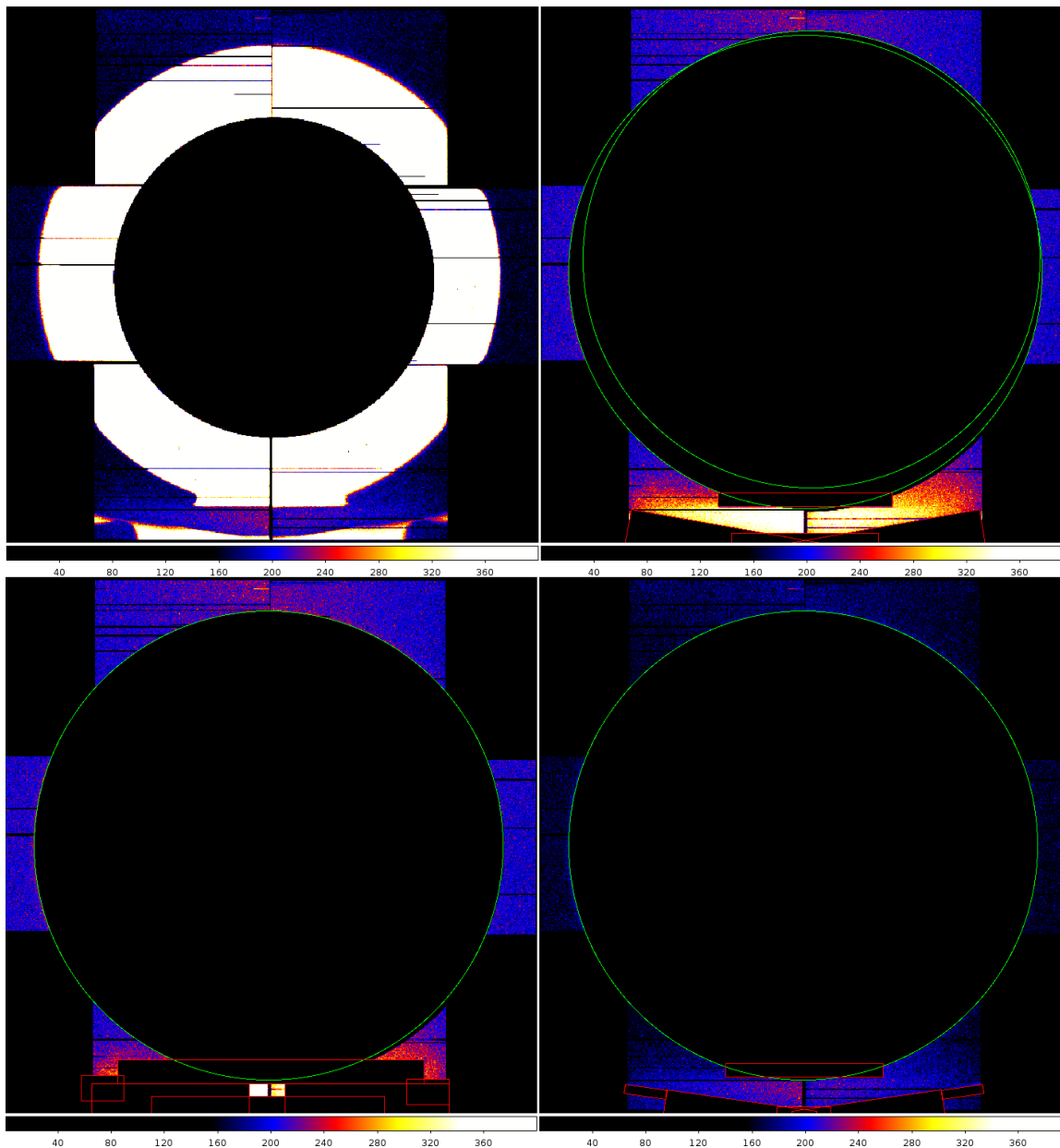


Figure 2.6: This figure shows the different approach that are used for the *outFOV* area selection. We summed images from our entire raw data set. *Upper left*: in this panel the celestial photons' contribution is clearly visible in the white areas (we excluded the central part of the *inFOV* area). *Upper right*: this comes from the area and energy selection used by Kuntz and Snowden [2008]. *Lower left*: this comes from the area and energy selection used by Read's script. *Lower right*: this is the *outFOV* area and energy selection we used for AREMBES.

CCDs (see Figure 2.1), separated by gaps. In our data set, this is obtained by imposing the filter flag (FLAG & 0x76ba000)==0), following prescriptions from 3XMM catalog.

All the *inFOV* products are normalized to this area, through corrections based on EXTraS exposure maps (see Sections 2.4, 2.5, 2.6). This filling method is based on the fundamental hypothesis of a spatial-independent background. Calibration analysis on proton flares already showed a marginally

ATHENA Radiation Environment Models and X-Ray Background Effects Simulators	WP1 TN 1.1	Doc No: IASFMi-ATHENA-WP1 Date: 10 February 2017 Page: 15 of 78
---	-----------------------------	---

spatial-dependent distribution, peaked around the boresight [e.g. Kuntz & Snowden 2008]. At a first order, we assume that the instrumental background is constant throughout the detector (for more details see Section 2.6).

2.3.2 Basic definition: out field-of-view (*outFOV*)

We define as “Out-Field-of-View” (*outFOV*) the detector area that is not exposed to celestial photons. For the MOSs, this is roughly the total detector area with the exclusion of the *inFOV* area. In the literature, different areas have been used for different studies. Figure 2.6 reports the regions used for the different approaches.

Kuntz and Snowden [2008] and Read’s f_{in}/f_{out} script⁶ use an empirical approach based on a limited data sample. The first maximizes the considered *outFOV* area, so that their results are heavily affected by the presence of the Gold lines (see Section 2.2.2). The second accurately excludes the Gold-Line-affected area, thus greatly reducing the considered *outFOV* area.

We based our work on a longer data set, excluding the area clearly affected by celestial photons through an accurate analysis. In order to maximize the *outFOV* area, we do not exclude spatial regions affected by the presence of the Gold lines, but we dealt with this problem through energy selection, by excluding the 9.0-9.4 keV and >11 keV range. Our region is defined as follows:

```
-circle(-50,-180,17540) -box(0,-17000,11800,1000,0) -box(-4800,-20150,11300,1830,352) -
box(0,-20200,4000,1000,0) -box(4800,-20150,11300,1830,8)-box(11850,-18600,3150,700,8) -
box(-11850,-18600,3150,700,352)
```

When compared to *inFOV*, *outFOV* results are normalized on the total *inFOV* area.

2.3.3 Inputs: from XSA and 3XMM to EXTraS

We download Processing Pipeline Subsystem (PPS) XMM-Newton data sets from the XMM-Newton Science Archive (XSA) as at the beginning of the **AREMBES** project (2016, March). These data are automatically processed from observation data files (ODF) using the SAS v 13.5, as reported in the XMM-Newton Users Handbook.

All the sources definition, positions, and characteristics come from the 3XMM-DR4 catalog. We define as 'point-like sources' all the sources with extent radius (as defined in 3XMM) lower than 12".

As input, we also take exposure maps and background regions from primary and secondary products of the EXTraS project, as at the beginning of the **AREMBES** project (2016, March). We note that background regions are optimized to maximize the background contribution and to exclude point-like sources contribution in the 0.2-12 keV energy band, thus the residual source contribution is always less than 0.5% of the background contribution in the **AREMBES** band.

2.4 Light curves creation

2.4.1 *outFOV* / *inFOV* area rescale

As a first step, we evaluate the *outFOV* to *inFOV* area rescale factor. The detector active area can be time-dependent due to the instrument degradation. We therefore evaluate the *inFOV* and *outFOV* areas during time chunks with at least 3 Ms of exposure (chosen to provide a good statistics) thus dividing

⁶ http://xmm2.esac.esa.int/external/xmm_sw_cal/background/epic_scripts.shtml

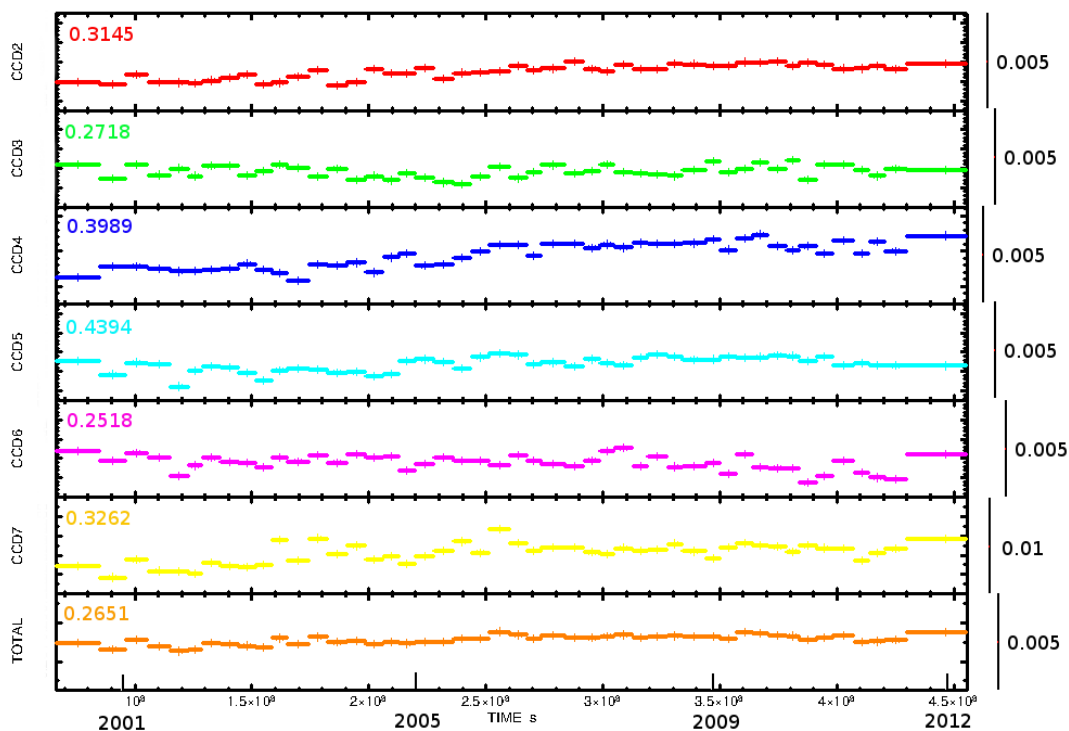


Figure 2.7: *outFOV*/*inFOV* rescale factor variation with time, for each CCD and in total.

our raw data set into 47 chunks, using the script `athena_chunks.py`. For this analysis we use the full 0.2-12 keV energy band.

We sum the counts images of each exposure in a chunk: we define the sum of non-null pixels in the *inFOV*(*outFOV*) area as the *inFOV*(*outFOV*) area. The excellent statistics provided by 3 Ms of data makes it almost impossible to have zero counts on an active pixel. The *outFOV*/*inFOV* time-dependent rescale factor (RESCALE_OFOV) is defined as the ratio of the areas. The script `athena_rescale.py` does the computations and writes all the results in a fits file.

The resulting area time variation is not statistically significant, with a mean *inFOV* area of 674.58 ± 0.17 arcmins² and *outFOV* area of 206.81 ± 0.17 arcmins².

We tested the results of this method using the 'backscale' SAS tool for a limited subsample of observations. This method works well for simple region files but it can give wrong results for complex regions. In the test cases, we found a discrepancy less than 0.001 (see Figure 2.7). Tests on the closed observations data set revealed a discrepancy of less than 10^{-7} .

2.4.2 General Preparation

We filter each event files for energy, pattern, flag and area selections, as presented before. In particular, for the *inFOV* region we extract counts only within the EXTraS background regions. Counts from different CCDs are stored separately. For each CCD we therefore produce filtered raw light curves with a set of time bins (10s-500s-5000s).

We extract the Good Time Intervals (GTI) of each CCD from the event file. These are the time intervals in which the CCD was collecting photons. For each time bin of the raw light curves we computed its GTI fractional coverage (FRACEXP), where 0 means no coverage and 1 full coverage.

ATHENA Radiation Environment Models and X-Ray Background Effects Simulators	WP1 TN 1.1	Doc No: IASFMi-ATHENA-WP1 Date: 10 February 2017 Page: 17 of 78
---	---------------	---

In order to correct for the excluded *inFOV* areas, we rely on EXTraS *inFOV* exposure maps (they can be computed only for the *inFOV* area using SAS). They are not corrected for photons vignetting, as needed for our photons+particle-induced background.

We compute the integral of the EXTraS exposure map and the integral of the cheesed exposure map, using the EXTraS background region. The ratio of the two integrals is defined as RESCALE_INFOV factor, that can be used to rescale the *inFOV* counts and fill the holes due to point-like sources in the *inFOV*.

All these information are stored in fits files and used for the clean light curves computations.

2.4.3 *inFOV* and *outFOV* light curves computation

Using the ingredients from the previous analysis, for each time bin of 500 sec we compute the *inFOV* and *outFOV* clean count rate, its associated error and fractional exposure, combining the values in each CCD as follows:

$$CR_I = R_I^{-1} dt^{-1} \sum_{j=1}^7 \left(\frac{N_j^I}{F_j} \right)$$

$$\sigma(CR_I) = R_I^{-1} dt^{-1} \sqrt{\sum_{j=1}^7 \left(\frac{N_j^I}{F_j^2} \right) + \frac{3}{8}}$$

$$F_I = \left(\sum_{j=1}^7 N_j^I \right) \times \left(\sum_{j=1}^7 \frac{N_j^I}{F_j^I} \right)^{-1}$$

$$CR_O = R_O^{-1} dt^{-1} \sum_{j=2}^7 \left(\frac{N_j^O}{F_j} \right)$$

$$\sigma(CR_O) = R_O^{-1} dt^{-1} \sqrt{\sum_{j=2}^7 \left(\frac{N_j^O}{F_j^2} \right) + \frac{3}{8}}$$

$$F_O = \left(\sum_{j=1}^7 N_j^O \right) \times \left(\sum_{j=1}^7 \frac{N_j^O}{F_j^O} \right)^{-1}$$

where the subscripts *I* and *O* refer to *inFOV* and *outFOV* respectively, R_I is the RESCALE_INFOV factor (Section 2.4.2), R_O is the RESCALE_OFOV factor (Section 2.4.1), dt is the bin time, N_j^I/N_j^O the number of counts in the *inFOV*(*outFOV*) area of the j^{th} CCD, and F_j the FRACEXP of the j^{th} CCD (Section 2.4.2). Since this configuration for *outFOV* light curves makes poor statistics in time bin of 500 sec, we decide to calculate a running mean, a running standard deviation and a running fractional exposure using the 2 nearest time bins around each time bin. These light curves are characterized by time bins of 2500 sec and step of 500 sec. For the first and last 2 time bins we force the count rate and its standard deviation to -1 and the fractional exposure to 0. As a result, we modify previous equations for *outFOV* taking into account that:



$$N_j^O = \sum_{t=T-2dt}^{T+2dt} N_t^O$$

$$F_j^O = \frac{1}{5} \left(\sum_{t=T-2dt}^{T+2dt} F_t^O \right)$$

where T is the time on which the 2500 sec time bin is centered.

Each light curve is produced as a FITS file format containing five columns: revolution ID (*REV_ID*), time (*TIME*), count rate (*RATE*), 1σ standard deviation on count rate (*ERATE*) and fractional exposure (*FRACEXP*).

The work described in Sections 2.4.1-2.4.3 is performed by *athena_infov.py* and *athena_ofov.py* scripts. The results for the entire data set are collected in a single fits file (the Main File); for details on this file see Section 3.2.3.

Light curves created with SAS standard tools (*evselect*) are different from what we produce due to the rescale factors and are distorted by CCD-dependent GTIs, while we correct this problem through the *FRACEXP* factors. Although Bad Time Intervals are quite rare for the MOSs cameras, when they occur the shape of the curve is badly affected, as shown in Figure 2.8.

2.5 Spectra computation

We produced the scripts *athena_spectra.py* and *athena_mergespectra.py* to extract and select XMM-Newton background spectra.

For each 500s-time-bin defined in Section 2.4, we extract *inFOV* and *outFOV* spectra in the 0.2-12 keV energy range, using the same pattern, region and flags filters as for the light curve computation. We bin the spectra in order to obtain 15 channels/bin, for a total of 800 channels. For each row of the light-curve Main File, we add an array of 800 elements, containing the grouped spectrum of that time bin, thus allowing any post-processing selection. The second script allows the user to make a selection of the 500-s spectra basing on column selections of the Main File (e.g. *inFOV* / *outFOV* ratio, optical filter, time, ...) and merges all the selected spectra into a single file for *inFOV* and one for *outFOV*. The *BACKSCAL* keyword in the spectrum (readable by the standard XSPEC) takes into account the area rescale factor, so that they are rescaled to the same *inFOV* area. Similarly, the *EXPOSURE* keyword is correctly calculated. Figure 2.9 reports, as an example, the *inFOV* and *outFOV* spectra of our entire dataset.

These spectra are used for SPB1 sub-WP (Section 3) spectral studies.

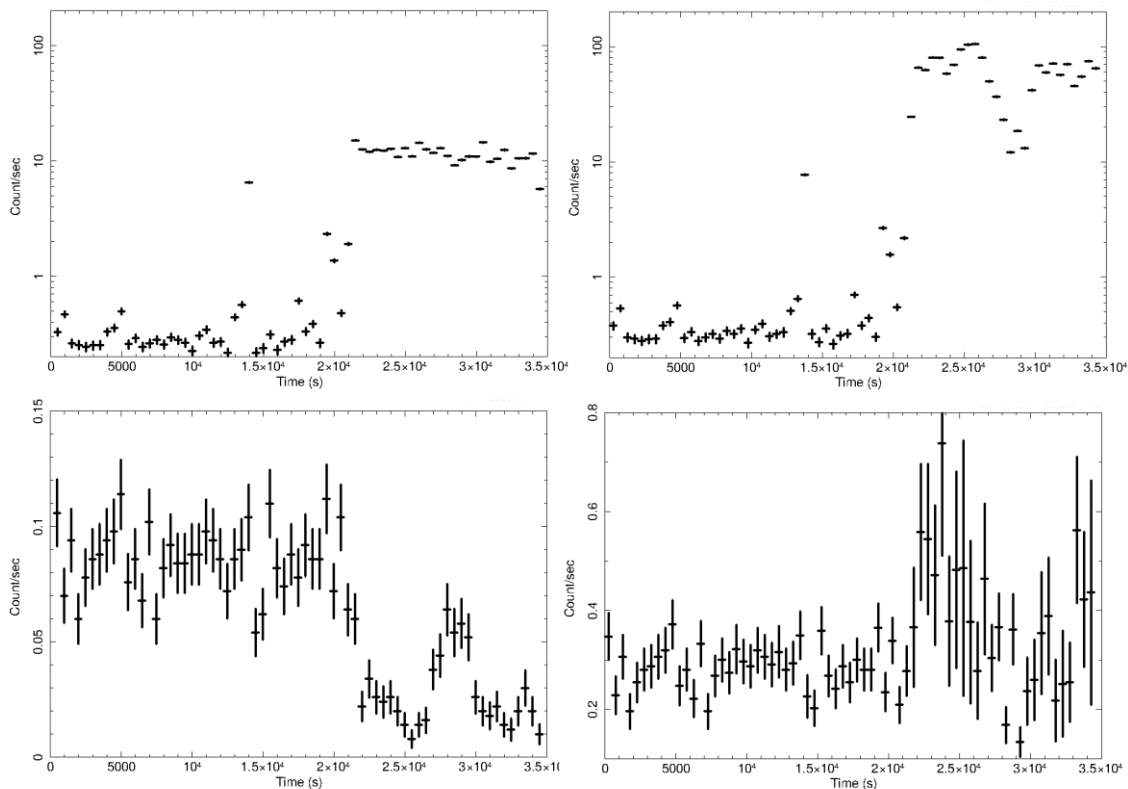


Figure 2.8: We show an examples of raw and clean light for an observation with CCD-dependent bad time intervals (0506130201-S002), to show the improvements in our method. *Upper left*: raw *inFOV* light curve, as obtained using the *evselect* SAS command. *Upper right*: clean AREMBES *inFOV* light curve, directly comparable with curves from all the other exposures. *Lower left*: raw *outFOV* light curve, as obtained using the *evselect* SAS command. *Lower right*: clean AREMBES rescaled *outFOV* light curve, directly comparable with the *inFOV* clean light curve.

2.6 Image computation

Similarly to the spectra computation, we developed the scripts `athena_exposures.py`, `athena_images.py` and `athena_mergeimages.py` to prepare, extract and select the detector-coordinates XMM-Newton images and exposures. For this task we cannot rely on EXTraS exposure maps because they are in sky coordinates.

The first script produces an exposure map for each observation, in detector coordinates and cheesed with the EXTraS background region. The bin size is optimized to obtain both a good spatial resolution for the image and a reasonable size for the file.

The second script extracts images from each 500s light-curve time bin following the same filters as in the light curve computation (also for the energy band). The results are stored in arrays as new columns of the Main File. In order to save disk space (and RAM), these results are compressed and therefore not easily readable.

The third script allows the user to make a selection of time bins based on columns of the Main File (e.g. *inFOV* / *outFOV* ratio, optical filter, time) and merge all the selected images into a single image for *inFOV* and one for *outFOV*. Moreover, this script merges the corresponding cheesed exposure maps and corrects the counts image for the exposure, thus filling the holes in the *inFOV*. We note that, in

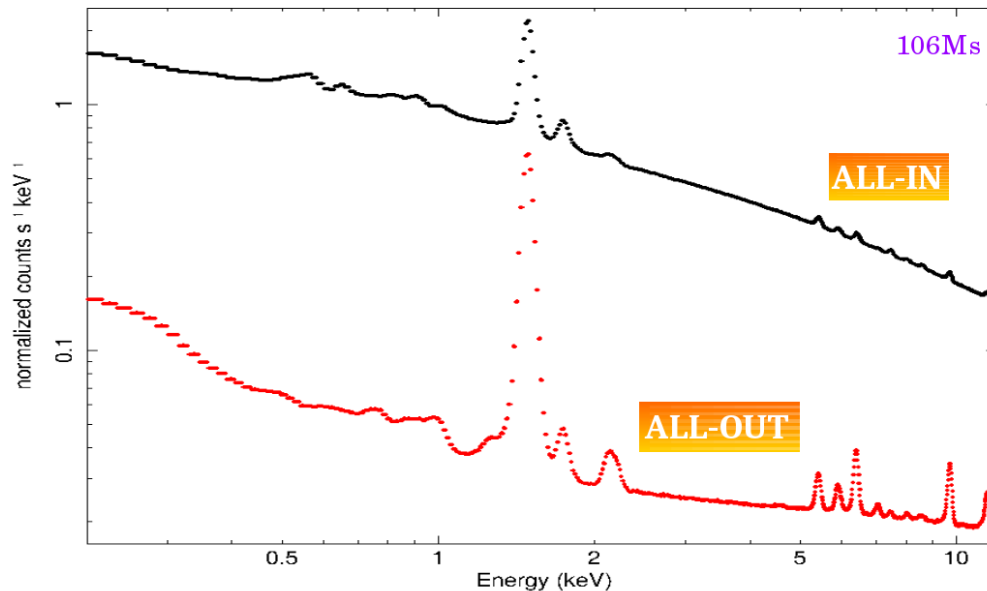


Figure 2.9: An example of the spectra that we are able to produce. Here, we show the spectra of *inFOV* (black) and *outFOV* (red) using our entire clean data set. We note that the two spectra are area and exposure-corrected and therefore directly comparable.

case of a low statistics, the pixel size should be increased by the user. With such a big data set, some bright pixels and columns result not to be correctly treated by SAS tools. We therefore correct the image by lowering the counts of bright, isolated pixels and columns. Both the Main File and single-observations exposure maps are needed as input for this script.

Figure 2.10 shows the MOS2 images during periods dominated by 'quiescent' and 'flaring' background (see Section 3.3.1 for the definition of the time periods).

While a detailed imaging analysis cannot be accommodated within the resources available to the **AREMBES** project, simple inspection of these images is sufficient to glean some rather interesting features. We list here some of them.

- There is significant vignetting of the proton flares component (right panel), with a possible offset with respect to the center of the FOV.
- The proton flares component also presents a CCD-dependent spatial behaviour, with the central pixel brighter than the others (right panel).
- The quiescent background varies by about 10-20% within each CCD increasing with distance from the read out node (left panel).
- Different CCDs appear to have different quiescent levels (left panel).

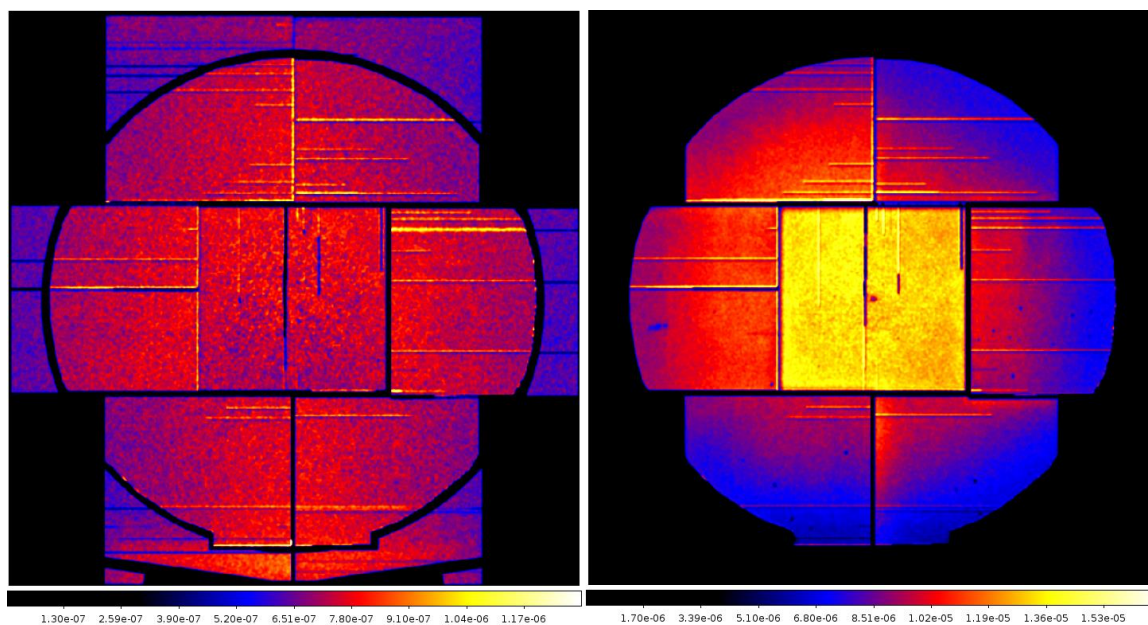


Figure 2.10: An example of the images that we are able to produce. Here, we show the images of *inFOV* and *outFOV* regions for *inFOV-outFOV* values below 0.1 cts/s (*left*) and above 0.4 cts/s (*right*), thus roughly representing the quiescent background and the flaring background we are analyzing in the AREMBES project. In the right image the *outFOV* regions are present but are not visible as the intensity of the emission is much lower than in the *inFOV* part.



3 SPB1: CHARACTERIZING THE FOCUSED PARTICLES BACKGROUND

3.1 Introduction

The aim of sub-WP SPB1 is to accurately characterize the focused particles background on EPIC/MOS instrument on board of *XMM-Newton* telescope, usually attributed to soft protons (SP). There has been considerable work over the years on this topic, e.g. De Luca and Molendi [2004] measured the contamination given from SP to characterize the Cosmic X-ray background; Carter and Read [2007] studied the various components to EPIC background; Kuntz and Snowden [2008] characterised the spectral and spatial response of the EPIC-MOS detector to SP background; Leccardi & Molendi [2008] characterized all background components, included SP one, to study the radial temperature profiles for galaxy clusters.

We have performed a systematic analysis of the entire EPIC archive for the first time. Our work is based on 13 years of *XMM-Newton* observations, from 2000 to 2012. This corresponds to the largest EPIC data set ever analyzed, which allows us to study and characterize meticulously the behavior of this background component through spectral and timing analysis.

A common way to quantify the impact of this component is to compare the background count rate in the field of view (*inFOV* region) with the unexposed corners (*outFOV* region), where this component is not present. In our analysis, we also follow this approach but with a different indicator: we have mostly made use of the “*inFOV* subtracted by *outFOV*” diagnostic, rather than the “*inFOV* over *outFOV*” used by other authors. The latter indicator allows to quantify the contribution of SP to EPIC background or to analyse its spectral behaviour, but only with the former diagnostic is it possible to isolate the background component which produces an excess of count rates in the *inFOV* region and study its characteristics. As stated in Section 2.2.1, we performed our analysis only on MOS2, because of the lack of a proper *outFOV* for the pn detector and the loss of a CCD in MOS1. However, our analysis could be easily performed on MOS1 with little changes to our method.

Statistical quality of the data is unprecedented. To fully exploit this we have performed a scrupulous analysis of systematics, which are often the source of the dominating uncertainties in our work.

As will become apparent in the next sections, the background component causing a count-rate excess in the *inFOV* region can be further divided into two components: a flaring component (currently attributed to soft protons flares) and a low-intensity residual component whose origin is still unclear. In this Section, we will:

- derive the fraction of observing time with flares (Section 3.3);
- define the low-intensity *inFOV* component (Section 3.3);
- study the evolution of the flaring and low-intensity *inFOV* components through the mission (Sections 3.5 and 3.6).

3.2 Data preparation

We base our analysis on the clean dataset, whose selection and production is described in Section 2.2, consisting in 3936 exposures with a total exposure time of 106.42 Ms.

We have developed an ad-hoc pipeline to perform the different steps of the analysis in an automated way. The implemented algorithms have the following main steps, some of which have already been described:

- standard event selection per each individual exposure (see Section 2.2.2);
- energy selection on our data set to exclude CXB contribution (see Section 2.2.2);
- region selection for data located in the *inFOV* and in the *outFOV* regions (see Section 2.3);



- *inFOV* and *outFOV* light curve computation per each individual exposure (see Section 2.4);
- stacking of the data. We merge all light curves associated to single exposures to generate a “global” *inFOV* light curve and a “global” *outFOV* light curve associated to the entire data set (see Section 3.2.1);
- subtraction of the *outFOV* from the *inFOV* light curve. To each *inFOV* time bin we subtract the *outFOV* count rate to the *inFOV* one and we compute a standard deviation using the standard error propagation rule (Section 3.2.2);
- production of a master file containing per each time bin all the information to generate and analyse the *outFOV*-subtracted light curve for *inFOV* (hereafter *inFOV-outFOV*). The file is in FITS format and is named *Master_bkglc_all_500.fits* (Section 3.2.3).

The first four points were widely described in Section 2, while the others will be described in detail in the following Sections. The automatic pipeline may be used in future to perform the same analysis for MOS1 camera or for a larger data set containing observations released after 2012. The pipeline is based on a Python script named *JoinTotalINOUT.py*.

3.2.1 Stacking of the data

We merged all the generated light curves to obtain two final light curves, corresponding to the *inFOV* and the *outFOV* light curves for both the sky fields. We do not fill the gap between two consecutive observations and we do not change the TSTART or TSTOP of the light curves to achieve a gap as a multiple of the time bin value because we are not interested in using such data to perform any Fourier analyses. The total exposure time in the final data set is of ~106.42 Msec.

3.2.2 *inFOV-outFOV* light curves computation

As described before, the best way to estimate the focused background component is to measure the *inFOV* count rate, using the *outFOV* region as a calibrator to minimize any contamination from other background components. For this reason we produce an *outFOV*-subtracted *inFOV* light curve where in each 500 sec time bin we compute the difference between *inFOV* and *outFOV* count rate and estimate its error using the standard error propagation rule.

3.2.3 The Master SPB1 background file

The most important product of our pipeline is the Master SPB1 background file (hereafter Master file), a file in FITS format named “*Master_bkglc_500.fits*” containing per each 500 sec time bin the most important information to study and characterize the *inFOV* background. The file includes 21 columns, below a brief description:

- REVID: the revolution identifier;
- TIME: mean time of the 500 sec bin in XMM format (time in seconds since 1998.0 TT);
- RATE_IN: expected count rate from the *inFOV* corrected by the *inFOV* rescale factor;
- ERATE_IN: 1σ standard deviation of RATE_IN;
- FRAC_IN: fractional exposure (ratio between the good time interval and the time bin) in the *inFOV*;
- RATE_OUT: expected count rate from the *outFOV* (calculated using the running mean, Section 2.4.3) corrected by the *outFOV* rescale factor;
- ERATE_OUT: 1σ standard deviation of RATE_OUT;
- FRAC_OUT: fractional exposure in the *outFOV* (calculated using the running mean, Section 2.4.3);
- FRAC_OUT500: fractional exposure in the *outFOV*;
- RATE_DIF: *outFOV*-subtracted *inFOV* count rate (RATE_IN-RATE_OUT);
- ERATE_DIF: 1σ standard deviation of RATE_DIF extracted by the error propagation rule;

- RATE_RAT: ratio between the *inFOV* count rate and the *outFOV* count rate (RATE_IN/RATE_OUT);
- ERATE_RAT: 1σ standard deviation of RATE_RAT extracted by the error propagation rule;
- FILTER: optical filter;
- OBSID: observation identifier;
- RESCAL_IN: rescale area factor to obtain the expected *inFOV* count rate in the full *inFOV* region;
- RESCAL_OUT: rescale area factor to obtain the expected *outFOV* count rate in the full *inFOV* region.

In addition, the Master file contains per each time bin a number of raw information related to the position of the *XMM-Newton* telescope in the sky and the revolution phase. Such parameters are extracted from public orbit files (see Section 4.3.2 for more details). We provide below the description of each parameter:

- X: x-axis position vector in celestial coordinates system;
- Y: y-axis position vector in celestial coordinates system;
- Z: z-axis position vector in celestial coordinates system;
- PHASE_RAW: orbit phase obtained as the ratio between TIME-TSTART and TSTOP-TSTART where TSTART and TSTOP are the start and stop time of the orbital revolution, respectively.

3.2.4 Final data set selection

After a large number of tests we have decided to exclude time bins where the counts statistic is too poor in the *inFOV* or in the *outFOV* to apply the Gaussian statistic. The number of observed counts in each time bin depends strongly on two parameters, the good time interval with respect to the time bin (represented by FRACEXP parameter) and the dimension of the selected collecting area (represented by RESCALE parameter). Increasing the FRACEXP the photon counts increase, while increasing the RESCALE parameter they decrease. A strong estimator to filter time bins with poor statistics may be extracted from the distribution of the ratio between the FRACEXP and the RESCALE for *inFOV* and *outFOV* (see Figure 3.1).

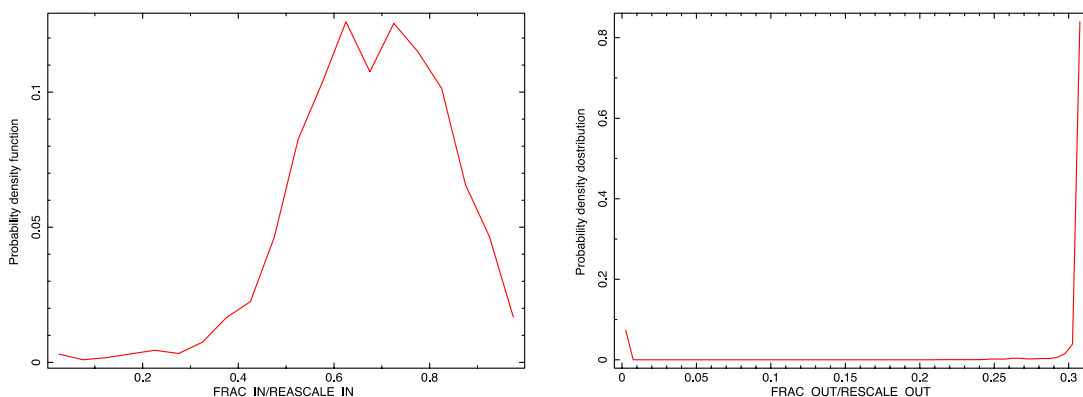


Figure 3.1: Probability density distribution of the ratio between the FRACEXP and the RESCALE for the *inFOV* (left) and *outFOV* (right).

Analysing such distribution, we decide to include in our data set only time bins with

$\frac{F_I}{R_I} > 0.49$ and $\frac{F_O}{R_O} > 0.29$, where $F_I(F_O)$ and $R_I(R_O)$ are respectively the FRACEXP and rescale factor for the *inFOV* (*outFOV*) region.

As a result, the exposure time in the filtered data set is of ~89 Msec.

3.3 Analysis of the *inFOV-outFOV* distribution

From the Master file we construct the count rate cumulative distribution function (CDF) and the differential distribution function (DDF) (see Figure 3.2). The former shows the fraction of time with respect to the filtered exposure time (here named “OnTime”) spent by the *inFOV* background below a given count rate, while the latter shows the number of time bins where the count rate were within a given count rate bin. We analyze such distributions to characterize in unprecedented detail the *inFOV* background. Median count rate and median absolute deviation (MAD), defined as the median of the absolute deviation from the data’s median, are shown in Figure 3.2.

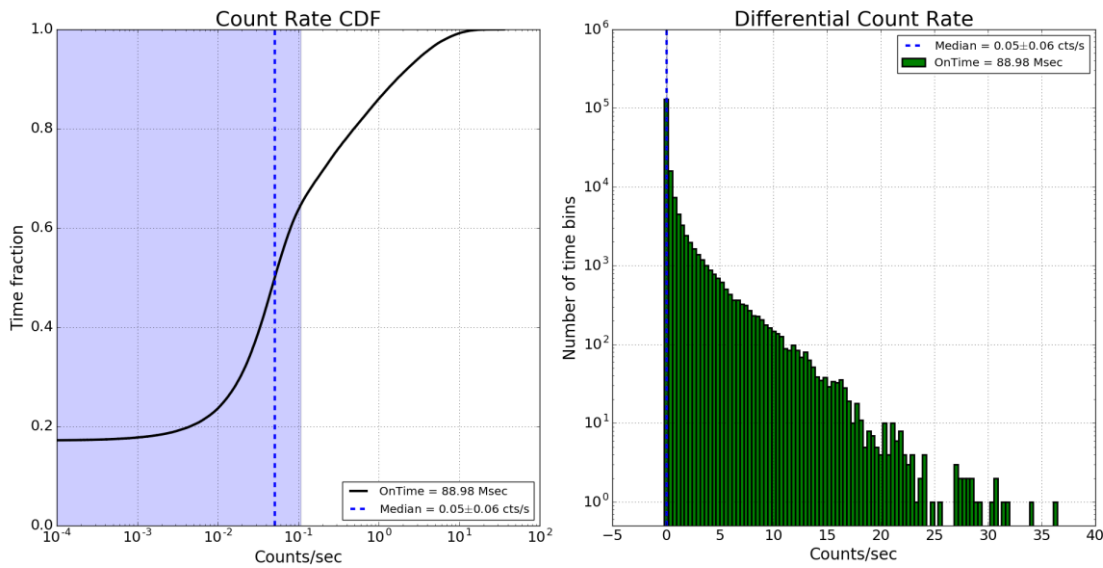


Figure 3.2: (Left) *inFOV-outFOV* count rate cumulative distribution function (CDF). Blue dotted vertical line shows the median, while the light blue span the median absolute deviation (MAD) defined in the text. (Right) *inFOV-outFOV* count rate differential distribution function (DDF).

3.3.1 *inFOV-outFOV* count rate distribution

Count rate CDF and DDF show that the *inFOV* background is composed by two main components, a “*quiescent*” one, characterized by low count rate distributed following a Gaussian shape, and a “*flaring*” one, characterized by higher counts/sec distributed following a more complex shape, similar to a power law.

Analysing the CDF we can extract the fraction of observing time with flares. Such distribution derives from an empirical characterization of the DDF with a Gaussian component plus a more complex one, that will be discussed in the next section. The flaring component becomes dominant in the distribution for count rate larger than ~0.1 cts/s. The fraction of time when the *inFOV* background is characterized by a count rate larger than such value is ~35% of “OnTime” (31.15 Msec). For the remaining ~65% of time (57.83 Msec) the *inFOV* background were in a “quiescent” state.

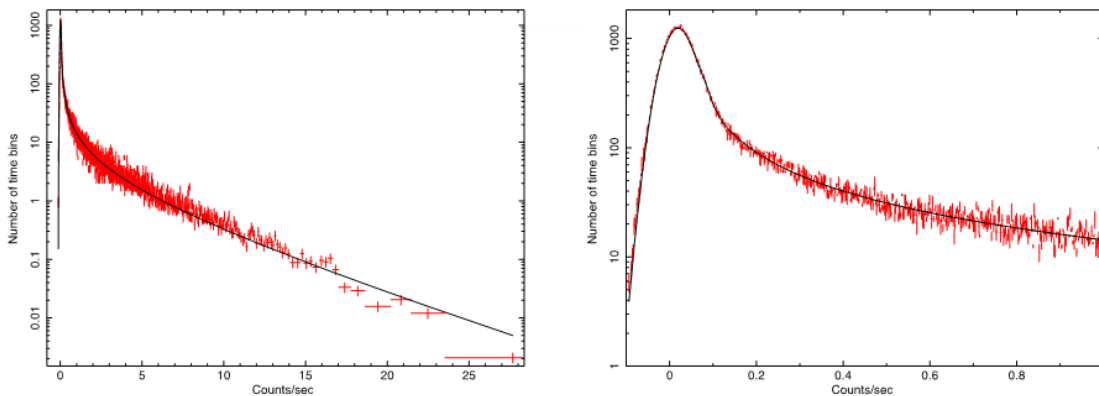


Figure 3.3: (Left) Global *inFOV-outFOV* DDF (shown in red) over-plotted by the best-fitted empirical distribution defined in the text (black line). (Right) Zoom of the distribution for the low count rate regime.

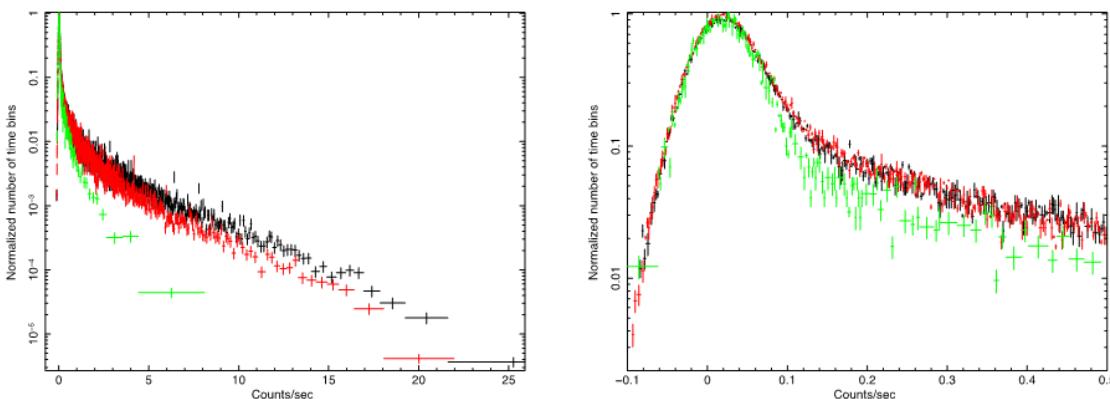


Figure 3.4: (Left) Normalized *inFOV-outFOV* count rate DDF for observations with Thin (black), Medium (red) and Thick (green) filter. (Right) Zoom of the same distribution for the low count rate regime.

3.3.2 Empirical characterization of the *inFOV* background components

Analysing the DDF we can study in detail the shape of *inFOV* background components. Figure 3.3 and Figure 3.4 show the DDF generated by an adaptive binning algorithm. As first, we produce a distribution with a uniform bin of 0.001 cts/s, and then we re-bin the distribution in order to achieve a signal-to-noise ratio of 5 per output bin.

The background distribution is characterized by a Gaussian component in addition to a more complex one. We model such component with an empirical model defined as a modified Lorentzian distribution as follows:



$$F(x) = \frac{LN \cdot x^{\Gamma_1}}{1 + \left| \frac{2(x-LC)}{LW} \right|^{\Gamma_2}} e^{-x/X_0}$$

where LN is the normalization and LC the center of the Lorentzian, LW the full width at half maximum (FWHM), Γ_1 the slope of power-law component, Γ_2 the slope of the denominator component and X_0 the exponential cut-off component.

We find that the Gaussian component is characterized by a mean value significantly different from zero (mean=0.0174±0.0001 cts/s) and a standard deviation equal to 0.0328±0.0001 cts/s. The width of the Gaussian is related to the subtraction process and is associated with the statistical fluctuation at low count rate. We verified that increasing the time bin value for *inFOV* and *outFOV* light curves, the standard deviation value of the Gaussian component decreases maintaining unchanged the mean value (within statistical errors). We define the Gaussian component as a “*low-intensity*” component because we are not able to check if it is variable or quiescent.

The values of parameters related to the modified Lorentzian component are below:

LC=0.079±0.001; LW=0.110±0.001; X₀=5.37±0.06; Γ_1 =0.47±0.03; Γ_2 =1.34±0.03

All quoted errors on the empirical model parameters are at 1 σ confidence level for a single interesting parameter. This component clearly shows the complex behaviour of the *inFOV* flaring background.

The modified Lorentzian component becomes dominant at about 0.1 cts/s (see Figure 3.3), where the DDF clearly deviates from the Gaussian component. This justifies the choice of this threshold to compute the fraction of time dominated by the flaring component in the previous section.

We underline here that the parameters of our empirical model are strongly degenerate with each other and therefore all the quoted errors should be taken with caution and considered as a lower limit.

3.3.3 *inFOV-outFOV* distribution as a function of filter

As discussed in Section 3.1, the focused background component is commonly attributed to the so-called soft protons (see e.g. Leccardi e Molendi [2008]). One key observation for this interpretation was performed during operational test, with the MOS detectors in reduced gain mode (allowing to measure energies up to 100 keV) and using different filters (thin for MOS1 and thick for MOS2). Spectra in the two detectors, obtained in a period of flares, were similar in shape but offset by about 30 keV in energy, which is consistent with the losses expected in the thick filter for protons from a few tens up to hundreds of keV [Tiengo 2007].

With this interpretation, we expect our distribution to depend on the filter. Starting from the Master file, we produce the count rate differential distribution for each optical filter. Figure 3.4 shows count rate DDF for each filter generated using the adaptive binning algorithm described in the previous section. Focusing on the high-count rate region, the DDF is quite similar for the Thin and Medium filter, while it is very different for the Thick filter as we expect. We isolate the flaring component in the DDF by selecting only the time bins where the *inFOV-outFOV* count rate exceeds 0.1 cts/s and we calculate their mean value as a proxy to quantify the intensity of this component. We measure this indicator for the distributions obtained with each filter and we obtain (1.92 ± 0.02) cts/s for the Thin filter, (1.48 ± 0.01) cts/s for the Medium and (0.74 ± 0.02) cts/s for the Thick filter. The mean count-rate of the flaring background component is thus reduced by more than a factor of two when the MOS2 detector uses the Thick filter, as expected in the soft-protons interpretation.

Conversely, if we focus on the low count rate region, which is dominated by the low-intensity background, we observe that the distributions look consistent in their Gaussian part (Figure 3.4, right panel). Our modelling does return different peak positions for the distribution obtained with each filter (Thin filter: 0.0173 ± 0.0002 cts/s, Medium filter: 0.0165 ± 0.0001, Thick filter 0.0196 ± 0.0003), possibly because of the degeneracies between the parameters of our modelling (Section 3.3.2). We note



however that even assuming the relative difference between peak positions for the filters to be significant, it is only ~15%, while the variation of the flaring component is larger than 100%. If the low-intensity component were associated to soft protons we would expect a much larger difference between the thin and medium filter data on one side and the thick filter data on the other.

This result suggests that the low-intensity component may have a different origin than the flaring component, as we will discuss in the next sections.

3.4 Evaluating systematic effects

Having identified a low-intensity component in the background distribution, we have to check if this may be explained by a systematic effect associated with the subtraction procedure. In the next sections we will evaluate systematics in order to validate the real presence of such background component in our data and to better understand its nature.

3.4.1 *inFOV-outFOV* distribution as a function of time

Figure 3.5 and Figure 3.6 show the count rate DDF for the *outFOV* and *inFOV*, respectively, using a count rate bin of 0.005 cts/s. Distributions were extracted from Master file using columns TIME, RATE_IN, ERATE_IN, RATE_OUT and ERATE_OUT.

*outFOV*DDF is characterized by two-peaks, with the first located at ~0.16 cts/s and the second at ~0.28 cts/s. Such distribution is associated with the modulation of unfocused background produced during solar cycles. The flaring background signal, characterized by high-count rate, is not seen in the *outFOV* as expected.

*inFOV*DDF shows two peaks at the same location of *outFOV* but with a very different relative intensity in favour of the peak at high count rates, because of the contribution of soft protons background. The flaring background signal is present in the distribution and dominates at high-count rate as expected.

If the low-intensity component of the *inFOV-outFOV* distribution is related to a systematic effect associated with the subtraction procedure we expect that its distribution will be different in the period of the two peaks, as we subtract in each period a different level of count rates.

From the Master file we extract *inFOV-outFOV* DDF corresponding to periods with a count rate in the *outFOV* between 0.14 and 0.17 cts/s (first peak), and to 0.26 and 0.29 cts/s (second peak). Figure 3.7 shows the two renormalized distributions focused on low count rate region.

As we expect from the different statistics in the two peaks the width of the distributions at low count rate is different, fitting the entire distribution with our empirical model we obtain a standard deviation value of 0.0266 ± 0.0001 cts/s for the first peak and 0.0308 ± 0.0001 cts/s for the second. For the peak positions, we obtain a best-fit value of 0.0129 ± 0.0002 for the first peak and 0.0162 ± 0.0002 for the second. As already discussed, the error bars on the peak position are underestimated and therefore the difference we found may not be significant and may result from the different shape of the distribution. Indeed, looking by eye at the distributions in Figure 3.7, we note that the peak positions seem to coincide and it is possible that our estimate of the best-fit peak position is affected by the degeneracy with the Gaussian width. Nonetheless, we cannot exclude that the difference is real, which possibly indicates a contribution from systematic effects in the background subtraction process. However, simple estimates indicate that if the peak were entirely due to systematic effects the shift in its position should be much larger.

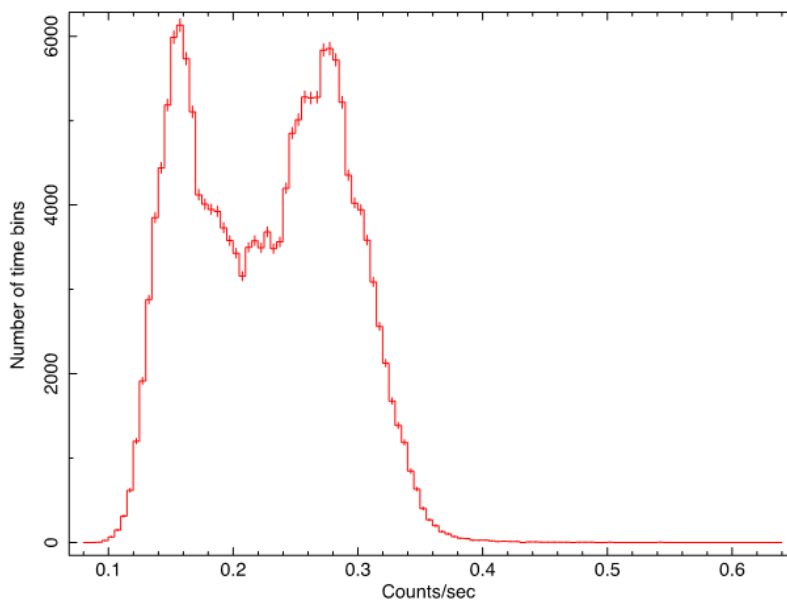


Figure 3.5: *outFOV* count rate differential distribution. The bimodal distribution is associated to the solar cycle.

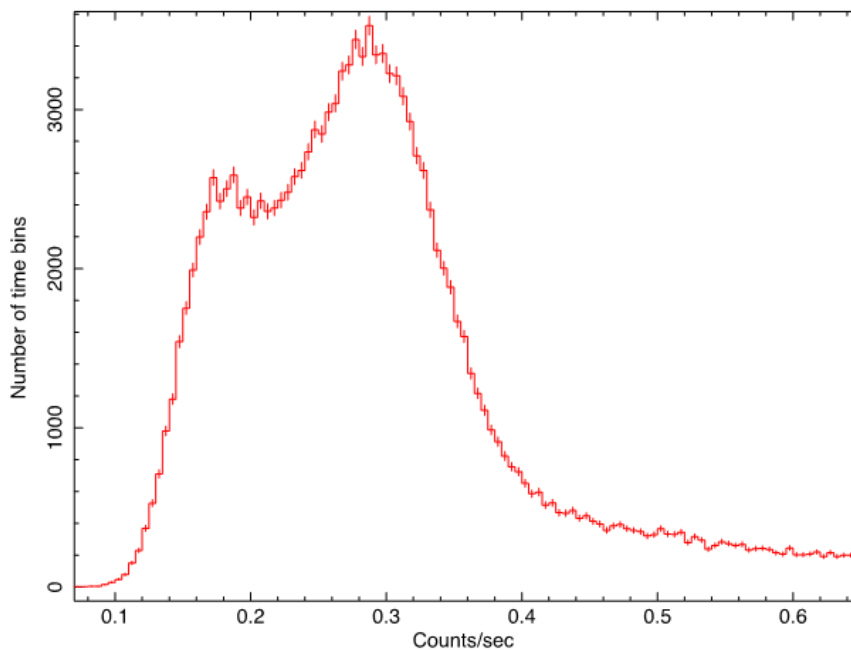


Figure 3.6: *inFOV* count rate differential distribution. The part at high count-rates (>0.7) due to the flaring component is not shown in the figure.

3.4.2 Closed exposures analysis

We further estimate systematics effects related to the subtraction procedure of *outFOV* data to *inFOV* by repeating our pipeline on a sample of observations performed with the filter wheel in *closed* position. In this configuration, an aluminium window prevents X-ray photons and low energy particles from reaching the detectors. Since the instrumental background dominates these exposures, we extract *inFOV-outFOV* light curves using the pipeline described in Section 3.2 to investigate and calculate a possible count rate excess in the *inFOV* region because of an inhomogeneous distribution of the internal instrumental background on the MOS2 camera.

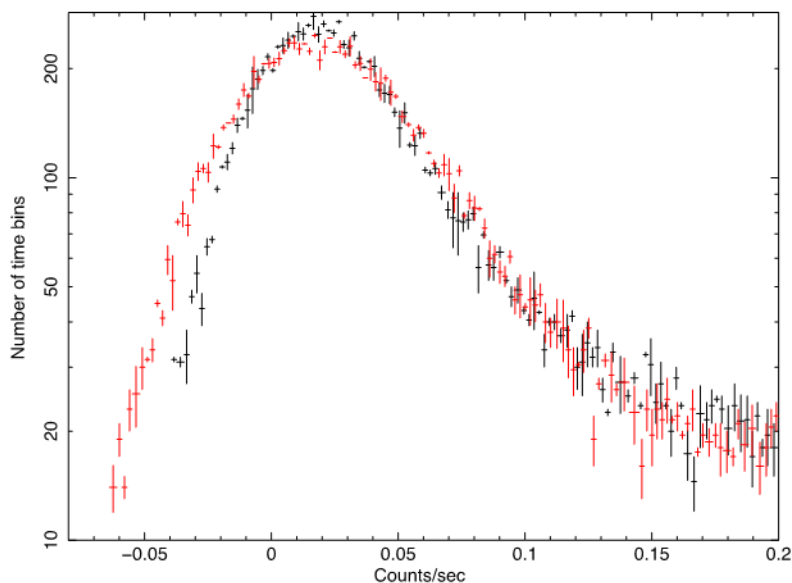


Figure 3.7: *inFOV-outFOV* count rate DDF during the period of two peaks in the *outFOV* DDF. The distribution referred to the period characterized by high count rate (second peak) is shown in red while the period characterized by low count rate (first peak) in black. The two distributions were renormalized in order to have the same peak value.

We have retrieved 72 *closed* observations (corresponding to 73 exposures) from the official list on the *XMM-Newton* web page⁷. We apply filters on events files based on PATTERN, FLAG and energy as performed previously for *non-closed* MOS2 exposures and we define the same *inFOV* and *outFOV* regions. The result of our automatic pipeline described before is a new Master file containing per each 500 sec bin time a number of information related to *inFOV* and *outFOV* light curves (see Section 3.2.3 for a more detailed description of parameters in the file). The exposure time in the entire *closed* data set is of ~1.43 Msec. Excluding “bad” time bins from the analysis following the approach described in Section 3.2.4, the exposure time decreases down to ~1.19 Msec.

⁷ http://xmm-tools.cosmos.esa.int/external/xmm_calibration/background/filter_closed/mos/mos2/mos2_FF_2016_v1.shtml

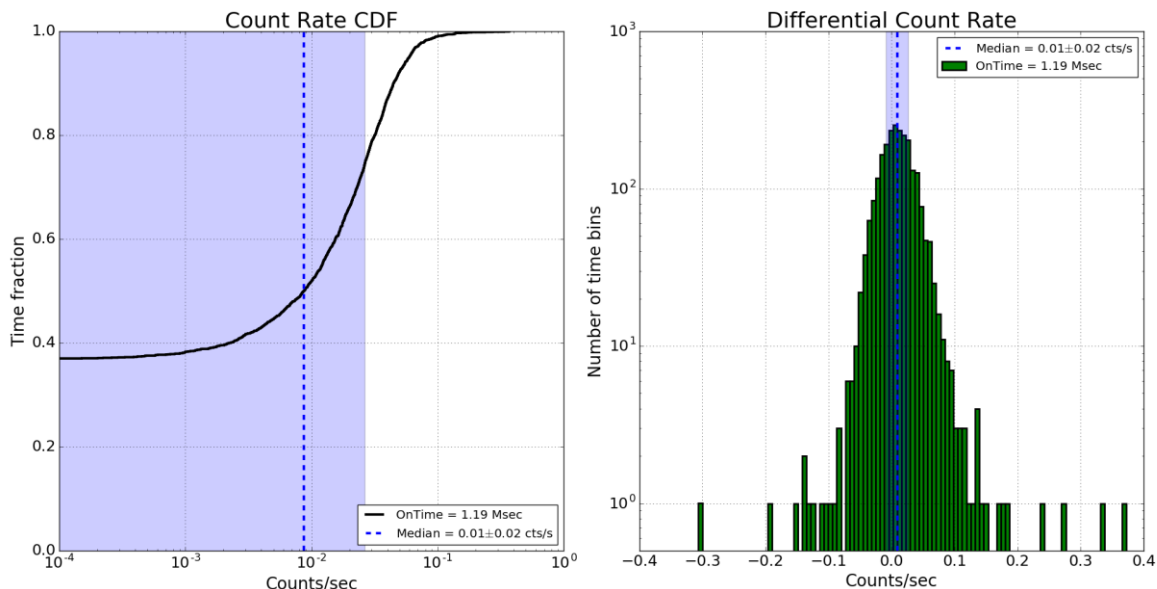


Figure 3.8: (Left) *inFOV-outFOV* count rate cumulative distribution function (CDF) for the closed exposures. Blue dotted vertical line shows the median, while the light blue span the median absolute deviation (MAD) defined in the text. (Right) *inFOV-outFOV* count rate differential distribution function (DDF).

From the closed Master file we create the *inFOV-outFOV* count rate cumulative distribution function (CDF) and the differential distribution function (DDF) (see Figure 3.8). Both distributions clearly show that there is no flaring background in *closed* exposures and only the Gaussian component at low count rates is detected. Fitting a simple Gaussian model to DDF distribution generated using our usual adaptive binning algorithm, we obtain that the best-fit mean value is 0.0085 ± 0.0006 , significantly different from zero, while the standard deviation is 0.0260 ± 0.0005 . This result shows an excess of count rate from instrumental background in the *inFOV* region. We have not investigated in detail the origin of such excess, but analyzing the integrated image containing all the *closed* exposures we assert that the major contribution may be due to the process of the electronic readout, which produces an asymmetric distribution of electronic background in each CCD in the direction of the readout nodes. Regardless of its origin, the presence of a significant excess in the *inFOV-outFOV* count rate distribution of closed observation clearly shows that some level of systematics is present in our analysis. The amplitude of this effect, as quantified by the peak position of the Gaussian, is about half of the low-intensity *inFOV* component that we found in our analysis of the EXTras dataset (Section 3.3).

We can consider the value of the peak position in the DDF distribution (0.0085 cts/s) as a rough estimate of the systematic error in the subtraction procedure. Considering that the rescaled *outFOV* intensity is ~ 0.02 cts/s, this corresponds to a relative error of 4%.

3.4.3 Discussion

The analysis presented in this section confirms that systematic errors play a role in the detection and modelling of the *inFOV* low-intensity component in the EXTras dataset. Indeed, our analysis of closed

observations suggests that systematic components account for about half of the amplitude of the Gaussian component of the *inFOV-outFOV* count rate distribution. While this result leaves the remaining half of this component as real, our incomplete understanding of systematics does not allow us to exclude that the low-intensity component may be entirely due to systematics. In the next section we will discuss a different approach to discriminate the nature of the low-intensity background on the basis of advanced spectral analysis.

3.5 Spectral analysis of the low-intensity and the flaring components

Spectral analysis of the data can provide further insight into the nature of the low intensity component discussed in the previous paragraphs. We have extracted spectra from the *inFOV* and *outFOV* regions for different levels of *inFOV-outFOV* intensity, to separate as much as possible contributions from the low intensity component and soft proton flares. For each filter we extracted 13 spectra, with the limiting *inFOV-outFOV* values shown in Figure 3.9 together with the *inFOV-outFOV* distribution. As we can observe in the figure, we have a sufficiently large number of spectra to follow the transition from the region dominated by the low intensity component to the one dominated by the flaring background.

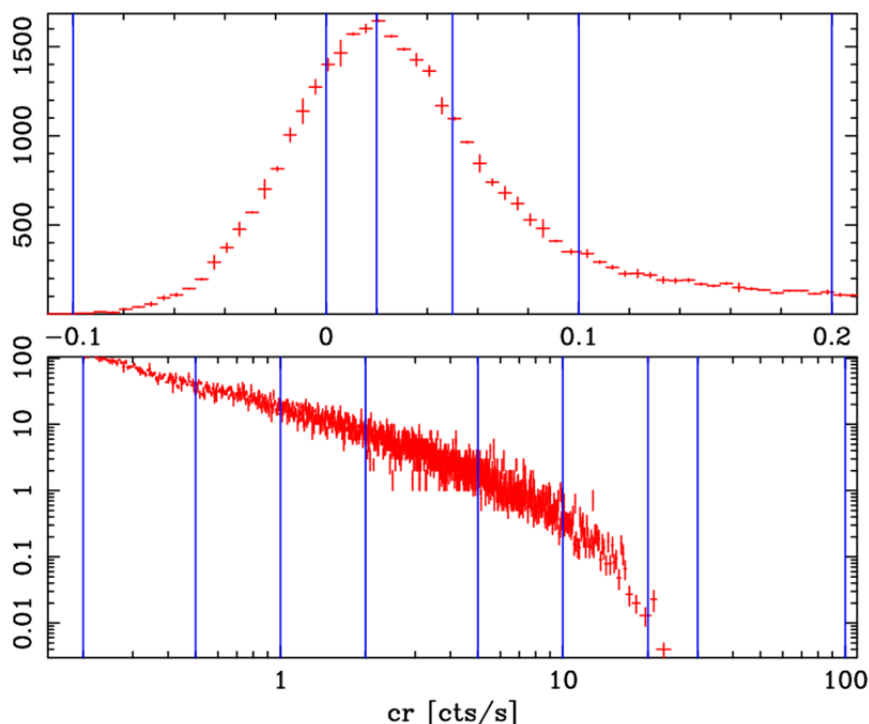


Figure 3.9: *inFOV-outFOV* count rate differential distribution function for the medium filter. Blue vertical lines indicate the ranges over which *inFOV* and *outFOV* spectra were extracted.

At variance with what we have done for the light curve analysis we have not subtracted the *outFOV* spectrum from the *inFOV* spectrum, but, as in Leccardi and Molendi [2008], we have worked with models. More precisely we have built a 4-components model comprising: 1) a first broken power-law component, **bkn1**, accounting for the high energy particle induced component observed both in the

inFOV and the *outFOV* regions; 2) a multi-gaussian component, **mgau**, accounting for the many fluorescence lines observed in the *inFOV* and the *outFOV* regions; 3) a second broken power-law component, **bkn2**, accounting for the excess emission observed in the *inFOV* region only and finally 4) a cosmic X-ray background component, **cxb**, for the cosmic X-ray emission observed in the *inFOV* region only. Fitting was performed simultaneously on each *inFOV* and *outFOV* spectra pair. Parameters for the **bkn1** component were forced to be the same for the two spectra, for the **mgau** component only energies were tied together while the normalizations were left to vary freely from one another to allow for variations of fluorescence lines across the detector. In Figure 3.10, we report, as an example, a fit to one *inFOV*, *outFOV* spectra pair.

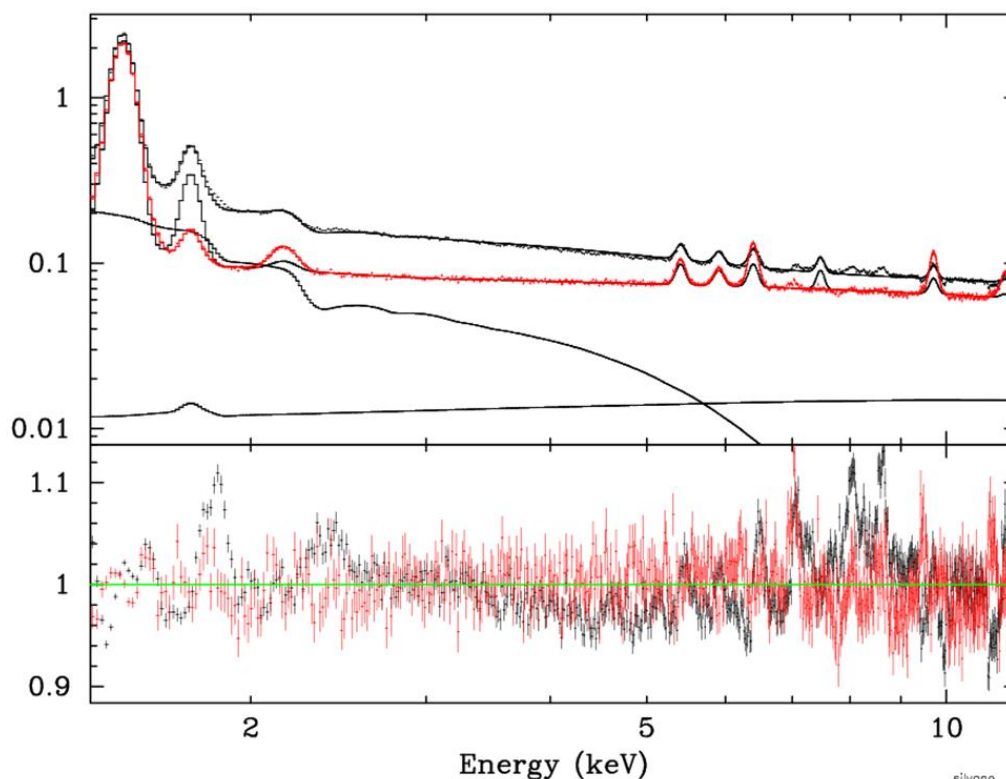


Figure 3.10: *inFOV* (black) and *outFOV* (red) spectra extracted for a specific choice of *inFOV-outFOV* intensity range. In the top panel we show the data along with the model and the most important components. In the bottom panel we show the residual of the fit in the form of a ratio of the data over model; note how: errors on data are in the order of a few percent, deviations are contained almost everywhere within a few percent.

Spectra fits such as the one shown in Figure 3.10 were performed for all spectra and for all filters. Once the analysis is performed, evolution of spectral parameters can be used to characterize the behavior of the various components. Since we are interested in the *inFOV* contamination, we have examined the **bkn2** component. In Figure 3.11 we show the variation of the high energy spectral slope of **bkn2** as a function of the ratio of the normalization of **bkn2** over **bkn1**, i.e. nrm_{bkn2}/nrm_{bkn1} . The first parameter describes the spectral shape of the *inFOV* contamination while the second is a measure of its intensity relative to that of the high energy particle induced component.

We can identify three different regions: a region associated to the peak (blue arrows in Figure 3.11) where the *inFOV* contamination is dominated by the low intensity component; a region at high count rates (black arrow in Figure 3.11) dominated by the flaring component and an intermediate region (red arrow in Figure 3.11) where both components contribute. As we can see from the top panel of Figure 3.11 in the first region the spectral slope is very flat, ~ -0.6 in the second it is much steeper, ~ 1 and in the intermediate region it undergoes a very rapid transition from one regime to the other. These results suggest that the low intensity and flaring components are different in nature. This is in agreement with what has been found from the analysis of the *inFOV-outFOV* distribution as a function of filter, see Section 3.3.3. This unexpected result has significant implications both in terms of our understanding of the XMM-Newton EPIC background and in terms of the role that soft protons and the low intensity component may have on the ATHENA background. A first discussion of these issues will be provided at the end of this section.

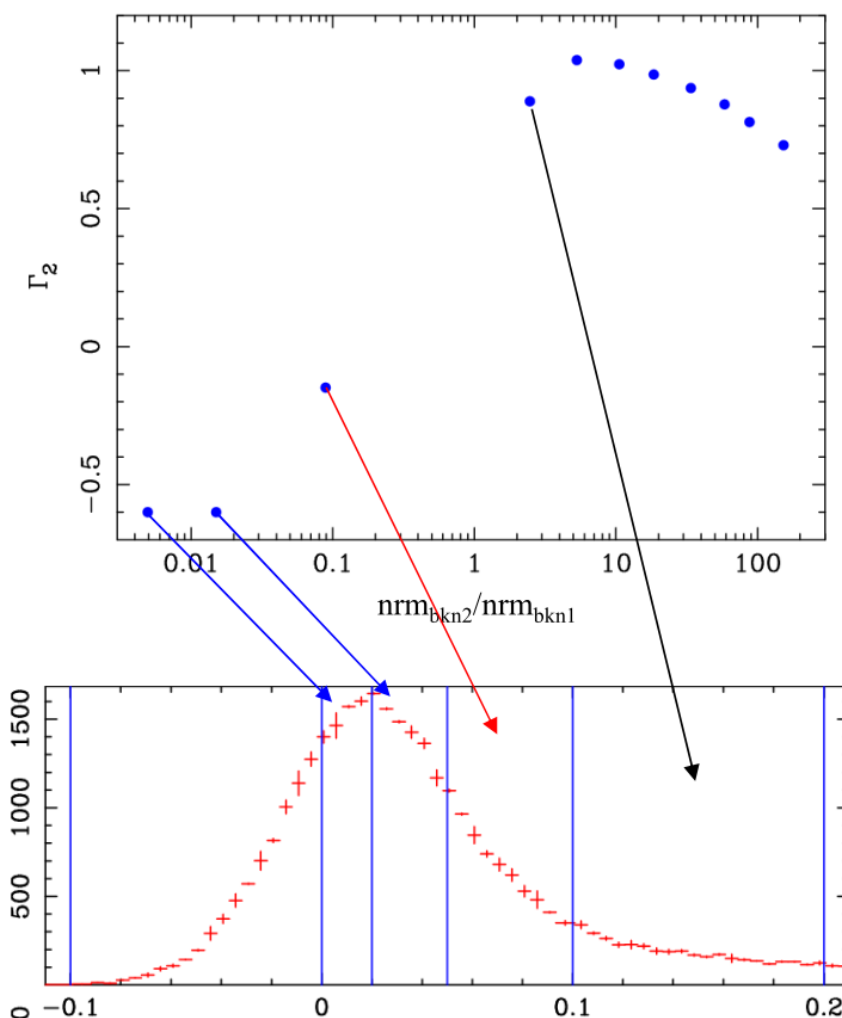


Figure 3.11: *Top panel*, high energy spectral slope of the *bkn2* component as a function of the ratio of normalizations of the *bkn2* and *bkn1* components. *Bottom panel*, differential distribution of the *inFOV* excess background. Note how the slope of the *bkn2* component rapidly changes as we move from the peak region, dominated by the low intensity component (blue arrows), to the high count rate region, dominated by soft proton flares (black arrow).

3.6 Evolution of the flaring and low intensity components through the mission

We want to test if the flaring background component and the low-intensity component show an evident evolution through the *XMM-Newton* mission and if such evolution is different for each component. Starting from the Master file, we have studied the *inFOV-outFOV* light curves dividing data per year. In this way we have extracted and analyzed count rate CDF and DDF for 13 years of mission, from 2000 to 2012. In addition, we have studied their spectral behavior to test the seasonal evolution. Obviously this is a simple approach that aims at investigating the background evolution on time scale of several years. A more accurate analysis that takes into account the behavior of the background as a function of the position of the satellite in the terrestrial magnetosphere will be discussed in Section 4.

3.6.1 Extraction of *inFOV-outFOV* count rate distribution per year

Figure 3.12 shows the *inFOV-outFOV* light curve for 13 years of *XMM-Newton* mission extracted from the Master file. The plot on the left shows the time evolution of the intensity and importance of SP flaring background component, while the plot on the right focuses on the time evolution of the low-intensity background component. We find some indication of evolution for the flaring component through the mission (more intense flares in the years 2003-2006) which may be associated to the solar activity. Conversely no clear variation of the low intensity component can be detected.

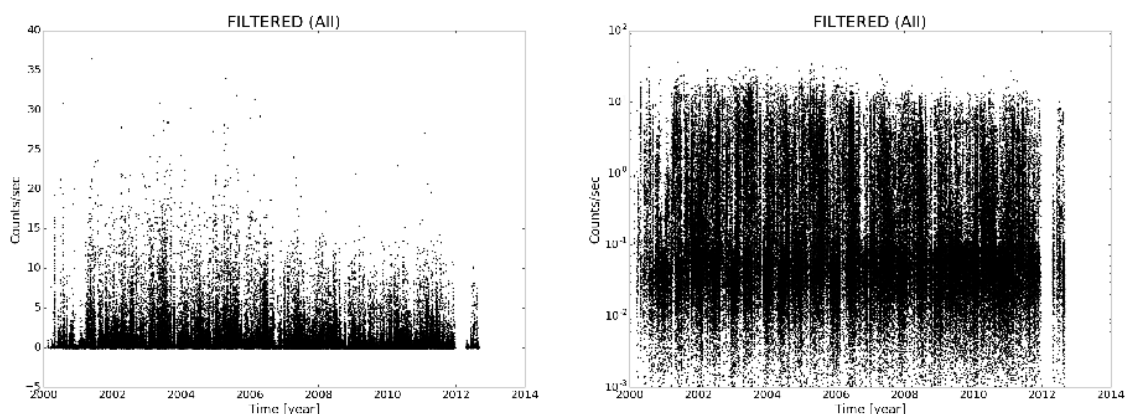


Figure 3.12: *inFOV-outFOV* MOS2 light curves for 13 years of *XMM-Newton* mission, from 2000 to 2012. (Left) Linear scale on count rate axis shows evidence for evolution of the flaring background through the mission. (Right) Logarithmic scale on count rate axis focuses on the low-intensity background component (located in the denser region).

3.7 Summary

In this sub-WP we have characterized the focused particles background on EPIC MOS2 camera on board of *XMM-Newton* telescope. The statistical quality of data is unprecedented, we have analyzed 13 years of observations, from 2000 to 2012, corresponding to ~195 Msec of data. We have used *outFOV* region as a calibrator to minimize any contamination from non-SP background components in the *inFOV* region. For this reason we have produced and studied *outFOV*-subtracted *inFOV* light curves with a time bin of 500 sec. Excluding from the analysis “bad” exposures and time bins, our final data set is roughly 90 Msec.

Analyzing the count rate cumulative distribution function of *inFOV-outFOV* light curves we have measured the fraction of time dominated by the flares in *XMM-Newton* MOS2 is about 35% (~30 Msec).



The count rate differential distribution function shows two components in the background: a high count-rate flaring component and a low-intensity gaussian component. .

The flaring component shows evidence of seasonal evolution (Section 3.6) and its intensity is different for observations obtained with different filters (Section 3.3.3), consistently with the current interpretation that it is due to soft proton flares. Concerning the low-intensity component, we have not detected seasonal variations (Section 3.6) or a significant dependence on the filters (Section 3.3.3). Moreover, it has a different spectral shape than the flaring background. While we have significant indications that at least part of this component may be due to systematics (Section 3.4), the physical origin of this component is still unclear and we cannot exclude at present that it is fully due to systematics. Nonetheless, its different behaviour with respect to the flaring component in terms of time evolution, spectral shape and filter dependence, suggests that the two components have different origin. The evidence we now have is enough to state that the low intensity component is not due to a population of quiescent soft protons focused by the mirrors, challenging its most common interpretation [e.g. De Luca & Molendi, 2004, Leccardi & Molendi 2008, Kuntz & Snowden 2008]. This result has important implications for the background modelling in XMM-Newton data analysis and for the forecast of soft proton contamination for Athena.



4 SPB2: IMPACT OF THE MAGNETOSPHERIC ENVIRONMENT ON THE XMM-NEWTON BACKGROUND

4.1 Introduction

XMM-Newton orbit is elliptical and highly eccentric, with an apogee of about 115000 km and a perigee of about 6000 km from Earth. While traveling along its orbit, the satellite transits through the Earth magnetosphere, the region around the Earth influenced by its magnetic field. Different regions of the magnetosphere can have very different environmental conditions, depending on the strength and the orientation of the magnetic field, the speed and the density of the particles etc. The different conditions encountered by XMM-Newton can, in principle, differently affect the particle background detected by EPIC instruments. Thanks to its highly elliptical orbit, XMM-Newton crosses these different magnetospheric environments, from the radiation belts near the perigee, through the magnetoplasma and magnetotail, to the magnetosheath and eventually out of the bow shock into the solar wind. XMM-Newton data are therefore very useful to test the dependence of the induced particle background and of the soft proton flux in different magnetospheric environments.

The aim SPB2 sub-WP is to study the influence of the magnetospheric environment on the focused particles background detected by EPIC. More specifically, we will estimate the variation of the two background components identified in Section 3.3.2 along the XMM-Newton orbit.

4.2 The dataset

We adopt the large XMM-Newton data sample described in Section 2.2, which includes observations performed between 2000-2012 from revolution 35 to 2330. We apply the same filtering and cleaning procedure described in Section 3.2.4. In addition, we reject periods where solar energetic particle (SEP) can affect the measurements. SEP events are related to solar flares and mass coronal ejection and occasionally they can induce a notable increase of the EPIC background level. The influence of SEP on the EPIC background will be extensively addressed in UPB2 sub-WP (Section 8) and the induced contamination is not systematic and obvious. We use the ESA Solar Energetic Particle Environment Modelling (SEPTEM) application server⁸ (see Section 8.3) to obtain the list of all SEP contaminated periods and excluded them from our dataset. After the removal of the time intervals affected by SEP events, the sample reduces to 87.8 Msec of cleaned data.

4.3 Method

4.3.1 Partition of the magnetosphere into magneto-zones

The terrestrial magnetosphere prevents most of the solar wind from hitting the Earth, although some energetic particles can enter it. In Figure 4.1, (left panel), we provide a schematic representation of the Earth magnetosphere. The outermost layer of the magnetosphere is the *bow shock*; it forms when the supersonic solar wind encounters the Earth magnetic field. The solar wind across the bow shock surface is then heated up and slowed down by the Earth's magnetic field, which acts like an obstacle. As a consequence, the solar wind starts flowing around the obstacle forming the *magnetopause*, a surface which divides the terrestrial magnetic field from the solar wind that flows around it. Along the magnetopause surface, the pressure of the Earth magnetic field is balanced by the pressure of the solar wind.

⁸ http://dev.sepem.oma.be/help/event_ref.html

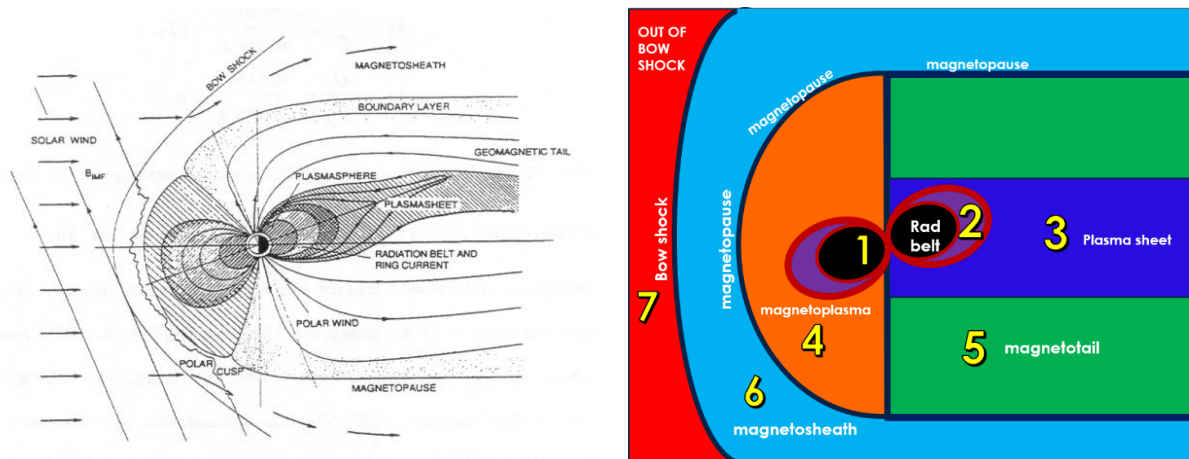


Figure 4.1: A schematic view of the magnetosphere of the Earth (*left panel*) and our simplified division of the magnetosphere into 7 magneto-zones (*right panel*). The color code represented here will be adopted throughout the report.

We adopt a simplified characterization of the Earth magnetosphere (see Figure 4.1, right panel) and divided the magnetosphere into 7 typical magneto-zones whose detailed description is provided in the following subsections. The color code shown in this figure is adopted throughout the report to distinguish the different magneto-zones.

4.3.1.1 Radiation belts: magneto-zone #1 and #2

The Van Allen *radiation belts* are the innermost part of the magnetosphere in which energetic charged particles are trapped inside the Earth's magnetic field and spiral around the field lines. The belts shape mostly follows the dipole magnetic field lines that can be described using the *L-shell model* by McIlwain [1961]:

$$R = L \cos^2 \lambda$$

where R is the radial coordinate of the field line in units of Earth radii ($R_E = 6371$ km), λ is the magnetic latitude and the L-shell parameter is defined:

$$L = \frac{R_0}{R_E},$$

and R_0 is the intersection of the field line with the geomagnetic Equator. Variables are defined in the geocentric solar magnetospheric system (GSM). The inner radiation belt extends in the range $L = 1.5 - 2.5$ and is relatively stable whereas the outer belt is extremely dynamic with an external edge varying from $L = 4$ to $L = 6$. Since the boundary is highly variable, it is not straightforward to define the edge of this magneto-zone. Therefore we split it into two different zones: we dub "radiation belts" (labelled as magneto-zone #1) the regions inside the $L = 4$ shell: these regions are surely embedded into the radiation belts; then we define the transition region, with L between 4 and 6 as "radiation belts exit" and label it as magneto-zone #2: somewhere in this region, the satellite exits the belts and enters the outer magnetospheric ambient.



4.3.1.2 Plasma sheet: magneto-zone #3

The *plasma sheet* (magneto-zone #3 in our classification) is a layer of weaker magnetic field and denser plasma located in the nightside (anti-Sunward direction) of the magnetosphere. Solar wind protons and electrons diffuse across the magnetopause in the magnetotail (see Section 4.3.1.3); the electric field across the tail causes them to drift towards the plasma sheet, and finally accelerate them Earthward. The plasma sheet shape is complex but, close to the Earth, is typically 10-12 R_E thick [Rosenqvist 2002]. We adopt a very simple model assuming it is a cylindrical region centered on the Earth-Sun line, with the axis parallel to the ecliptic plane in the anti-Sunward direction, with radius $R = 5 R_E$.

4.3.1.3 Magnetoplasma and magnetotail: magneto-zones #4 and #5

Inside the magnetopause, the magnetic field lines have a different shape on the nightside and dayside regions. In the dayside region, magnetic field lines are closed (see Figure 4.1, left panel). Field lines, here, resemble the dipole L-shells field lines of the radiation belts, but are significantly distorted and compressed by the pressure of the solar wind. Conversely, in the nightside regions the magnetic field lines are stretched and open.

We divide the area inside the magnetopause into two different sectors (labelled as #4 and #5). The anti-Sunward region is known as *magnetotail* (#5) and we dub "*magnetoplasma*" the Sunward zone (#4). To model these regions, we use a simple model [Kuntz and Snowden, 2008] for the magnetopause radius in the dayside direction

$$R_{MP} = \frac{14.21}{1 + 0.42 \cos \theta}$$

where the distance R_{MP} is in R_E units and θ is the angle from the Earth-Sun line. Coordinates are in the geocentric solar ecliptic (GSE) system. The Sunward magnetopause distance is about $R \sim 10 R_E$. On the nightside, we assume the magnetopause to be a cylindrical surface, with radius $R = 14.21 R_E$, with the cylinder axis parallel to the ecliptic plane and centered on the Earth-Sun line.

4.3.1.4 Magnetosheath: magneto-zone #6

The *magnetosheath* is the plasma region between the bow shock and the magnetopause in which the shocked solar wind is heated and slowed down from supersonic to subsonic speeds. The decelerated particles are deflected and flow around the magnetopause surface. The boundaries for this magneto-zone (labelled as #6) are the magnetopause surface (defined in the previous paragraph) and the bow shock surface that we model following Kuntz and Snowden [2008]:

$$R_{BS} = \frac{22.74}{1 + 0.75 \cos \theta}$$

where the distance R_{BS} is in R_E units and θ is the angle from the Earth-Sun line. On the Sunward side, the distance of the bow shock from the Earth is $\sim 13 R_E$.

4.3.1.5 Out of the bow shock: magneto-zone #7

We finally label as magneto-zone #7, the regions *out of the bow shock* when the satellite is outside the magnetosphere and embedded in the solar wind. The description used in our analysis for the magnetosphere is clearly simplified. Apart the oversimplified modeling adopted, we should keep in mind that the magneto-zones shapes and boundaries can significantly vary in time. The plasma sheet on occasion sashes and flaps around; solar wind speed and pressure variation can compress the magnetopause and bow shock surfaces changing their boundaries. Solar wind pressure varies with time both through the long-term change which occurs over the 11-years solar cycle and through short-term sporadic phenomena like solar flares and coronal mass ejections. All these variations are responsible for changes of the magneto-zones shapes and boundaries that we neglect in our mode. It should also be noted that region boundaries are not sharp edges and these zones are not strictly distinct, instead there may be smooth transitions from one region to another. However, also thanks to the very large quantity of data available, this simple description of the magnetosphere is appropriate to study in a statistical way how the various magnetospheric conditions can affect the XMM particle background.

4.3.2 XMM-Newton orbit segmentation

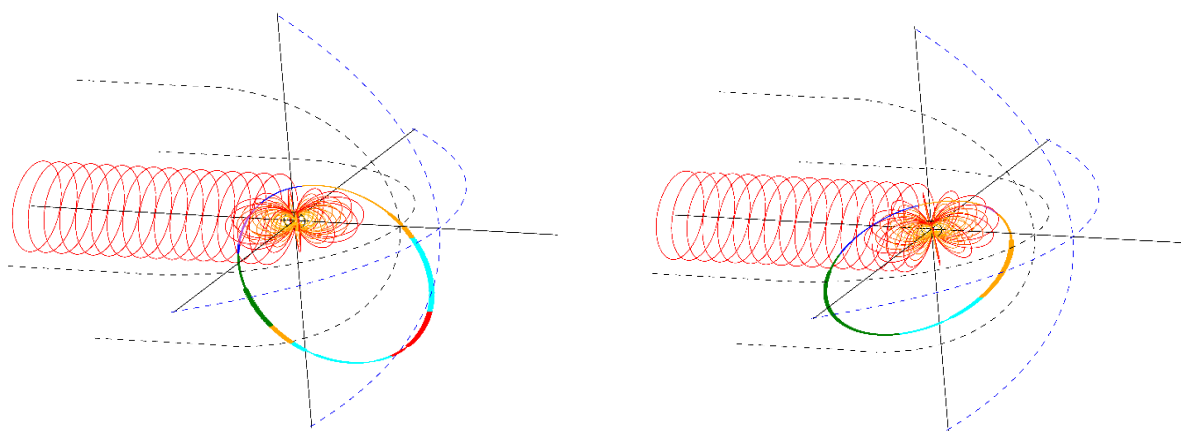


Figure 4.2: XMM-Newton orbit for revolution 1016 (*left panel*) and 1466 (*right panel*). The coordinate grid is in Geocentric Solar Ecliptic (GSE) coordinate system, with the Earth in the origin and the Sun located at the end of the X-axis at the right-side of the plot; XY plane is the ecliptic plane. Distances are in R_E units. Radiation belts (closed lines around the Earth) are plotted for L in the range L= 2(yellow) to L=6(red) with colors with orange tones for intermediate values of L. Red circle mark the plasma sheet and black and blue dashed lines are the projection of the magnetopause and bow shock surface respectively. The XMM-Newton orbit segments are plotted using the color codes defined in Figure 4.1.

Our sample includes data from revolution 35 to 2330. For each revolution, we derive the XMM-Newton orbit using the information available in the Radiation Monitor page of the XMM-Newton website⁹, where fits files containing orbit parameters can be retrieved. These files are obtained through the SAS 'orbit' task and provide the XMM-Newton orbit status with a 1 second cadence but their processing for the

⁹ <https://www.cosmos.esa.int/web/xmm-newton/radmon>

entire archive can be very time-consuming. When available, we used Trend Data in HEASARC10, as they store XMM orbit parameters with a 64 sec cadence. We thus use Radiation Monitor orbit files only when Trend Data are missing.

We split each XMM orbit into segments according to the magnetosphere environment crossed while travelling. Then, for each revolution and for each magneto-zone we find the Good Time Intervals (GTI) that can be used to filter the sample data and analyze the background region by region.

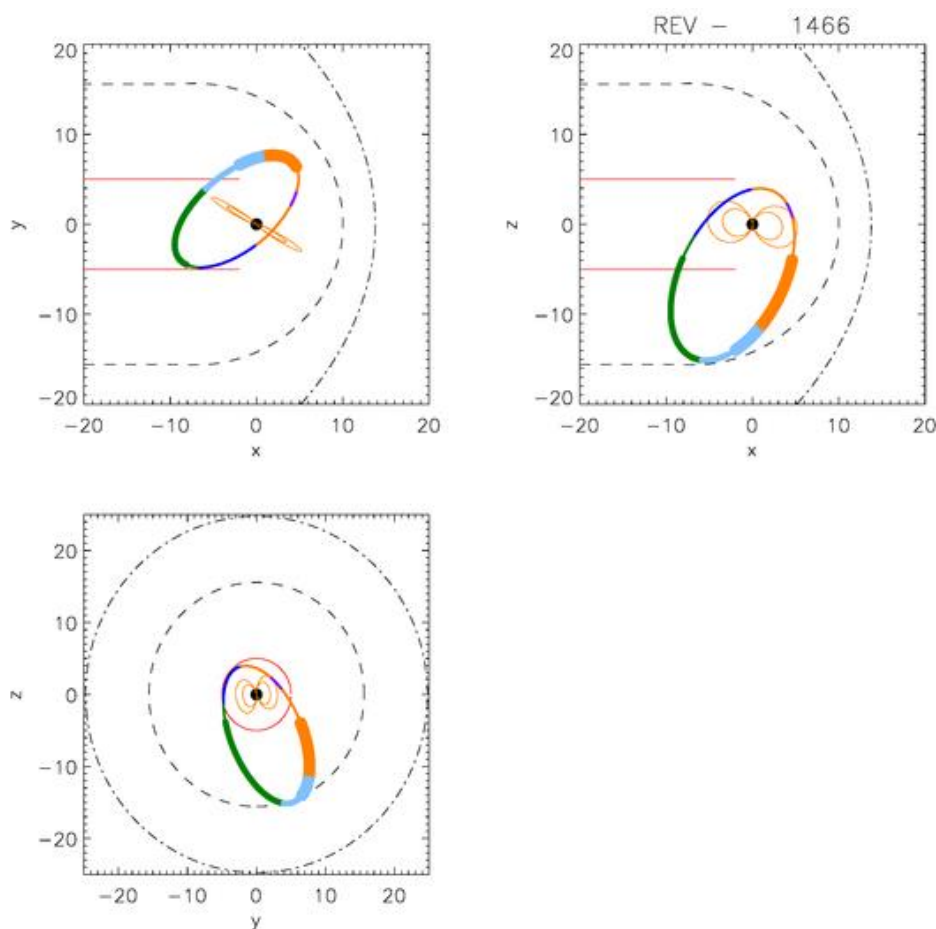


Figure 4.3: 2D projections of XMM orbit for revolution 1466. Closed orange lines around the Earth mark the L=2 and L=6 radiation belts. Red lines delimit the area of the plasma sheet. Dashed and dot-dashed black lines trace the magnetopause and the bow-shock surface respectively. XMM-Newton orbit segment are plotted using the color code defined in Figure 4.1. The thick portions mark the orbit parts where EXTrAS data are available.

We segmented the XMM-Newton orbits by intersecting them with the magneto-zone edges. In Figure 4.2 we plot, as an example, a 3D representation of the XMM-Newton orbits during revolution 1016 (26-27 June 2005) and revolution 1466 (10-11 December 2007). 2D projections for revolution 1466 are also reported in Figure 4.3 for a better visualization of the orientation of the orbit. In both figures, closed lines around the Earth track the torus of the radiation belts, useful to show the orientation of the belts in that orbit: the orientation of radiation belts varies in time due to seasonal and daily motion of the Earth's dipole tilt angle. To derive changes in the magnetic axis inclination, we use the SolarSoftware (SSW) IDL package [Freeland and Handy, 1998], where the dipole axis position is calculated according to the

¹⁰ https://heasarc.gsfc.nasa.gov/docs/xmm/xmmhp_trend.html

International Geomagnetic Reference Frame (IGRF) model, as described in Fränz and Harper [2002]. In Figure 4.2, the plasma sheet cylinder is represented through a series of red circles, extending in the anti-Sun side; dashed black lines are the projections of the magnetopause surface on the XY and XZ planes; blue dashed lines are the projections of the bow shock surface. Projections for plasma sheet, magnetopause and bow shock are also plotted in Figure 4.3. In the bottom panel (projection on the YZ plane), the radii for the circles are chosen to illustrate the maximum extension of the three surfaces, when seen from the Sun.

The orbit segments are plotted using the color code defined in Figure 4.1 and the orbit parts where EXTrAS data are available are plotted with a very thick line. EXTrAS data generally cover only a fraction of the orbit. This is also clearly visible in Figure 4.4 where we plot the timeline for the same revolutions; perigee is considered as starting point of the orbit. In the bottom panels we report in colored boxes the observations slots during each orbit and periods where Trend Data are available (black thick line). The middle panels show the EXTrAS lightcurves. The lack of data during the revolution can be due to various reasons. First of all, EPIC cameras are closed at low altitudes to avoid damage from exposure to soft protons during the passages through the radiation belts: XMM has a minimum observation altitude of 40,000 km. This is responsible of missing data at the beginning and at the end of each orbit. Observations can be missing for corrupted or bad data or could have been rejected from the EXTrAS archive (see Section 3.2.4). In addition, gaps are present during slew transitions from an observation target to another.

Parts of the orbits where Trend Data are available are plotted with a medium thickness line in Figure 4.2 and Figure 4.3, and are reported in the bottom panels of Figure 4.4 (black thick line).

The top panels of Figure 4.4 show the Radiation Monitor lightcurve. Radiation Monitor, unlike EPIC instruments, is generally operative throughout the whole orbit.

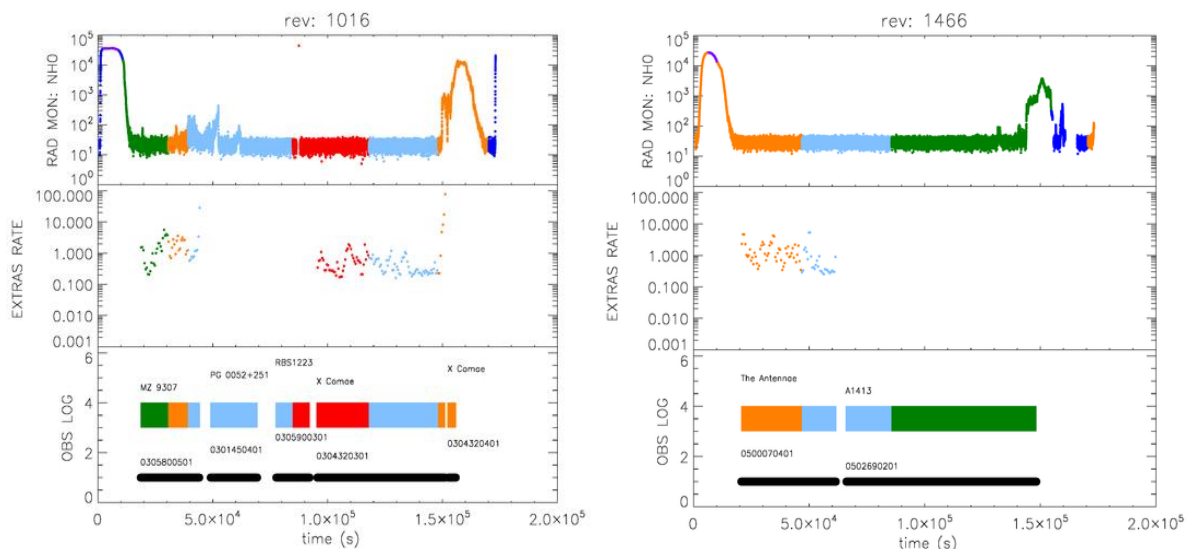


Figure 4.4: Timeline for orbits #1016 and #1466. Top panels show the Radiation Monitor lightcurve. In the middle panels we report the EXTrAS rate along the orbit. Bottom panels include general informations about the revolution: observations ID, observation targets and (thick solid black lines) intervals where Trend Data in HEASARC archive are available. Different regions are color coded as in Figure 4.1.

XMM-Newton orbit has an inclination of about 40 degrees, slightly variable in time. Figure 4.2 and Figure 4.3 show that it lies north of the ecliptic plane only when it is near to the perigee. Then the orbit extends south of the ecliptic plane where the satellite spends most of the time. The direction of the orbit and the apogee position change during the year. Depending on the season, the orbit extends toward the Sun, with the apogee eventually exiting the bow shock surface (like in the left panel of Figure 4.2) or in the anti-Sun direction, keeping completely inside the magnetotail and the magnetosheath (right panel of Figure 4.2).

Figure 4.5 shows the full lightcurve of the whole EXTraS sample, with colors marking the different magneto-zones. In the first observation years, the out-of-bow-shock region (in red) is periodically reached during the summer periods. Successively, namely after July 2005, the satellite is no more able to reach this region, due to a gradual circularization of the orbit and to variations of its inclination angle.

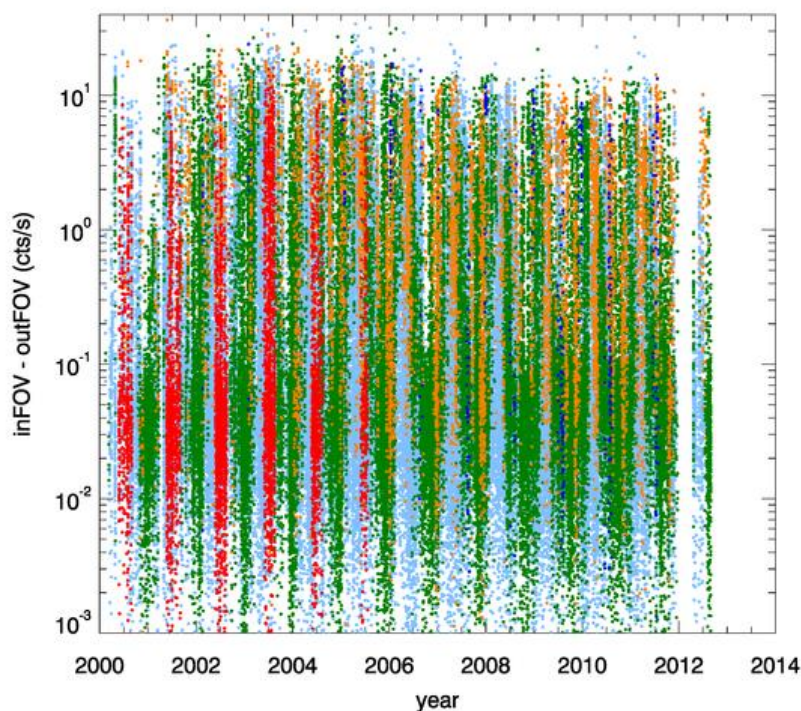


Figure 4.5: Lightcurve of the whole EXTraS archive. Colors mark the different magneto-zones following the color codes of Figure 4.1.

It is also worth noting that the XMM-Newton orbit precesses, so that, while in the first years of the mission, XMM-Newton apogee is located in the Sunward direction during the summer time, in the last years the situation is reversed with the apogee facing the Sun in winter.

During the 13 years under analysis XMM recursively crosses all the magneto-zones. The fraction of time spent in each ambient depends on the orbit geometry and inclination and on the extension of each zone. In Table 4.1 we report also the time (and fraction) spent in each magneto-zone and the corresponding amount of EXTraS data. Particularly interesting is the out-of-bow-shock region (#7), where the satellite is out of the Earth magnetosphere.

XMM-Newton spent in the out-of-bow-shock zone only 4.2% of the time with 3.7 Msec of EXTraS data in this region. Most of the time is spent into the magnetosheath and the magnetotail. Little time is spent into the plasma sheet. Because of its position (in the nightside and along the ecliptic plane) and its



thinness, the plasma sheet hosts the satellite only for about the 5% of the time with only 5 Msec of data available. Due to required off time near the perigee, no data are available in regions #1 and #2. These two magnetospheric regions will not be discussed further in this report.

Table 4.1: We report the total time (and the corresponding fractional value) spent by XMM–Newton in the different magnetospheric zones. We show both the time scored by the Radiation Monitor (which roughly corresponds to the total time effectively spent in each region) and the total time (with the corresponding fractional value) of EXTras data available in the same region.

Magneto-zone	RADIATION MONITOR		EXTras archive	
	TIME (Msec)	Fraction (%)	TIME (Msec)	Fraction(%)
#1 Radiation belts	3.3	0.9	0.0	0.0
#2 Radiation belts exiting	13.2	3.4	0.0	0.0
#3 Plasma sheet	20.3	5.2	0.4	0.5
#4 Magnetoplasma	58.4	15.0	5.1	5.8
#5 Magnetotail	126.1	32.5	35.6	40.5
#6 Magnetosheath	154.7	39.8	43.0	49.0
#7 Out of bow shock	12.4	3.2	3.7	4.2

4.4 Results

4.4.1 Soft protons rate, low-intensity background, and magnetospheric environment

We use the *inFOV-outFOV* rate to estimate the EPIC background (see Section 3.2.2). Starting from the light curve of the whole EXTras sample, we derived the *inFOV-outFOV* rate versus the orbit phase (Figure 4.6); each orbit light curve has been plotted versus the time elapsed from the perigee position. As usual, colors mark the different magnetic zones. The figure gives a qualitative picture of the EPIC *inFOV* excess background along the orbit. We can recognize the twofold behavior of the background. Many events feature a high (say ≥ 0.1 cts/s) *inFOV-outFOV* rate which can occasionally rise up to ~ 200 cts/s; these correspond to soft proton flares. However, the bulk of the data lies in the range $[0.01 - 0.1]$ cts/s where the low-intensity component of the background (discussed in Sections 3.3.2 and 3.4.3) dominates. Although the nature of this component is still matter of debate, we are reasonably certain that it is not associated to soft protons.

Since the perigee is the starting (and ending) point of the orbit, at the center of the plot, in the middle of the orbit we find the events recorded at the apogee: here are concentrated the “out of bow shock” data (in red). Apparently, the *inFOV-outFOV* rate here is slightly lower than in the other regions, with a lower spread of data, although not free from soft protons flare events. On the contrary, the figure shows that soft proton flares are found in all magnetozones and are not associated only to some peculiar magnetospheric regions.

The plasma sheet (blue dots) is “populated” only at the beginning and at the end of the orbit, near the perigee. Due to the high variability of the radiation belts edge, data referring to this region are possibly contaminated by the belts. The *inFOV-outFOV* rate seems on average larger than elsewhere and the quantity of data in this region is low since the time spent here is only 0.4 Msec.

Orange dots, labeling the magnetoplasma on the dayside, are also located at the edges of the plot at the beginning and at the end of the orbit. Indeed, the satellite lies in this area just after exiting (or before entering) the radiation belts when the orbit extends Sunward; the pressure of the solar wind produces a compression of the magnetosphere on the dayside, thus reducing the thickness of the magnetoplasma, about 20000 km between the edge of the radiation belts (~ 40000 km of altitude) and the magnetoplasma (~ 60000 km, in the Sun direction). XMM-Newton spends in this region only a small

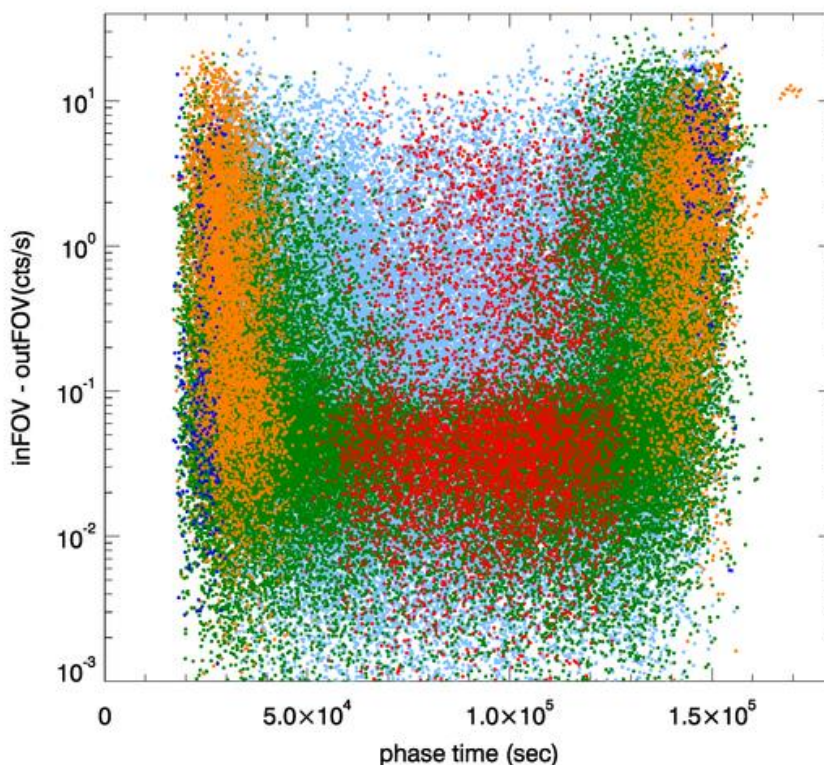


Figure 4.6: *inFOV-outFOV* rate of the whole EXTras sample versus the phase time. For each orbit, the phase time is the time measured starting from the beginning of the orbit. The orbit is assumed to start at perigee. Colors mark the different magneto-zones following the color codes of Figure 4.1.

fraction of time (~6%, i.e. ~5 Msec). Also for this region, the *inFOV-outFOV* rate seems slightly higher than in the other more external zones.

To quantify the variation of the *inFOV-outFOV* rate in the different magnetospheric ambients we report in Figure 4.7 the distributions of *inFOV-outFOV* rate for the five considered zones. Distributions on the left column are zoomed to low (within the [-0.1, 0.3] range) *inFOV-outFOV* values for a better visualization of the low-intensity component. The distributions show the presence of two main contributions: 1) the peaked Gaussian-like distribution at low count rates describes the low-intensity component where the bulk of the data lies; 2) all the distributions feature a long tail toward high count rate values, representing the flaring component. The wide extension of the tail is a symptom of the importance of the flaring component, which, in all the magnetospheric regions, accounts for a notable fraction of events: indeed the fraction of time when the background is affected by soft protons flares is $\geq 30\%$ (Section 3.3).

In all the panels of Figure 4.7, we overplot the best fitted empirical distribution defined in Section 3.3.2 where a Gaussian function is adopted to describe the low-intensity component and a modified-Lorentzian function provides a description of the tail. The statistics is good in regions #5, #6, and #7 (magnetotail, magnetosheath and out-of-bow-shock) that collect most of the data. The obtained best-fit functions describe accurately the *inFOV-outFOV* distributions in these regions and the best fit parameters are well constrained. However, as already discussed in Section 3.3.2, there is significant correlation between the different parameters and the purely phenomenological nature of the adopted model requires that we consider uncertainties on model parameters with some caution.



The statistics in region #3 (plasma sheet) is very low and the obtained curve hosts some artificial features that the fitting procedure introduces to follow distribution irregularities. Best-fit values for this region, albeit with small error bars, are not reliable from a physical point of view and we cannot use them to draw any conclusion.

As discussed in Section 3.3, the Gaussian peak derived from the fitting procedure is suitable to quantify the low-intensity component contribution in the different magnetospheric ambients. On the contrary, the best-fit parameters of the Lorentzian component provide an empirical description of the distribution but do not have any physical significance and cannot be used to quantify the intensity of the flaring component into the various magnetozones. To quantify the intensity of the latter component, we use the mean of the high-rate-component. We choose as fiducial threshold 0.1 cts/s and we calculate the mean value of the *inFOV-outFOV* rate above this threshold and we refer to it as the flaring mean rate (Section 3.3.3). The Gaussian peak values and the flaring mean rate for each magnetozone are reported in Table 4.2.

Table 4.2: Gaussian peak positions obtained fitting *inFOV-outFOV* with function defined in Section 3.3.2; means for high count rates (*inFOV-outFOV* > 0.1) in the different magnetospheric regions.

Magnetozone	Gaussian Peak	Flaring mean rate(<i>inFOV-outFOV</i> > 0.1)
#3 Plasma sheet	0.014±0.003	4.075±0.233
#4 Magnetoplasma	0.039±0.001	2.425±0.037
#5 Magnetotail	0.0179±0.0001	1.700±0.020
#6 Magnetosheath	0.0165±0.0001	1.544±0.015
#7 Out-of-bow-shock	0.0168±0.0002	1.522±0.048

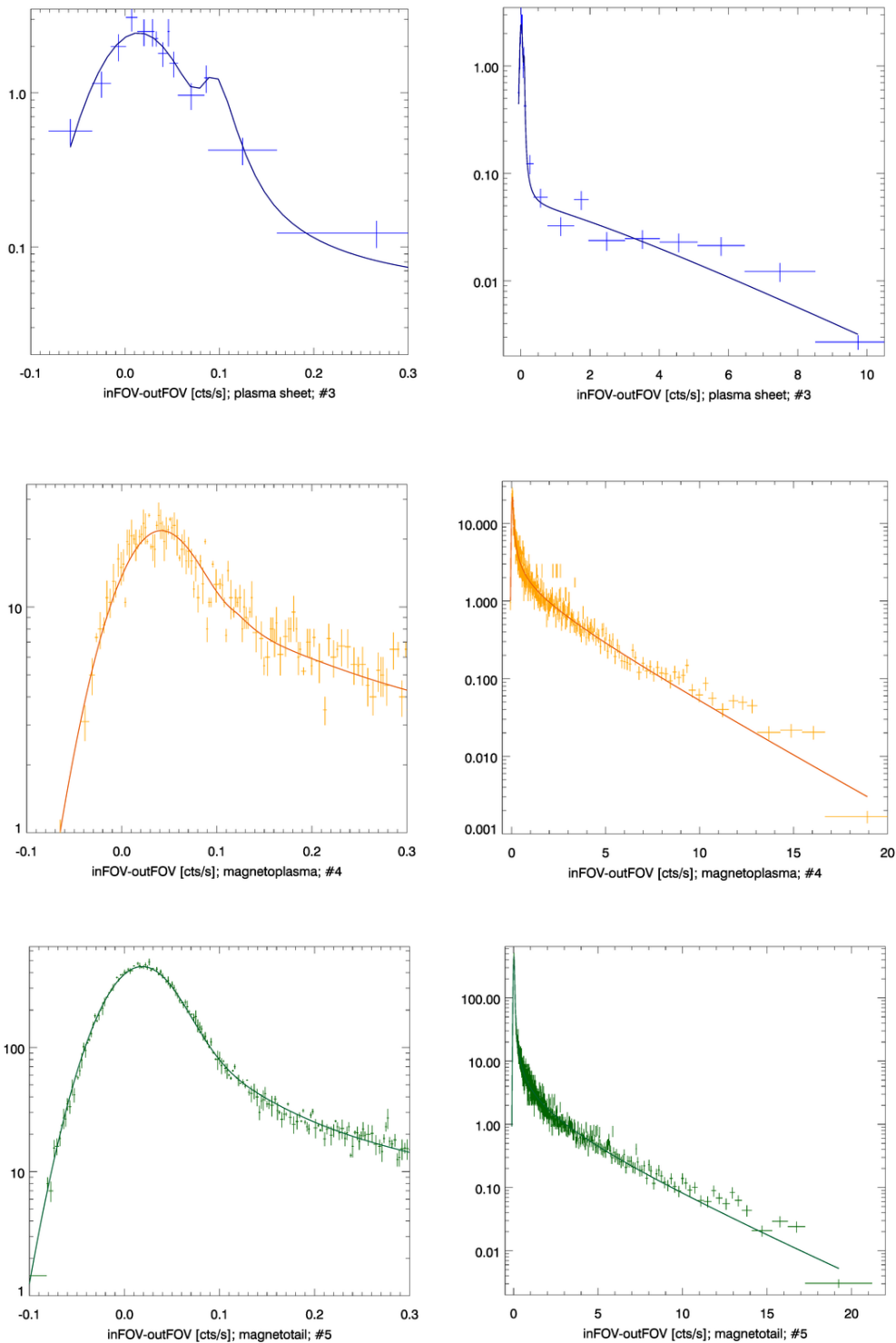


Figure 4.7: *inFOV-outFOV* distribution for each magnetozone. Distributions in the left column are zoomed in the range [-0.1, 0.3] for a better visualization of the low-intensity component. Best fit functions described in Section 3.3.2 are overlotted. Different regions are color coded as in Figure 4.1. (Continues in next page)

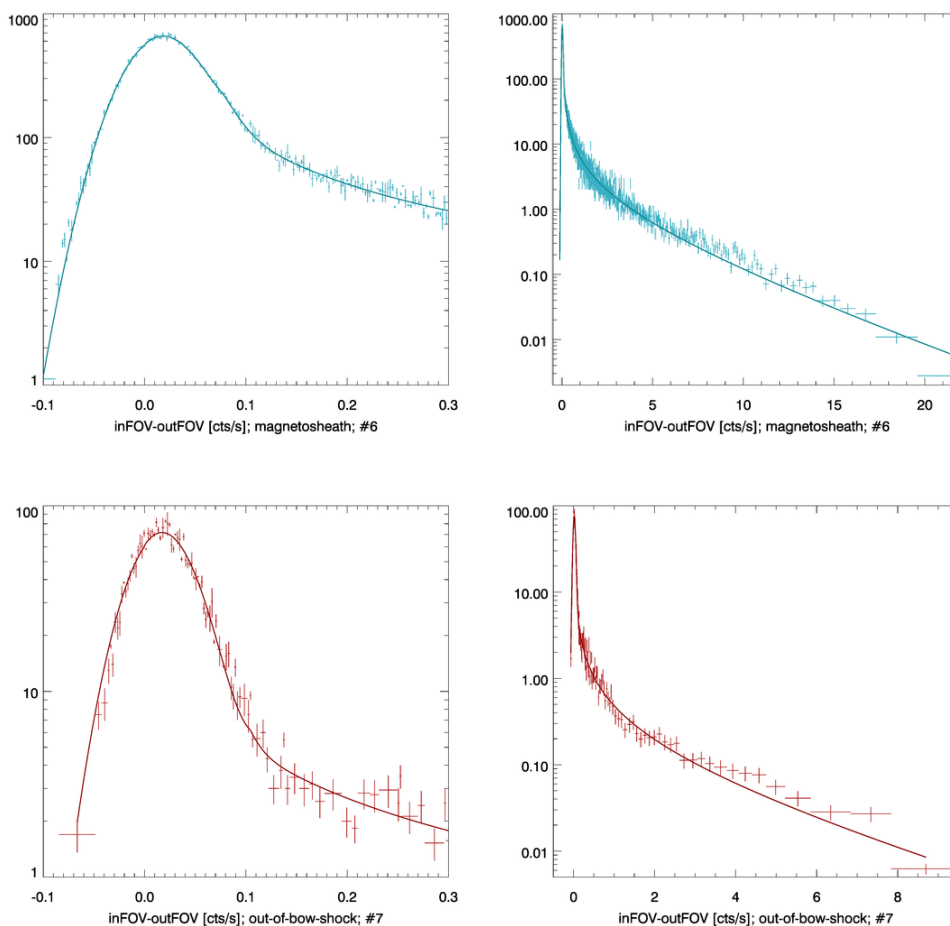


Figure 4.7: (...continued): *inFOV-outFOV* distribution for each magnetozone. Distributions in the left column are zoomed in the range [-0.1, 0.3] for a better visualization of the low-intensity component. Best fit functions described in Section 3.3.2 are overlotted. Different regions are color coded as in Figure 4.1.

To compare the different ambients, we rescale all the distributions to the same maximum value, fixed to unity (Figure 4.8). In the left column panels, we zoom to low count rates, for a better visualization of the low-intensity component. The three “main” magnetozones (#5, #6, and #7) are very similar, with the out-of-bow-shock distribution featuring a slightly lower tail. The regions #3 and #4 show a prominent enhancement of the tail. It is worth noting that the rescaling used to overplot the distributions does not allow a direct comparison of the intensity of the flaring component (which is, instead, quantified by the flaring mean rate value reported in Table 4.2). Rather, the plot shows the relevance of the flaring component with respect to the low-intensity component.. A quantitative comparison of the different magnetospheric regions both for the flaring and the low-intensity component is provided in Figure 4.9. In the left panel we plot (excluding the plasma sheet whose best fit values are not reliable, as previously mentioned) the best fit of the Gaussian peaks, while in the right panel we plot, for all the regions, the flaring mean rate (in both panels errors are at 68% c.l.). The peak value does not significantly vary in regions #5 #6 and #7 while it features a higher value in region #4. This suggests that the low-intensity component is probably not strongly variable, as far as the most external regions are concerned. Both

Figure 4.8 and Figure 4.9 show that the peak of the low-intensity component for region #4 is significantly shifted towards higher values. However in this region the contribution of the flaring component is higher and it becomes comparable to the low-intensity component and affects the peak position. It is impossible to disentangle the contamination of the tail on the peak position from a possible real shift of the low-intensity component; thus the behavior of the low-intensity component in this region is not easily interpreted.

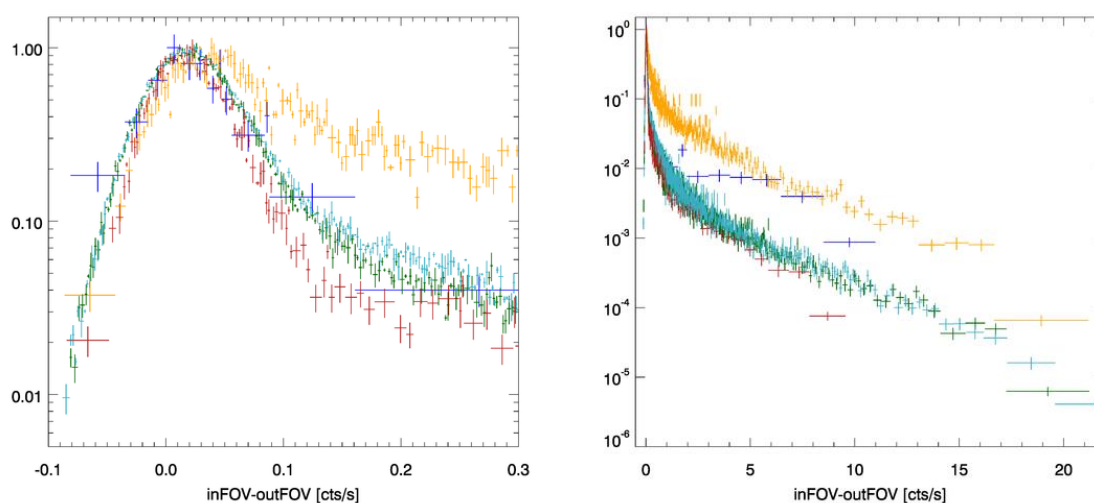


Figure 4.8: *inFOV-outFOV* distribution for each magnetozone. Distributions in the left panels are zoomed in [-0.1, 0.3] for a better visualization of the low-intensity component. Distributions are rescaled to the same maximum value. Different regions are color coded as in Figure 4.1.

The flaring component (see right panel of Figure 4.9) also shows moderate variations when regions #5, #6, and #7 are concerned, with the out-of-bow-shock region featuring the lowest values. When moving towards the innermost regions of the magnetosphere (#3 and #4) the flaring component intensity significantly enhances. It is worth noting that all the regions feature a flaring mean rate higher than 1, i.e. a factor of ten larger than the threshold we use to separate the components. This implies that there are no magnetic environments free from soft protons flares.

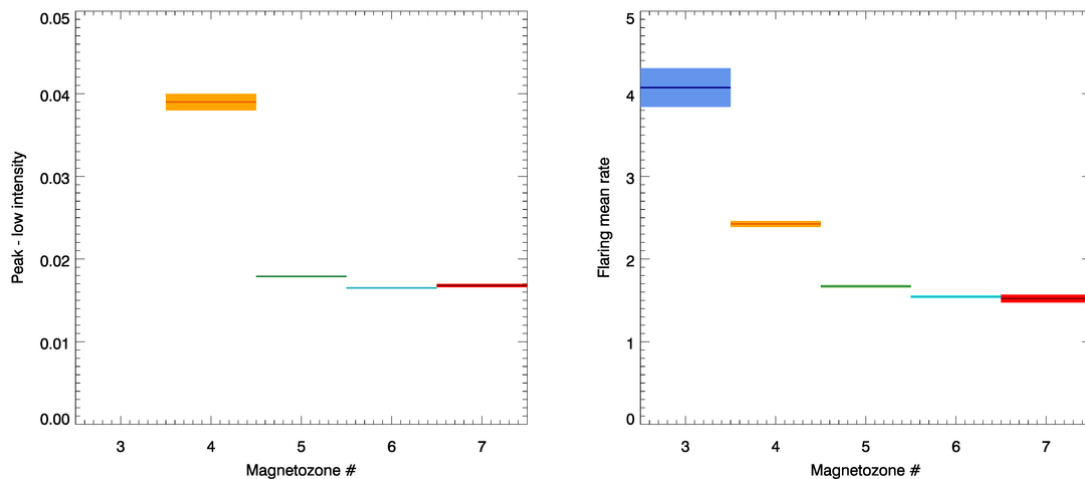


Figure 4.9: *Left panel:* Gaussian peak positions obtained fitting *inFOV-outFOV* distributions in the different magnetosphere regions with function defined in Section 3.3.2. *Right panel:* Means for high count rates (*inFOV-outFOV* > 0.1 cts/s) in the different magnetospheric regions. Different regions are color coded as in Figure 4.1.

4.4.2 Dependence on the XMM-Newton altitude

The results reported in the previous section show that variations in different magnetozones are modest, with magnetoplasma (which is located closed to the radiation belts) featuring the highest values, while the out of bow shock region records the smallest values. This suggests that the *inFOV-outFOV* flux may be related to the altitude of the satellite rather than to the particular magnetozone.

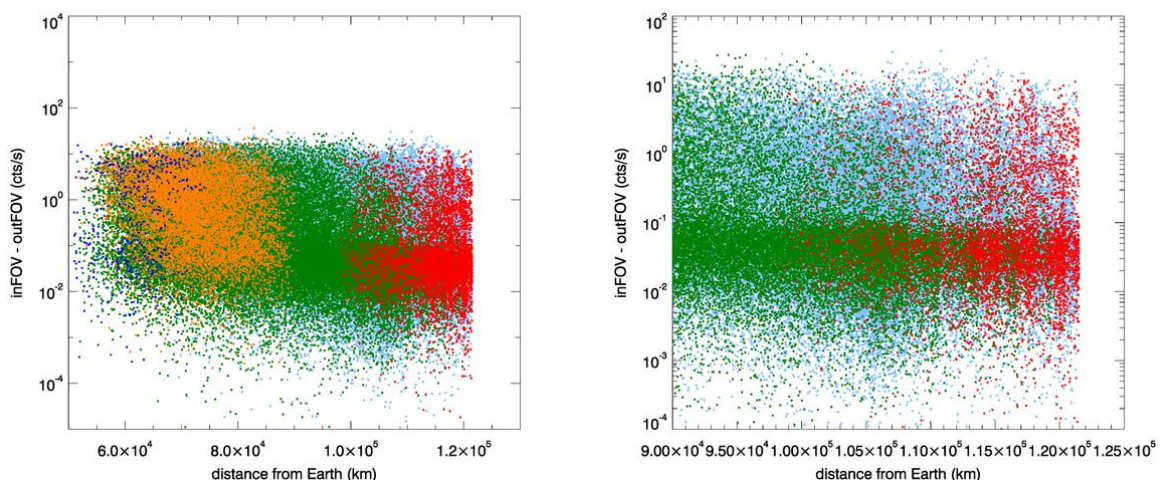


Figure 4.10: *inFOV-outFOV* rate for the whole EXTras sample as function of the XMM-Newton distance from the Earth. In the right panel we zoomed to large distances where the majority of data is located. Different regions are color coded as in Figure 4.1.

In Figure 4.10, we plot all the EXTrAs *inFOV-outFOV* rates versus the distance from Earth. In the right panel we zoom to larger distances where most of the data are taken.

Due to the high dispersion, it is not straightforward to infer any particular behavior, even if a descending trend can be observed in the left panel. Looking at the right panel it is apparent that no striking change occurs when passing from a magnetozone to another.

We inspect in detail the *inFOV-outFOV* behavior with altitude, separately for the flaring and the low-intensity component. To study the flaring component at different altitudes, we rebinned data using 2-

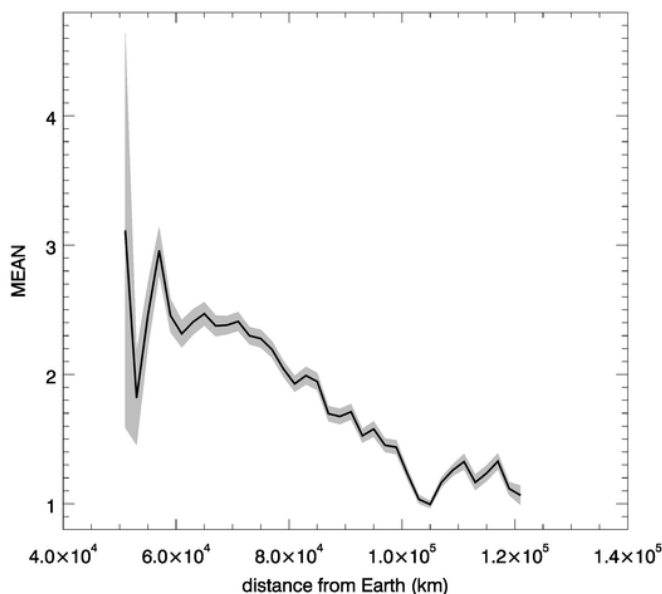


Figure 4.11: Mean for the *inFOV-outFOV* rate, for count rates > 0.1 cts/s, of the whole sample as a function of the XMM-Newton distance from the Earth.

km-wide shells. We determined in each bin the mean of the *inFOV-outFOV* rate (for count rates > 0.1 cts/sec, i.e. the flaring mean rate), irrespective of the magnetospheric environment. Figure 4.11 we plot this indicator as a function of XMM-Newton distance from the Earth. It significantly decreases with the distance: soft proton flares affect the XMM-Newton background at low altitudes more than at high altitudes, even though (as we already noted, see Figure 4.9) the flaring mean rate never drops below 1 cts/s, showing that this background component can occur in all parts of the XMM-Newton orbit.

The behavior of low-intensity component at different altitudes cannot be studied through 2-km-wide shells, since statistics is not enough to perform the fitting procedure. We divided the 50000-125000 km altitude range into 11 bins. Ranges are selected to have about 10000 *inFOV-outFOV* time bins.

In Figure 4.12 we plot the distributions (zoomed to low count rates in the left column) for all the bins, rescaled so that the maximum value is 1 to help comparison. Colors represent the different altitude shells with black points referring to the innermost shell while red points refer the most distant shell. The tail shows a clear progressive decreasing trend from the innermost to the outermost shell which reflects the result shown in Figure 4.11. On the contrary, variations of the peak positions are modest. In Figure 4.13 (left panel) we plot the smoothed distributions: the peak position slightly shifts towards high values when moving towards the Earth. However these variations are small if compared to the variations of the tail.

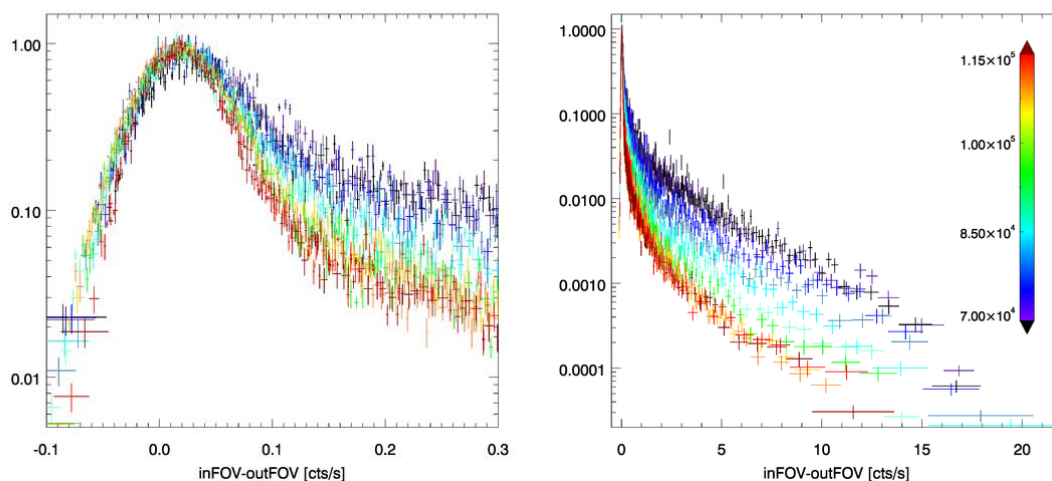


Figure 4.12: *inFOV-outFOV* distribution for different altitude shells. Distributions in the left panel are zoomed in the range [-0.1, 0.3] for a better visualization of the low-intensity component. Distributions are rescaled to the same maximum value. Different regions are color coded as in Figure 4.1.

In the right panel of Figure 4.13 we plot the modes of the smoothed distributions, except for the innermost bin where the distribution is irregular even after the smoothing procedure. The innermost bins, below 80000 km feature a significantly higher peak values, while at high altitudes values drop below 0.020. The peak values at high altitudes are spread in the [0.0165 - 0.020] range. Although this spread is apparently large, we should note that these variations are of the order of 15%, which is small if compared with variations of the tail intensity that cover almost an order of magnitude. Moreover, variations at high altitudes do not follow a systematic trend but fluctuate. As already pointed out in Section 4.4.1 the shift of the peak position in the innermost regions is not immediately interpreted. The high relevance of the tail component in these regions can affect the peak position and this contamination does not allow to draw conclusions on the behavior of the low-intensity component.

4.4.3 Dependence on the direction: Sunward and anti-Sunward

A further discriminatory factor which can, in principle, induce differences in the *inFOV-outFOV* rate is the position of XMM-Newton in the dayside or in the nightside of the magnetosphere.

Since the low-intensity component did not show strong variations with the magnetospheric environment and with the distance from Earth, we restrict the analysis to the flaring component and investigate if the front/back position affects the soft proton rate intensity. We evaluate the mean of the *inFOV-outFOV* rate (for count rates > 0.1 cts/sec) in the same 2-km-wide shells used in Figure 4.11, and separate regions Sunward and anti-Sunward. The two profiles are plotted in Figure 4.14. Both in the dayside and nightside of the magnetosphere the flaring component features a decrease with the altitude. In general data taken in the dayside have a higher value than data taken in the nightside. This suggests that regions in the backside of the magnetosphere are less contaminated by soft-proton-flares than regions in the dayside, with little influence from the magnetospheric environment.

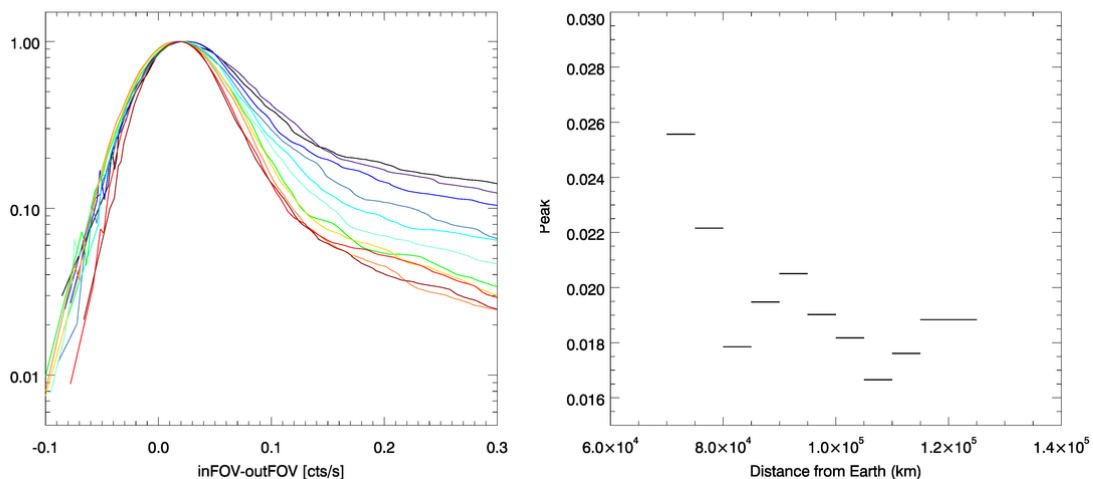


Figure 4.13: *Left panel:* $inFOV-outFOV$ smoothed distribution for different altitude shells. Distributions are rescaled to the same maximum value. Different regions are color coded as in Figure 4.1. *Right panel:* Peak position for smoothed distribution as function of the XMM-Newton distance from the Earth.

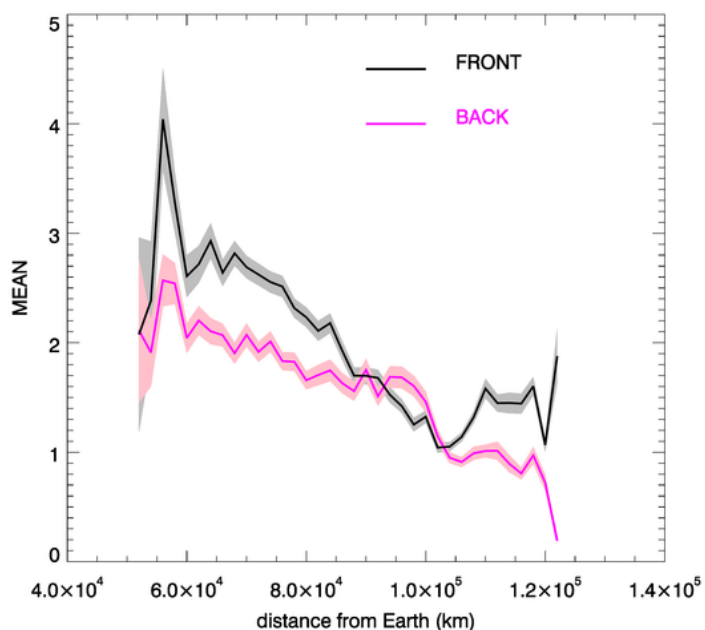


Figure 4.14: Mean for the $inFOV-outFOV$ rate (for count rates > 0.1 cts/s) as a function of distance from Earth in the dayside (black) and in the nightside (magenta) of the magnetosphere.



ATHENA Radiation Environment Models and X-Ray Background Effects Simulators	WP1 TN 1.1	Doc No: IASFMi-ATHENA-WP1 Date: 10 February 2017 Page: 54 of 78
---	-----------------------------	---

4.5 Conclusions

In this sub-WP we studied the role played by the different magnetospheric ambients on the *inFOV* excess background detected by XMM-Newton.

Our analysis shows that moving from a magnetozone to another has a moderate influence both on the low-intensity background and flaring soft proton component. On the contrary, the soft proton rate is highly related to the satellite altitude with higher rates at low altitudes. A substantial difference in the soft proton rate is found when comparing Sunward with anti-Sunward regions, the former featuring a higher background rate than the latter.

5 SPB3: THE ORIGIN OF THE SOFT PROTON COMPONENT

5.1 Introduction and data selection

The objective of this sub-WP is the comparison of the XMM flaring background component caused by soft protons with environmental estimates of the soft proton particle flux recorded by orbiting satellites designed and calibrated to measure those particles. The final goal is to estimate the concentrating power of the XMM optics.

We used as primary datasets the *inFOV-outFOV* XMM rate (see Section 3.2.2) which reflects the intensity of the soft proton component when the count rate is above 0.1 cts/s (see Section 3.3.2) and the data from the Advanced Composition Explorer (ACE) satellite in orbit around L1 [Stone et al. 2001], chosen because it has a time span of available data comparable to the one we have for XMM. We used particle data from the Low energy Magnetic Spectrometers (LEMS), LEMS120 and LEMS30, of the EPAM instrument dedicated to monitor the low energy (46 keV - 4.8 MeV) protons [Gold et al. 1998]. Of particular interest for our purposes are the low energy channels of those detectors, P1 that covers the 46-67 keV energy range and P2 that covers the 67-115 keV range for LEMS30 and P1' and P2' that refer to the channels for LEMS120 in the same energy ranges. LEMS30 points at 30° from the Sunward pointing spin axis and LEMS120 points at 120° from the spin axis, therefore looking back towards the Earth's bow shock. Because of this orientation LEMS120 is sensitive to upstream events (brief, intermittent particle flux enhancement) when magnetically connected to the Earth's bow shock. The LEMS30 detector with its different orientation is not as sensitive to upstream events [e.g., Haggerty et al. 2000, Tessein et al. 2015]. Furthermore the LEMS30 P1 channel has no data since day 327 of 2001 and P2 since day 302 of 2003 [Haggerty et al. 2006]. We will therefore base mainly our analysis on the LEMS120 P1' and P2' channels. We took the 5 minutes average calibrated Level 2 data from the ACE science center¹¹.

5.2 Comparison of the *inFOV-outFOV* MOS2 and ACE EPAM LEMS data

We show the comparison of the EPIC MOS2 *inFOV-outFOV* rate and ACE LEMS120 proton flux in the P1' and P2' channels in Figure 5.1. It is clear from the investigation of the plot that there is no striking correlation, besides a tendency for a lower envelope, meaning that given a high flux of soft protons in L1 we can expect a corresponding high level in EPIC. However at any given flux in L1 there is a wide range of intensities of soft protons detected at the position of the XMM orbit, pointing to local (within the magnetosphere) acceleration sites for this particle component. Much of the structure seen below $2 \times 10^3 / (\text{cm}^2 \text{ s sr MeV})$ in the P1' channel is due to background [Haggerty et al. 2006]. The P2' channel is not affected by background problems and it provides the same basic picture. We have not applied a delay time allowing for protons flight time from L1 to Earth, also because it is not always clear the direction of travel (e.g. in the case of upstream events). We experimented applying delay times from 400s (the free streaming travel time from L1 to Earth for a 67 keV proton) up to 1hr and the qualitative picture does not change.

If we divide our data when considering time intervals not affected by SEP events and time intervals during SEP events (see Figure 5.2) we can see that as expected the bulk of high proton fluxes in L1 corresponds to SEP events, however this does not correspond to a better correlation in the EPIC data. It should be noted that most of the time during SEP events EPIC is not observing to prevent radiation damage: during 92 SEP events lasting totally for 39.08 Ms occurring in the time span of our XMM data EPIC has been observing for 7.7 Ms corresponding to 20% of the time.

¹¹ http://www.srl.caltech.edu/ACE/ASC/level2/lvl2DATA_EPAM.html

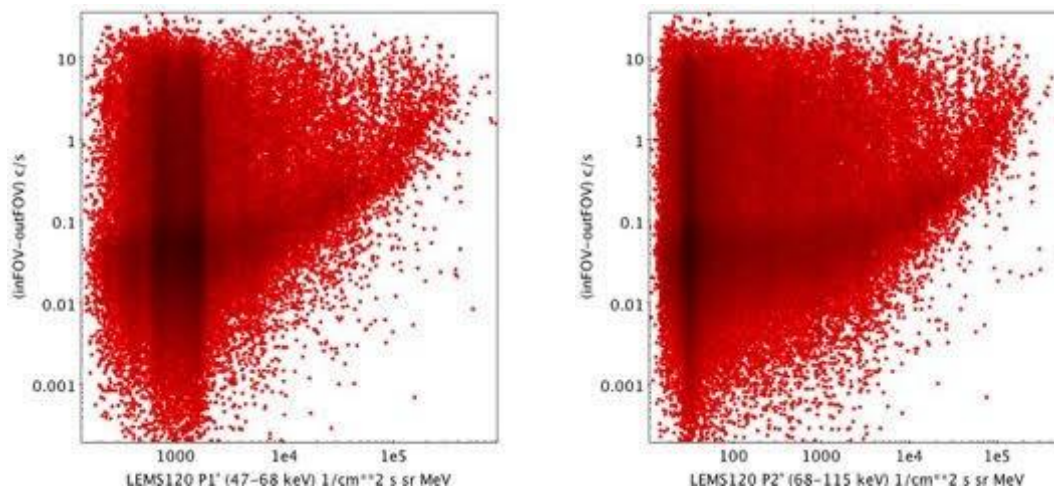


Figure 5.1: *Left panel:* Comparison of XMM (*inFOV-outFOV*) rates and ACE LEMS120 proton flux in the P1' channel (46-67 keV). *Right panel:* Same as the left panel but for the P2' channel (67-115 keV).

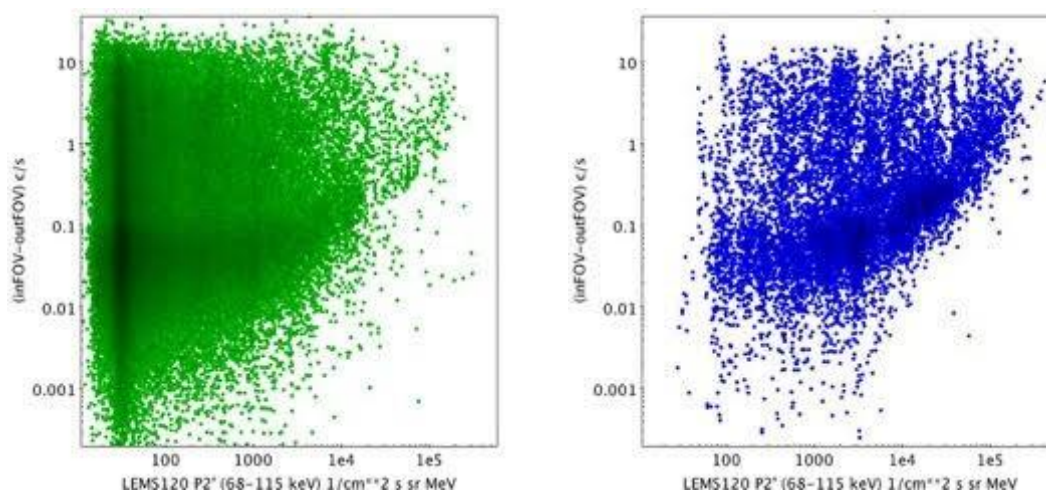


Figure 5.2: *Left panel:* Comparison of XMM (*inFOV-outFOV*) rates and ACE LEMS120 proton flux in the P2' channel (67-115 keV) during periods not affected by SEP events. *Right panel:* Same as the left panel but for periods during SEP events.

5.3 The *inFOV-outFOV* MOS2 and ACE EPAM LEMS data during SEPS

Motivated by the non negligible amount of EPIC data obtained during SEP events and by the working hypothesis that there might be a connection between measures at L1 and on XMM-Newton during SEPs, we investigated in detail the 92 SEP events occurring during the time span of our XMM data. We show in detail some SEP events during which the largest amount of EPIC MOS2 data are available.

The first case study shown in Figure 5.3 refers to the SEP event occurring in the time interval 19-28 October 2001 where the amount of EPIC MOS2 data available are 387.5 ks. The plot of the comparison between EPIC MOS2 *inFOV-outFOV* rate and ACE LEMS120 proton flux in the P2' channel shown in

the left panel of Figure 5.3 shows the same qualitative trend of the one collecting all data during SEPs shown in the right panel of Figure 5.2. Investigating in detail the light curves we highlighted different portions of them by different colors. If the part of the light curve painted in red shows a correlation, the one in green shows a small correlation in the high MOS count rate part, whereas the one depicted in blue shows no correlation marking the “finger”-like structure well represented in the general plot of the right panel of Figure 5.2.

Another example is shown in Figure 5.4 and it refers to the SEP event occurring during 17-30 November 2001. Also in this case similar ACE proton fluxes in L1 corresponds to a wide range of *inFOV-outFOV* rates.

This general behavior points to the complexity of the problem: clearly the flux of protons in the range of few tens of keV is modulated by many factors within the magnetosphere and it cannot be simply related to the behavior in L1 measured by ACE.

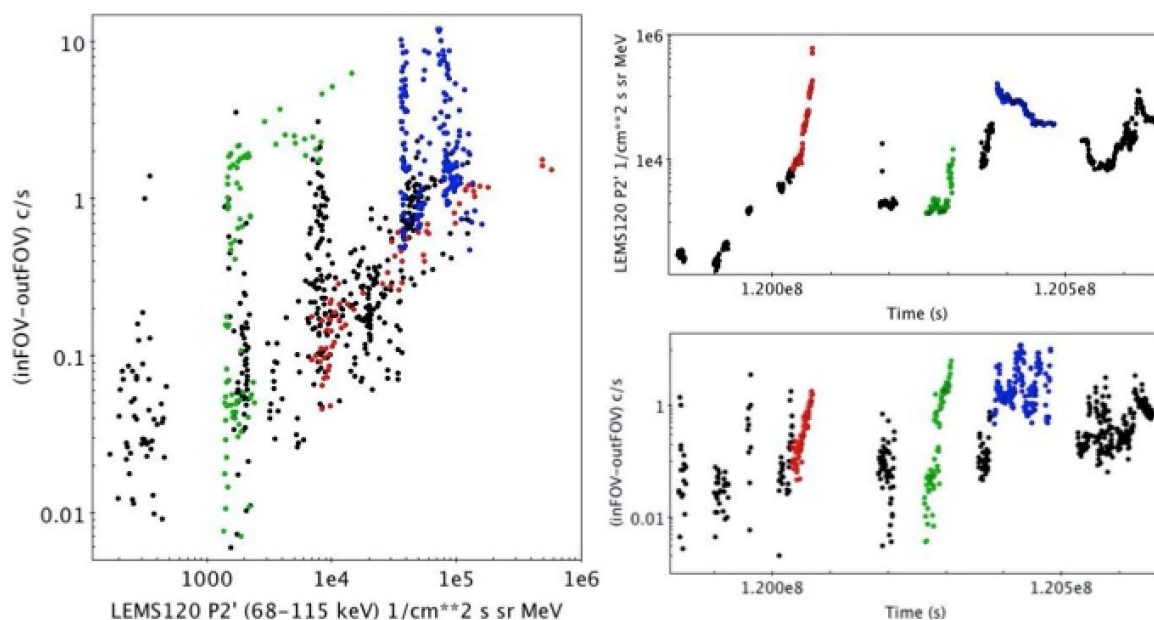


Figure 5.3: EPIC MOS2 and ACE LEMS120 P2' data taken during the SEP event of 19-28 October 2001. *Left panel:* Comparison of XMM (*inFOV-outFOV*) rates and ACE LEMS120 proton flux in the P2' channel (67-115 keV). *Right upper panel:* LEMS120 P2' light curve. *Right bottom panel:* EPIC MOS2 (*inFOV-outFOV*) light curve. Different parts of the light curves are depicted in different colors: red the portion showing a good correlation, green showing only a partial correlation, blue showing no correlation.

In order to possibly disentangle the complication due to the propagation of protons in the magnetosphere we investigated the behavior of the two dataset when selecting time interval when a SEP event was ongoing and XMM was out of the bow shock. We found 534.5 ks of data satisfying the above conditions and spanning 13 SEP events in the period from July 2000 to July 2005. The results are shown in Figure 5.5 with the same scheme as in the previous figures: despite the attempt of avoiding the complications due to the magnetosphere no clear trend emerged. This is an indication that the orientation of the satellite with respect to the local magnetic field play possibly an important role which is one of the key lessons to learn from magnetospheric physics.

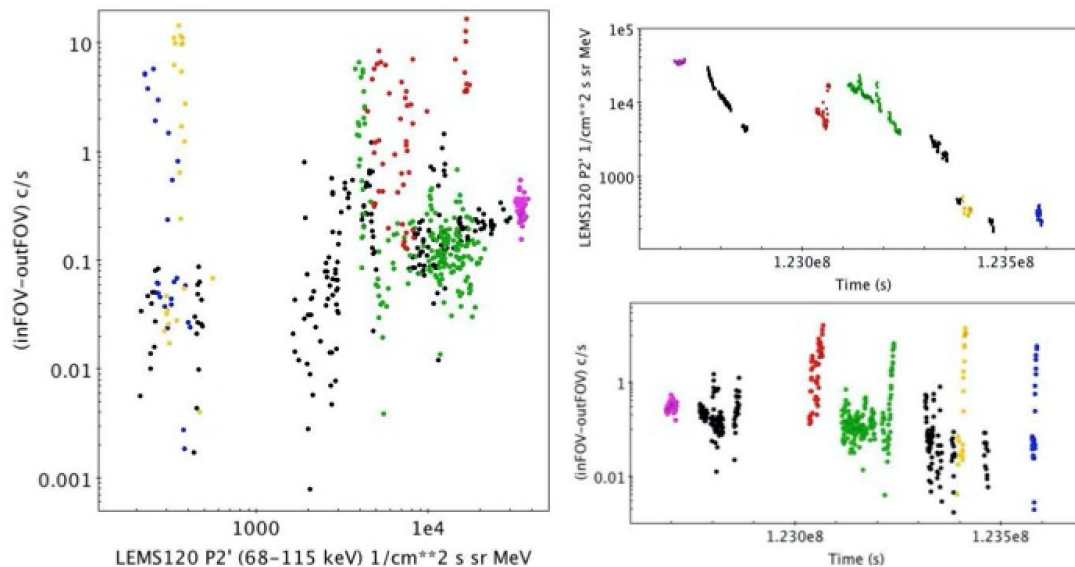


Figure 5.4: Same as Figure 5.3 but for the EPIC MOS2 and ACE LEMS120 P2' data taken during the SEP event of 17-30 November 2001.

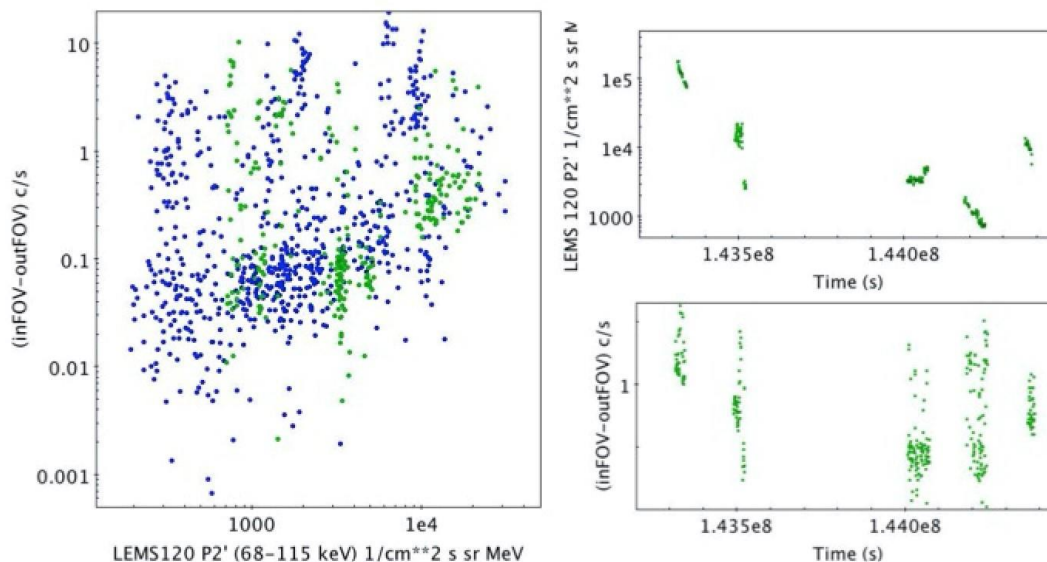


Figure 5.5: Same as Figure 5.3 but for the EPIC MOS2 and ACE LEMS120 P2' data taken in time intervals affected by SEP events when XMM was outside of the bow shock. Highlighted in green and shown in the light curves are the data taken during the SEP period of 16-30 July 2002 for 165 ks.

5.4 Comparison of the *inFOV-outFOV* MOS2 and ERM data

We also compared the Epic Radiation Monitor (ERM) and *inFOV-outFOV* MOS2 data with the selection discussed in Section 8.3. The resulting plot (see Figure 5.6) is strikingly different from the one presented

in Section 8.4 showing a clear lack of correlation, with a Spearman's ρ of -0.07 and Kendall's τ of 0.048. This reinforces with the exquisite data statistics of our project the fact that the focused soft proton component has energies below the one probed by the ERM as early recognized in the mission [e.g., Kendziorra et al. 2000].

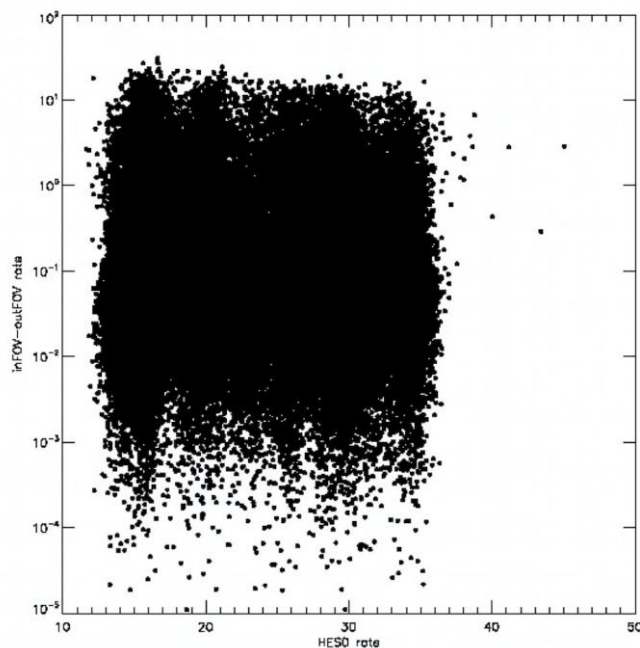


Figure 5.6: Comparison between ERM HESO count rates and the corresponding *inFOV- outFOV* count rate.

5.5 Conclusions

There is no clear correlation between the soft proton flux measured by ACE in L1 and the XMM *inFOV-outFOV* count rate. Therefore the datasets investigated in this analysis are not sufficient to reach our final goal of measuring the concentrating power of XMM optics.

Strong conclusions cannot be reached, other than an indication of the complexity of the problem and the various factors affecting the flux of soft protons entering the XMM telescopes. There are a large variety of acceleration sites for soft protons and their flux is possibly orientation dependent. A measurement of the soft proton flux needs to be performed in a location as close as possible to that of XMM at that specific time: datasets of satellite within the magnetosphere such as Cluster [Escoubet et al 1997] may prove to be valuable for this analysis. Moreover, information on EPIC observing direction should be included when executing such a comparison.

6 SPRD: RADIATION DAMAGE BY SOFT PROTONS

6.1 Introduction

The aim of SPRD sub-WP is to study radiation damage caused by focused low-energy (few tens up to few hundreds of keV) particles on detectors that have already flown in space. As low energy protons do not reach the low-Earth orbit where most X-ray satellites were launched in the past, we could base our analysis only on the experience of Chandra and XMM-Newton, which both suffered some level of radiation damage due to particles in this energy range.

6.2 Radiation Damage in Chandra CCDs

The Chandra X-ray Observatory was launched on July 23rd 1999 on an initial operational orbit with 10000 km perigee altitude, 140000 km apogee altitude and an inclination of 28.5°. In this highly elliptical orbit, Chandra transits in the radiation belts at closest approach to Earth. One of its two focal plane instruments, the Advanced CCD Imaging Spectrometer (ACIS), is composed of frame-transfer charge-coupled devices (CCDs), some of which are front-illuminated (FI) and other back-illuminated (BI).

Soon after the first observations, the CCD focal plane was moved out of the telescope focus for calibration: analysis of data of the calibration source showed that all the FI CCD chips had suffered some damage (Figure 6.1) causing a significant increase in the Charge Transfer Inefficiency (CTI), which triggered intensive investigation on the type of damage and the reason which could have caused it [Prigozhin et al. 2000].

CTI is caused by defects in the silicon lattice that can be created by the interaction with charged particles. These defects, or “traps”, capture charges during their transfer to the read-out electronics, and release them at later times. Its effects on the detector performance are: position-dependent changes in the energy scale, loss of spectral resolution and loss of quantum efficiency. In the left panel of Figure 6.1 [from Prigozhin et al. 2000], we show the CTI effect on energy scale and energy resolution, by plotting the pulseheight of an X-ray event as a function of row number when the CCD is illuminated with the calibration source. Three emission lines (Al K, Ti K and Mn K_α at 1.5, 4.5 and 5.9 keV, respectively) can be identified as areas with high density of points. The amplitude of the pulseheight of each line decreases at high row numbers because of charge packets losing charges during the transfer, and the width of the line increases at high row numbers, showing a degradation of the energy resolution. Prior to the launch, the lines in Figure 6.1 were flat with a fixed width across the whole device, as FI chips had essentially no CTI [Grant et al. 2012].

Originally, high energy protons were considered the biggest threat to the detectors, because of their penetrating and damaging properties, and intensive studies were performed prior to Chandra launch by irradiating ACIS-like CCDs with 40 MeV and 10 MeV protons. However, the type of damage suffered by ACIS detectors on flight was different than the results of the laboratory test: flight chips showed a much lower intensity of the dark current and a different dependence of CTI on temperature. Moreover, flight chips did not show indication of damage in the frame store section of the detector, which is protected by a layer of gold-plated aluminium, and the damage was found only in FI chips, not in the two BI chips. Calculations showed that to reach the transfer channels in the FI devices and to be blocked by the 40 microns substrate of BI chips, charged particles should be in the energy range 50 keV – 2 MeV [Prigozhin et al. 2000].

The Chandra team conducted experiments by irradiating an ACIS-like CCD with ~100 keV protons, with a total dose of $3.6 \cdot 10^7$ protons cm⁻². During the experiment, the dark current stayed very low as in the flight devices, two order of magnitudes below the results of irradiation tests with 40 MeV protons. Moreover, the temperature dependence of the CTI was qualitatively similar for the flight chip S2 and for the ACIS-like CCD (w459c1, see right panel of Figure 6.1; Prigozhin et al. 2000). It thus became clear

that the significant damage suffered by ACIS FI CCD was caused by a high flux of soft protons. As these particles are focused by the X-ray optics and their density is maximal along the orbit in the radiation belts, since mid September 1999 ACIS has been protected during radiation belt passages, by moving the detector out of the telescope focus. The same procedure takes place during periods of enhanced particle flux, triggered either by the on board radiation monitor or by ground operations monitoring of various space weather probes [see Grant et al 2012 for details]. Moreover, the Chandra team provided a large effort to correct the effects of CTI on Chandra analysis [Grant et al. 2003, 2005, 2012]. The detector performance in terms of energy scale, energy resolution and quantum efficiency have been thus continuously monitored since 1999. The subsequent damage is not identical to the initial damage, showing that part of the total CTI is due to high energy unfocused particles hitting the detectors. However, the performance of the FI CCD degraded more than those of the BI CCDs, which implies that soft protons can reach the detectors also during scientific observations. The degradation of the detector performances is consistent with the effect of CTI and other processes not related to interactions with charged particles (i.e. contamination of the focal plane). Thus the only known radiation damages experienced by ACIS and caused by charged particles and soft protons are associated to CTI.

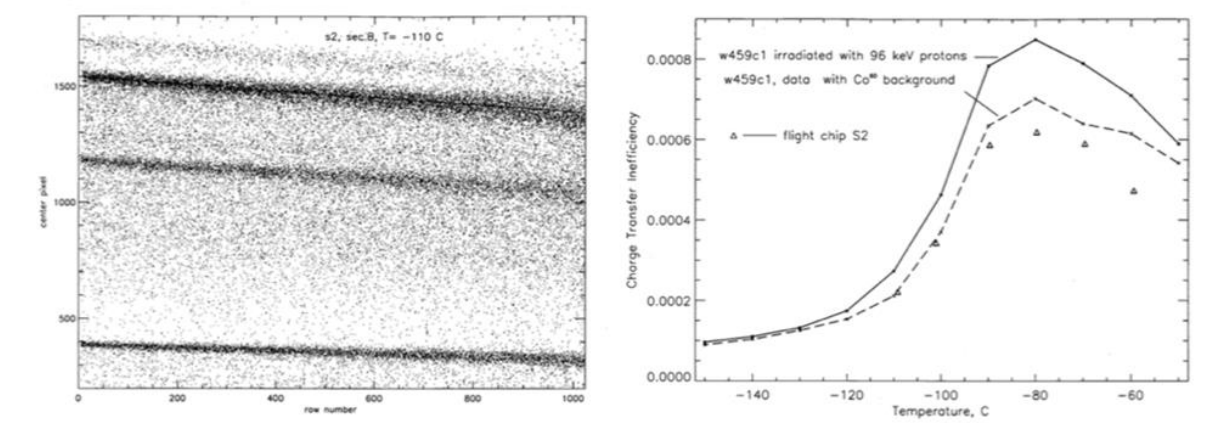


Figure 6.1: *Left:* Pulseheight of the center pixel as a function of row number for the Chandra ACIS-S2 detector with in flight calibration source, showing indication of loss of energy resolution due to CTI [from Prigozhin et al 2000]. *Right:* Temperature dependence of CTI for the Chandra ACIS-S2 detector (triangles), compared with ground tests on spare device w459c1, irradiated in the laboratory with ~100 keV protons. The solid line reproduces the output of ground tests using only protons, while the dashed line shows the results of an experiment with protons and a Co⁶⁰ X-ray source to mimic the X-ray background experienced on flight [see Prigozhin et al 2000, for details].

6.3 Radiation Damage in XMM-Newton detectors

The ESA X-ray satellite XMM-Newton was launched into a highly-eccentric orbit in December 1999, a few months after the launch of Chandra and the discovery of radiation damage by soft protons on its FI CCDs. The MOS cameras use front-illuminated CCDs, while the pn CCDs are back-illuminated. EPIC cameras are kept closed when the satellite goes through the radiation belts, at an altitude below 45000 km. This shrewdness prevented the FI MOS-CCDs to suffer a similar damage as experienced by the Chandra chips in the first months (Section 6.2). However, soft protons reach CCDs also in other parts of the orbit and contribute to the overall damage of the detectors. The instruments teams of the EPIC cameras have monitored continuously the performance of their detectors in terms of energy scale and resolution. As an example, we show in Figure 6.2 the monitoring of the CTI of the central CCD of the MOS2 detector in the first 3.5 years of the mission [Altieri et al.

2004]. The CTI shows an increasing trend with a few sudden jumps associated to powerful coronal mass ejections (see Section 9.2). In November 2003 (revolution 553), the EPIC team reduced the operational temperature of the CCD from -100 degrees to -120 degrees: with this procedure the CTI was reduced by a factor of three for most CCD chips and degradation rate was limited to acceptable levels ($dCTI/dt \sim 2 \cdot 10^{-6} \text{ yr}^{-1}$ at 6 keV, Altieri et al 2004).

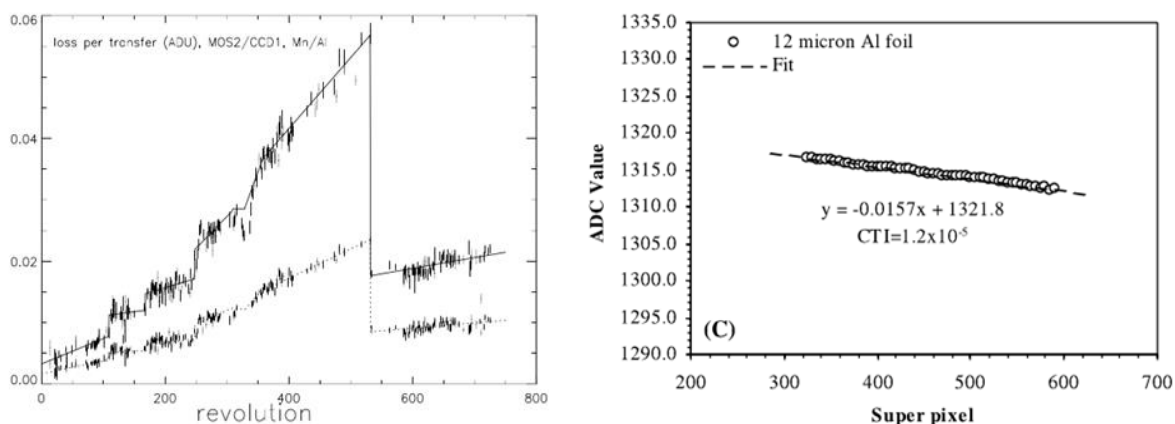


Figure 6.2: *Left:* Evolution of the CTI for the MOS2 central CCD, expressed as ADU signal losses per transfer at the two energies of the calibration source Al K α (1.49 keV) and Mn K α (5.896 keV). From Altieri et al. [2004]. *Right:* Results of ground tests on flight-type MOS CCD irradiated with $5 \cdot 10^6$ protons $\text{s}^{-1} \text{ cm}^{-2}$ with energy 170 keV, showing indications of CTI [Ambrosi et al 2003].

While part of the CTI degradation experienced by MOS is due to high-energy unfocused particles (see Section 9.2) also soft protons can contribute to it. Indeed, Abbey et al. [2001] conducted experimental tests and Monte-Carlo simulations to quantify the CTI induced by low energy particles on MOS detectors [see also Ambrosi et al 2003]. They irradiated MOS-like CCDs with protons at energies 70, 170 and 330 keV with doses in the range 10^7 - $2.3 \cdot 10^6$ protons cm^{-2} and found a significant increase of the CTI when using particles with energy 170 and 330 keV (see Figure 6.2). They used these experimental data to implement a simulation code to predict the effect of a flux of protons, with given spectra on the CTI of MOS chips. They assumed the spectral shape and proton flux ($0.2 \text{ protons cm}^{-2} \text{ s}^{-1}$) measured by Kendziorra et al. [2000] from observations during SP flares with the pn detector in low-gain and found their prediction for the CTI ($7.3 \cdot 10^{-6}$ - $1.5 \cdot 10^{-5}$) to be close to the values measured on flight for the MOS CCDs ($1.3 \cdot 10^{-5}$ - $1.7 \cdot 10^{-5}$).

Contrary to MOS FI CCDs, BI pn chips are not damaged by low-energy particles that lose all their energy before reaching the transfer channels. Indeed, Kendziorra et al. [2000] irradiated pn-like CCD with 100 keV protons and a total dose of 10^9 protons cm^{-2} , finding no impact on the detector performance.

As for Chandra, the radiation damage of the EPIC detectors due to charged particles is consistent with CTI, both by low-energy focused particles (especially for MOS) and high-energy penetrating particles (see UPRD sub-WP, Section 9).

6.4 Conclusions

The continuous monitoring of the performance of the detectors in both Chandra and XMM-Newton have shown that they suffered radiation damage, part of which is due to low-energy protons focused by the X-ray mirrors. In both cases, the change in the energy scale, the loss of energy resolution and quantum



ATHENA Radiation Environment Models and X-Ray Background Effects Simulators	WP1 TN 1.1	Doc No: IASFMi-ATHENA-WP1 Date: 10 February 2017 Page: 63 of 78
---	-----------------------------	---

efficiency are consistent with CTI caused by both low-energy protons and high energy penetrating particles (see Section 9), with the addition of other effects which are unrelated to the charged particles (micrometeorites, focal plane contamination...).

We do not have evidence of other effects due to charged particles on X-ray CCDs besides CTI, which should not be an issue for Athena detectors as they do not transfer charges.

7 UPB1: UNFOCUSED PARTICLE BACKGROUND FROM VARIOUS MISSIONS

7.1 Introduction

We collected and compared unfocused non X-ray background (UNXB) spectra from four X-ray satellites: XMM-Newton, Chandra, Swift and Suzaku. The four missions selected for this analysis allow comparisons between the detector design and the orbit of the mission. While Swift and Suzaku have low orbits (500-600 km), Chandra and XMM-Newton orbits are much higher (60000-100000 Km). The XMM-Newton and Swift missions both use the same type of MOS CCD and therefore allow the very effect of the orbit to be studied. The Swift and Suzaku missions use different types of detectors and allow the effects of the detector design to be investigated in a similar orbit.

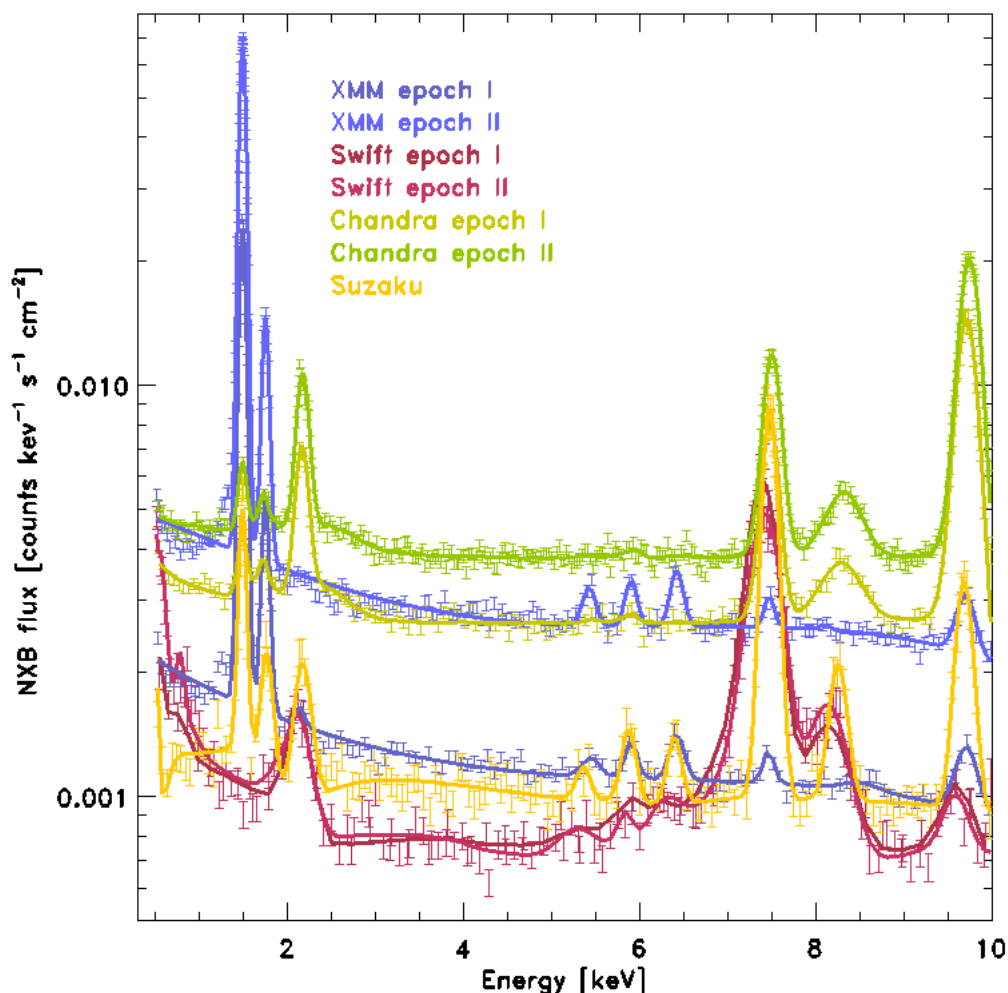


Figure 7.1: NXB spectra, normalized per unit of area of the detector. Continuous lines show the best-fit models.



Detailed studies of the UNXB properties of the single mission have been published in Kuntz and Snowden [2008] for the XMM-Newton, Tawa et al. [2008] for Suzaku, Moretti et al. [2009] for Swift XRT. The origin of the instrument background has been investigated in the last decade by different authors [Murakami et al. 2006, Hall et al. 2008, Campana et al. 2013].

Starting from the cosmic rays observed spectra and using Monte Carlo simulations to reproduce the interactions with the detectors, they succeeded in reproducing the observed NXB of different telescopes both in high and low orbits.

7.2 Dataset

Different strategies have been applied to separate the instrumental component of the different missions from the Cosmic X-ray Background (CXRb). For Suzaku the dark Earth observations provide the best dataset. The XMM-Newton spectra are extracted from CLOSED filter observations. For Chandra ACIS-I UNXB is routinely monitored operating the detector in a stowed position moving ACIS further away from the external calibration source than in the HRC-I position. Finally, for the Swift-XRT the NXB spectrum is provided by the data collected in the small regions of the detector that are not exposed to the sky. While XMM-Newton, Chandra and Suzaku datasets are relatively short exposures of the whole detector, the Swift-XRT data-set is represented by very long exposure of a small part of the CCD (Table 7.1).

In all the cases the detectors operate in the standard science mode so that all the usual filters and corrections can be applied. The grade/pattern selection filter procedure is expected to produce only negligible differences among different detectors. This is because the event grade/pattern definitions are fundamentally the same: in fact the ASCA grades 0,2,3,4,6 which are the good X-ray events for Suzaku and Chandra precisely correspond to the 0-12 grades adopted by XMM-Newton and Swift.

Table 7.1: Observation table. For each satellite the roman number indicates the different epochs. In the last column, the detector area used for the present analysis is reported

	date	expo [ks]	area [cm ²]
XMM I	Dec99 – May05	360.4	28.51
XMM II	May05 – Nov10	254.9	28.51
Cha I	Jan02 – Dec05	235.0	24.15
Cha II	Jan06 – Dec09	367.0	24.15
Swi I	Jul08 – Dec08	6290.0	0.1604
Swi II	Jan11 – Dec11	15747.8	0.1604
Suz I	Jan09 – Dic09	520.8	5.164

7.3 Data comparison

As expected the high-orbit telescopes suffer a higher level of particle flux which produce a significantly higher NXB. Despite the completely different structures, Swift and Suzaku X-ray telescopes register very similar NXB continuum level with a difference of ~15% (Table 7.2). The most striking aspect of Figure 7.1 is that, while the level of the low orbit NXB is constant during the mission, Chandra and XMM-Newton present huge variations, of 1.5 and 2.5 factor respectively.

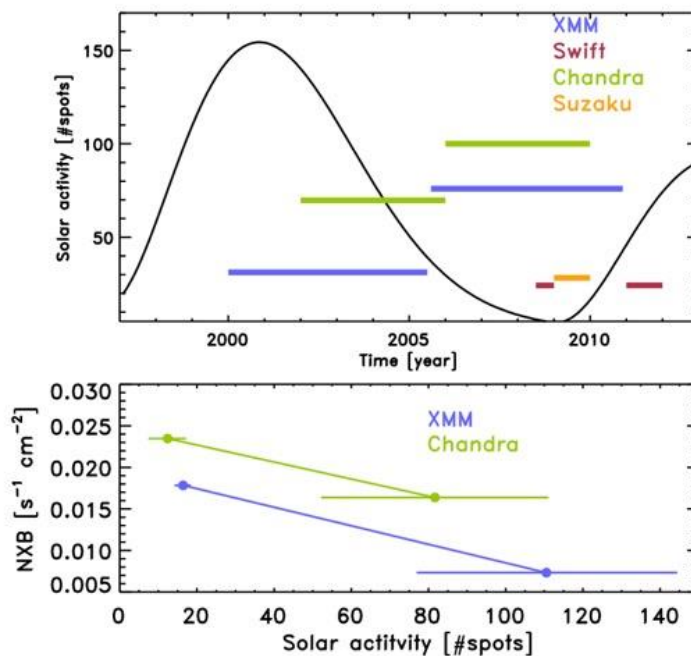


Figure 7.2: NXB fluxes and Solar activity.

We investigated the effect of the Solar activity on the NXB level. As a proxy of the solar activity we adopted the sunspot smoothed number [Hathaway et al. 2010]. In the upper panel of Figure 7.2 we plot the total flux (soft + hard) of the seven observations arbitrarily renormalized. As expected we found that the NXB level anti-correlates with solar activity (lower panel Figure 7.2). Accounting for the Solar cycle, the XMM NXB is ~40% lower than Chandra, while it is 1.3-3 times higher than the low orbit telescopes (Table 7.2).

7.4 Spectral fit

In order to assess the relative contribution of fluorescence lines and continuum we modeled the seven spectra by means of a set of empirical analytical models. We found that all the seven spectra we considered in the 0.5-10 keV energy band can be well modeled by the sum of two power-laws, corrected by a cubic spline plus a variable number of emission lines.

The X-ray fluorescence lines in all the seven datasets account for 20-30% of the total NXB (Table 7.2). The maximum is registered by the Swift XRT where the Ni K α line overwhelms the continuum with an equivalent width of ~3 keV.



Table 7.2: Mean particle flux in each observation in the 0.5-2.0 and 2.0-10. keV bands. In the last column the fraction due to fluorescence lines is also reported.

	soft [$\text{s}^{-1} \text{cm}^{-2}$]	hard [$\text{s}^{-1} \text{cm}^{-2}$]	line/total
XMM I	$2.64\text{e-}03 \pm 1.6\text{e-}05$	$4.72\text{e-}03 \pm 2.1\text{e-}05$	0.20
XMM II	$6.83\text{e-}03 \pm 3.1\text{e-}05$	$1.11\text{e-}02 \pm 3.9\text{e-}05$	0.23
Cha I	$2.56\text{e-}03 \pm 2.1\text{e-}05$	$1.39\text{e-}02 \pm 4.9\text{e-}05$	0.21
Cha II	$3.62\text{e-}03 \pm 2.0\text{e-}05$	$1.99\text{e-}02 \pm 4.7\text{e-}05$	0.20
Swi I	$9.90\text{e-}04 \pm 3.1\text{e-}05$	$4.80\text{e-}03 \pm 6.9\text{e-}05$	0.27
Swi II	$1.17\text{e-}03 \pm 2.2\text{e-}05$	$4.58\text{e-}03 \pm 4.3\text{e-}05$	0.33
Suz I	$1.25\text{e-}03 \pm 2.2\text{e-}05$	$5.48\text{e-}03 \pm 4.5\text{e-}05$	0.32

7.5 Summary

Our comparative analysis of the instrumental background measured by different X-ray satellites may be summarized as follows:

- We detect a substantial dependence on the orbit: experiments in LEO have lower levels of background than those in HEO, conversely only moderate differences between different experiments placed in the same orbit are found.
- Experiments on high Earth orbits show evidence of background modulation with the solar cycle.
- Experiments on low Earth orbits show no evidence of background modulation with the solar cycle.
- The fraction of line to total emission for the background is about 20% for HEO missions and 30% for LEO missions.

8 UPB2: THE ORIGIN OF THE UNFOCUSED PARTICLE BACKGROUND

8.1 Introduction e data selection

The objective of the UPB2 sub-WP on the unfocused particle background is to identify the primary mechanism responsible for the instrumental background observed in EPIC MOS2 data.

We define here as instrumental background the unfocused particle background, i.e. the one recorded when the EPIC MOS2 instrument is not exposed directly to the view of the sky. For this purpose we analyzed data taken when the filter wheel is in the closed position and the unexposed corners data taken during normal observations taken in Full Frame (*outFOV*, Section 2.3.2).

We also analyzed the data of the EPIC Radiation Monitor (ERM), which consists of two detectors, the low energy proton and electron unit (LE) and the high energy particle unit (HE). All the units are based on Silicon diodes, which record the energy loss in the material. In particular we made use of the counts detected in single event mode (HES0) in the HE, which are sensitive to protons in the 8-40 MeV range. For a description of the ERM see <http://www.cosmos.esa.int/web/xmm-newton/radmon-details>.

An example of a ERM HES0 light curve through an XMM orbit is shown in Figure 8.1 together with the light curves of the EPIC MOS 2 count rates within the FOV and in the unexposed corners (*outFOV*). The main features are shown: the high ERM rates at the beginning and at the end of the orbit correspond to the belt passages where the EPIC instrument is not taking data. The ERM count rate for the rest of the revolution reflect the intensity of the Galactic Cosmic Rays (GCRs). The light curve of the *outFOV* data show also no variation with time, whereas the background rate inside the field of view (*inFOV*) is much more variable and flares are seen typically not present in the ERM data. The latter is the background component associated to tens of keV protons concentrated by the mirrors and well outside the energy band probed by the ERM.

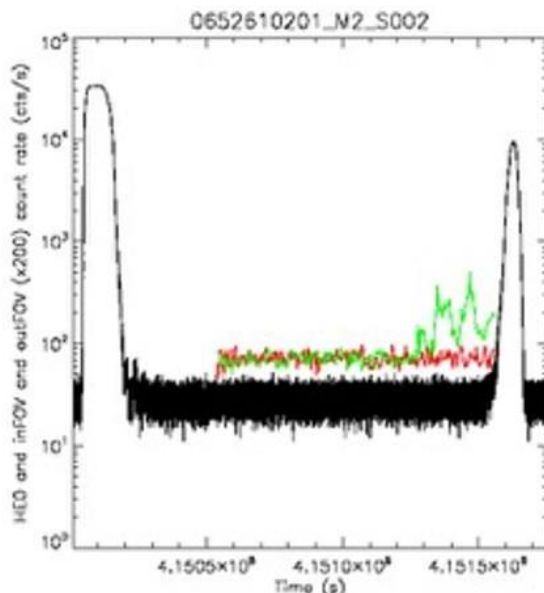


Figure 8.1: ERM HES0 light curve of the rev 2054 (black) together with the EPIC MOS2 light curves in the FOV (*inFOV*, green) and outside the FOV (*outFOV*, red) for the observation with OBSID 0652610201 (lasting for almost the entire EPIC observation window during that orbit), rescaled for display purposes.

8.2 Dependence on solar cycle

The key temporal variation imposed on the ERM and EPIC data for what concerns the unfocused instrumental background is the solar cycle because it modulates the Galactic Cosmic Rays (GCR). The GCR flux anticorrelates with the solar cycle. This for example has been found in the behaviour of the Chandra background rate as a function of time (see Figure 8.2; taken from C. Grant website¹²) which as expected is anti-correlated with solar activity, as is the GCR flux. The inference is that the Chandra background is dominated by the GCR rate [e.g., Smith et al. 2010].

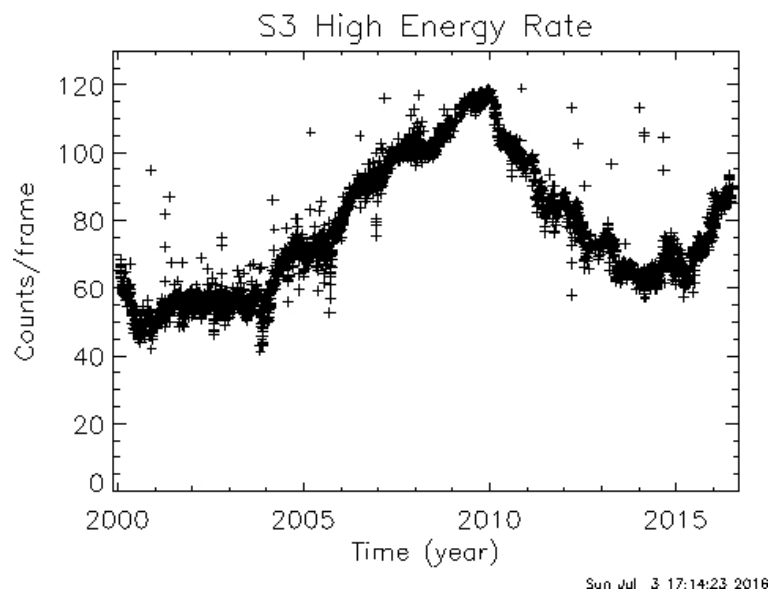


Figure 8.2: Chandra high energy (12-15 keV) count rate for the ACIS-S3 CCD as a function of year.

A useful and easy proxy for the solar activity is the number of sun spots and this is plotted aside the median in each XMM orbit of the ERM HES0 count rate (see Figure 8.3). This plots highlights the fact that the median count rate is effective in removing features due to passage in the belts but not periods of enhanced count rates which are due to Solar Energetic Particle (SEP) events. These two types of time intervals, passage in the belts and SEPs, are periods where the proton flux in the 8-40 MeV range is not just due to GCR.

¹² <http://space.mit.edu/~cgrant/cti/cti120/bkg.pdf>

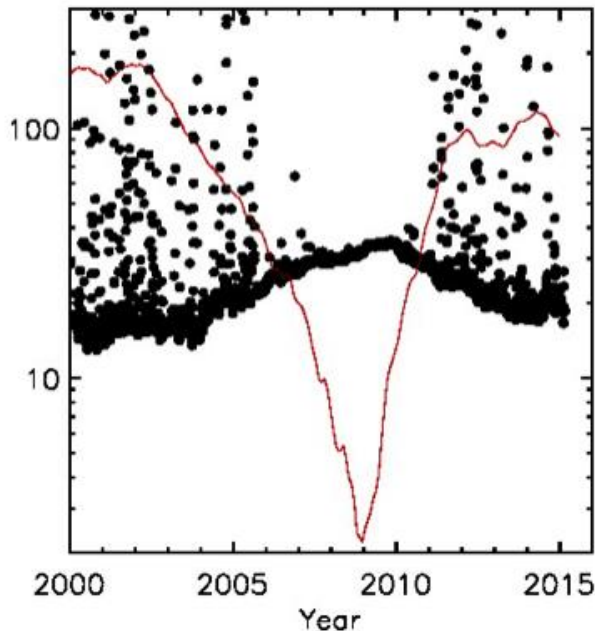


Figure 8.3: The median count rate of the ERM HES0 is shown as a function of time (black dots). The number of sun spots, taken as a proxy of solar activity, is overplotted in red, in arbitrary units. There is a clear general trend of anticorrelation as expected given that most of the time the 8-20 MeV proton flux reflects just the GCR flux. However this is no longer true when SEPs are present which can last for many XMM orbits. It is also clear from the plot that SEPs are present only during high solar activity.

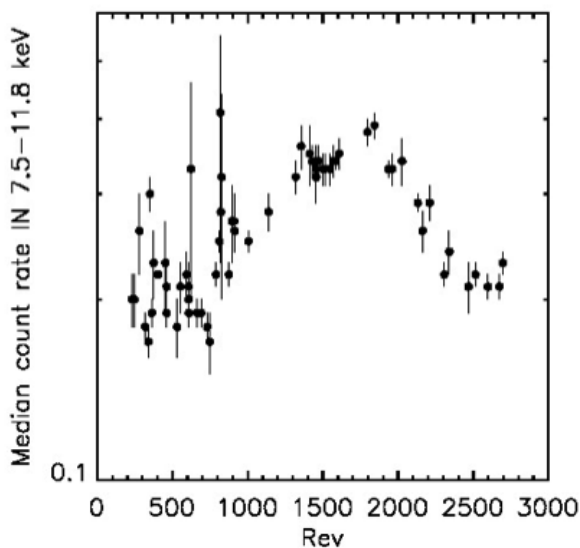


Figure 8.4: Median count rate over the all field of view of the available MOS2 closed observation.

ATHENA Radiation Environment Models and X-Ray Background Effects Simulators	WP1 TN 1.1	Doc No: IASFMi-ATHENA-WP1 Date: 10 February 2017 Page: 71 of 78
---	-----------------------------	---

The same temporal behavior is seen when looking at the all set of closed observations listed in the XMM website¹³ (Figure 8.4). Outliers in the relation are due to closed observations which are scheduled at the beginning or at the end of the revolution and they are therefore affected by high energy particles trapped in the radiation belts.

The key aspect that the instrumental background is correlated with high energy particles is also reflected in a naïve correlation of the closed data median count rate and the corresponding median ERM HES0 rate during the same time interval (Figure 8.5). The ERM count rate can vary by up to two orders of magnitude, reflecting the high spectral variability of SEPs and particles in the radiation belts, however the instrumental background varies at most by a factor of 2.

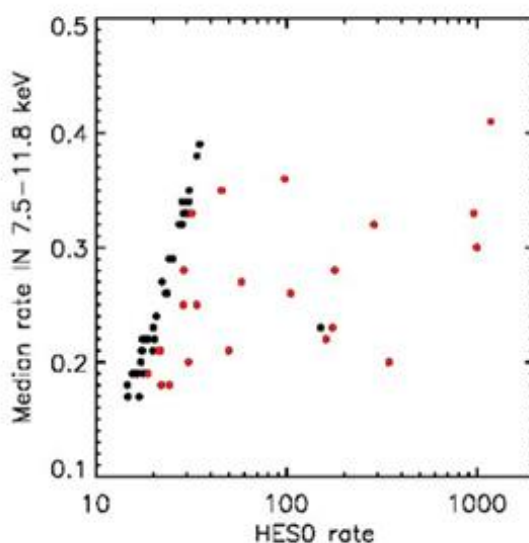


Figure 8.5: Correlation of the ERM HES0 count rate and the corresponding median rate over the all *inFOV* for closed observations. The black points show the expected correlation when the HES0 rate is representative of the GCR flux. Red points are selected when filtering for SEPs or radiation belts passage as detailed in the following section.

8.3 Filtering out SEPs and radiation belts

In order to obtain a consistent comparison of the count rate in the two instruments, it is therefore necessary to filter periods of radiation belts passages and SEPs events. The former is obtained by fitting the histogram of the counts with a Gaussian and excluding time periods above 3σ from the mean, in a similar fashion as filtering soft proton flares in the light curves of EPIC observations.

¹³ <http://www.cosmos.esa.int/web/xmm-newton/filter-closed>

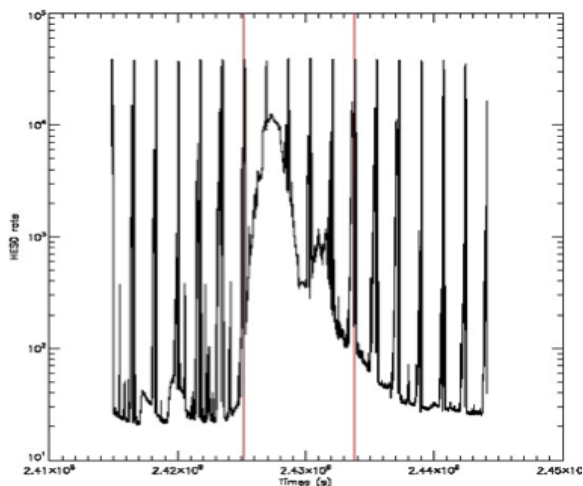


Figure 8.6: ERM HES0 count rate during several XMM orbits showing the time interval flagged as SEP shown by the vertical red lines. Clearly there is some residual high flux left in the declining tail of the flare.

The latter has been obtained by using the SEP events list found on the ESA Solar Energetic Particle Environment Modelling (SEPTEM) application server (http://dev.sepem.oma.be/help/event_ref.html). The time duration of the SEP event in the list is usually conservative, even though sometime this is not true and leads to low residual level of outliers (see an example in Figure 8.6).

8.4 Correlation of ERM and *outFOV* MOS2 data

When the ERM data are thus filtered, the correlation is evident and also the time behaviour is perfectly consistent, see Figure 8.7. The plots correspond to 71.5 Ms worth of data. It's also worth noting the striking qualitative similarity with the Chandra ACIS-S3 background of Figure 8.2, which reinforces the

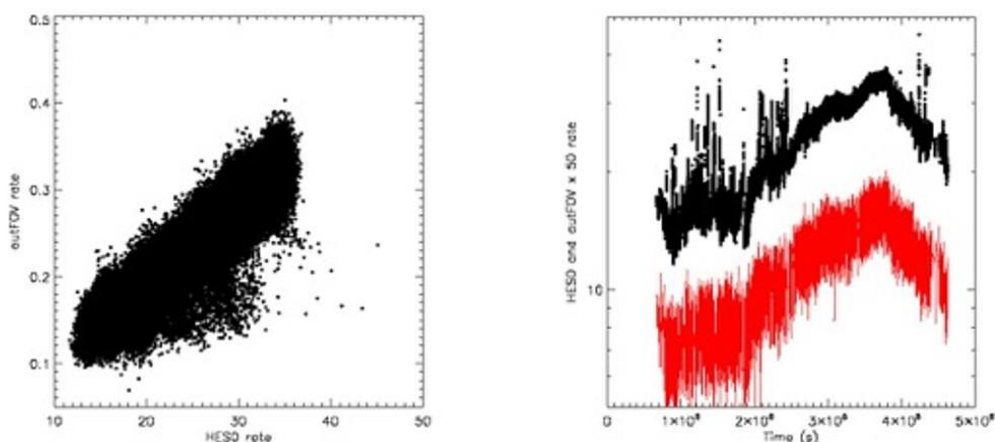


Figure 8.7: *Left panel*: plot showing the correlation between ERM HES0 count rates and the corresponding *outFOV* count rate. A clear correlation is present. *Right panel*: time resolved behavior of the ERM HES0 count rate (black) and the EPIC-MOS2 *outFOV* data (red).

ATHENA Radiation Environment Models and X-Ray Background Effects Simulators	WP1 TN 1.1	Doc No: IASFMi-ATHENA-WP1 Date: 10 February 2017 Page: 73 of 78
---	-----------------------------	---

idea of a common GCR rays origin for the unfocused particle background of CCD detectors in similar orbits.

8.5 Absence of correlation with the magnetospheric environment

The absence of correlation with magnetospheric environment is yet another evidence of the GCR origin of the particle component creating the unfocused particle background in EPIC. The plot shown in Figure 8.8 reports the mean of the *outFOV* rate as a function of the distance from Earth, colour-coded according to the definitions of magnetospheric environments in Section 4.3.1 (see Figure 4.1). There is no indication of a dependence on the magnetospheric environment: the low rates when the XMM satellite is outside of the bow shock are simply due to the fact that the satellite probed this magnetospheric regime at the beginning of the mission, when solar activity was high and therefore the GCR flux and its induced particle background was low.

8.6 The mechanism responsible for the instrumental background

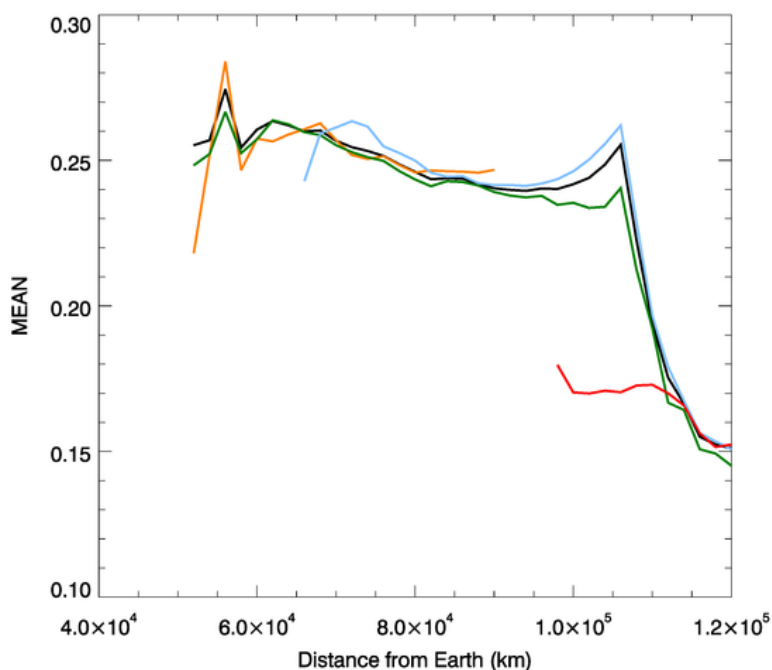


Figure 8.8: Mean count rate as a function of Distance from Earth of the *outFOV* count rate, color coded according to the different magnetospheric regimes defined in Figure 4.1

We provided evidence that the EPIC MOS2 instrumental background is clearly correlated with the flux of GCR, as modulated by the solar cycle. Correlation however is not causation: relying on established understanding based on Geant 4 simulation [e.g. Hall et al. 2008], the main elements of the background are knock-on electrons ejected by the high energy GCR protons (100-400 MeV).

9 UPRD: RADIATION DAMAGE BY UNFOCUSED PARTICLES

9.1 Introduction

The aim of the UPRD sub-WP is to study radiation damage caused by high-energy (tens-hundreds of MeV) particles interacting with X-ray detectors without being focused by the mirrors. Charged particles may displace atoms in the silicon lattice of the current generation of X-ray detectors, creating electron “traps” which increase Charge Transfer Inefficiency (CTI), resulting in position-dependent energy scale and in the loss of spectral resolution and quantum efficiency. This discussion complements the one in SPRD sub-WP (Section 0) where we discussed the radiation damage caused by soft protons focused by the mirrors. We base our analysis on the experience of X-ray detectors that have already flown in space, concentrating mainly on the EPIC CCDs on board XMM-Newton.

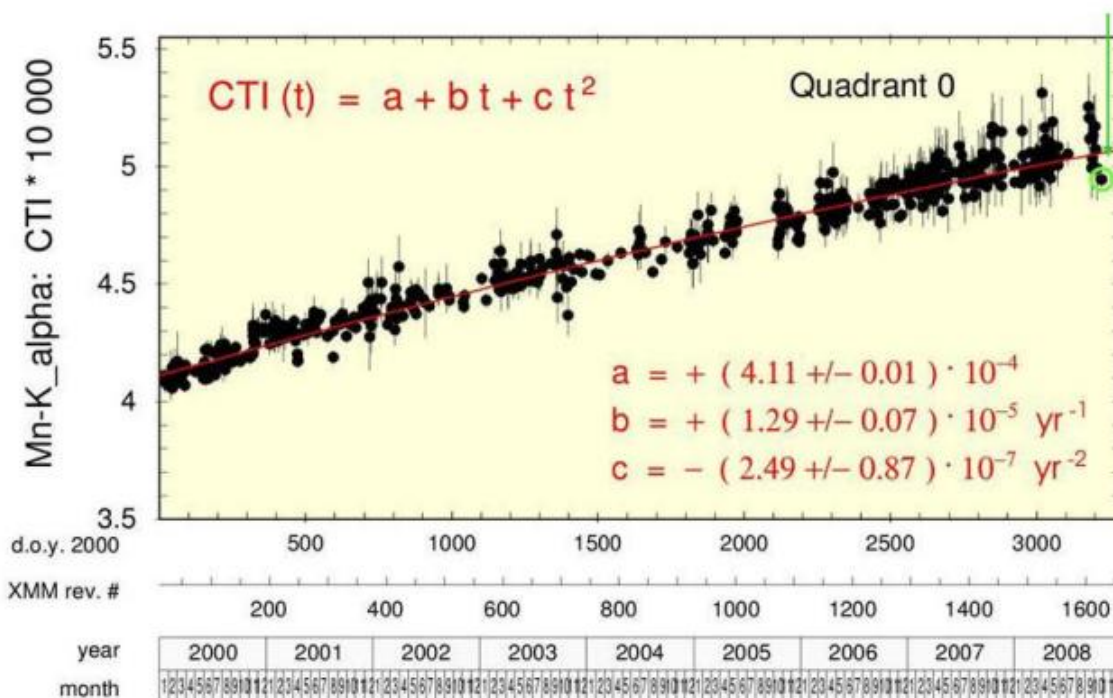


Figure 9.1: CTI monitoring in the EPIC pn detectors using the Mn K_{α} (5.896 keV) calibration line: its increase in time is described with a linear growth rate of $1.29 \cdot 10^{-5}$ per year with a small quadratic correction. From Meidinger (2016).

9.2 Radiation Damage in XMM-Newton detectors

In Figure 6.2, we show the monitoring of the CTI in one of the front-illuminated MOS CCDs in the first years of the mission by the XMM-Newton EPIC team [Altieri et al. 2004]. We discussed in Section 0 that part of the damage could be due to low-energy protons, as estimated from ground tests. However, the CTI curve in Figure 6.2, also shows some sudden increases associated to SEP events due to



powerful coronal mass ejections (such as the 2000 Bastille Day Solar flare around revolution 110, Altieri et al. 2004). This highlights that SEPs investing the satellite can cause a significant and sudden increase in the CTI, and contribute to the radiation damage of the detectors.

In the back-illuminated EPIC pn detector, the CTI increase since launch is entirely due to unfocused energetic particles, since soft protons lose all their energy before reaching the transfer channel (Section 0), which is located relatively far away from the surface, deep in the silicon bulk.

The EPIC pn team monitored continuously the CTI of the CCDs: Meidinger et al. (2004) found that in the early years (1999-2003) it increased linearly with a rate of $1.3 \cdot 10^{-5}$ per year, i.e. a 3.2% degradation per year with respect to the starting CTI value (due to fabrication defects) of $4.1 \cdot 10^{-4}$. This degradation rate has decreased only slightly with time, because of the solar cycle, and remained almost constant as shown in Figure 9.1 [Meidinger 2016], where the CTI evolution is fitted with a linear degradation of $1.29 \cdot 10^{-5}$ per year, with a small (10^{-7}) quadratic correction. The overall CTI is consistent with pre-launch expectations [Meidinger et al. 1998, 2000], which estimated the total radiation damage experienced by the detector in 10 years to be equivalent to a 10 MeV proton fluence of about $5 \cdot 10^8 \text{ cm}^{-2}$.

Periodic observations with the calibration sources can be used to correct the effects of the CTI on the scientific analysis of XMM-Newton data. However, the statistical nature of charge transfer losses results in a small degradation of the energy resolution by about 1 eV per year [Meidinger et al. 2004].

An unexpected damage that occurred to the EPIC CCDs is the impact with micrometeoroids, which caused the loss of two CCDs in the MOS1 camera and a few bright pixels in the EPIC pn chips. However, this kind of damage is not due to charged particles but most likely to fragments scattered on the focal plane after a micrometeoroid impact on the telescope [Pfeffermann et al. 2004]. This damage is potentially an issue for future telescopes with larger effective area such as Athena, and mitigation strategies are currently under study for the WFI camera [Meidinger 2016].

9.3 Conclusions

The continuous monitoring of the performances of the current generation X-ray detectors have shown that they suffered radiation damage due to charged particles. In particular, the XMM-Newton EPIC pn CCDs are not affected by soft protons focused by the mirrors and only damaged by high-energy penetrating particles. The performances of the pn have been continuously monitored by the instrument team and their degradation is consistent with the CTI increase expected before launch. We have no evidence of other effects due to charged particles on X-ray CCDs besides CTI, which should not be an issue for Athena detectors as they do not transfer charges.



10 SUMMARY

The main findings presented in this report may be summarized as follows

- Sub-WP SPB1: contrary to what was previously believed, the low intensity component is not associated to soft protons! This amounts to a shift in paradigm in our understanding of the EPIC background with significant consequences both for XMM-Newton & Athena. As an example, we point out how some of the ATHENA level 2b requirements for the soft proton background were expressed in terms of the quiescent soft proton component. Now we know that this component is not associated to soft protons and these requirements will have to be revisited.
- Sub-WP SPB2: Dependence of the soft proton rate on magnetospheric environment is modest if any. Conversely we find evidence of an anti-correlation of soft proton intensity with distance from the Earth and of some difference between the “front” side of the magnetosphere, i.e. the one exposed to the sun, and the tail side.
- Sub-WP SPB3: There is no clear correlation between the soft proton flux measured by ACE in L1 and the XMM inFOV-outFOV count rate. Therefore the datasets investigated in this analysis are not sufficient to reach our final goal of measuring the concentrating power of XMM optics. A measurement of the soft proton flux needs to be performed in a location as close as possible to that of XMM at that specific time: datasets from satellite within the magnetosphere, such as Cluster, may prove to be valuable for this analysis. Moreover, information on EPIC observing direction should be included when executing such a comparison.
- Sub-WP UPB1: X-ray mission in High Earth Orbit (HEO) all show a modulation of the intensity of the high-energy particle background with Solar Cycle.
- Sub-WP UPB2: We have found: 1) a clear correlation of the EPIC high-energy particle induced background with radiation monitor data and 2) a clear anti-correlation of the EPIC high energy particle induced background with the solar cycle. Both these finding support the hypothesis of high energy cosmic ray protons as the ultimate source for this type of background.
- Sub-WPs SPRD and UPRD: Analysis of soft proton and high-energy particle induced radiation damage reveals that the only measured effects on X-ray CCDs are those on the CTI. This should not be an issue for Athena detectors as they do not transfer charges.



11 REFERENCES

- Abbey et al, Proceedings of 6th European conference on Radiation and its effects on components and systems, (2001)
- Altieri et al, MmSAI, 75, 559 (2004)
- Ambrosi et al, Nuclear Instruments and Methods in Physics B207, 175 (2003)
- Campana et al, Experimental Astronomy, 36, 451 (2013)
- Carter and Read, A&A, 464, 1155 (2007)
- De Luca and Molendi, A&A, 419, 837 (2004)
- Escoubet et al, Space Sci. Rev, 79, 11 (1997)
- Fränz and Harper, P&SS, 50, 217 (2002)
- Freeland and Handy, Solar Phys. 182, 497 (1998)
- Gold et al, Space Sci. Rec. 86, 541 (1998)
- Grant et al, Proc. SPIE, 4851, 140 (2003)
- Grant et al, Proc. SPIE, 5898, 201 (2005)
- Grant et al, Proc. SPIE, 8443, article id 844311 (2012)
- Haggerty et al, Advances in Space Research, 105, 25123 (2000)
- Haggerty et al, Advances in Space Research, 38, 995 (2006)
- Hall et al, SPIE Conference Series, 7021, article id 70211Y (2008)
- Hathaway et al, Living Reviews in Solar Physics, 7, 1 (2010)
- Kendziorra et al, Proc. SPIE, 4140, 32 (2000)
- Krivonos et al, A&A, 463, 957 (2007)
- Kuntz and Snowden, A&A, 478, 575 (2008)
- Leccardi and Molendi, A&A, 486, 359 (2008)
- McIlwain, J. Geophys. Res., 66, 3681 (1961)
- Meidinger, IEEE Transaction on Nuclear Science, 45, 2849 (1998)
- Meidinger, Schmalhofer and Struder, NIM, A439, 2-3, 319 (2000)
- Meidinger et al, MmSAI, 75, 551 (2004)
- Meidinger, presentation at AHEAD Background Meeting 2016,
<https://file.sic.rm.cnr.it/index.php/s/cU2VuVpoaSZQAqr>, (2016)
- Moretti et al, A&A, 493, 501 (2009)
- Murakami et al, SPIE Conference Series, 6266, article id 62662Y (2006)



ATHENA Radiation Environment
Models and X-Ray Background
Effects Simulators

WP1
TN 1.1

Doc No: IASFMi-ATHENA-WP1
Date: 10 February 2017
Page: 78 of 78

Pfeffermann et al, MmSAI, 75, 555 (2004)

Prigozhin et al, Proc. SPIE 4140, 123 (2000)

Read et al, A&A, 534, 34 (2011)

Rosenqvist et al, Atmos J Solar - Terrestrial Physics, 64, 721 (2002)

Smith et al, Proceeding of the SPIE, 7732, article id 773246 (2010)

Stone et al, Space Sci. Rev. 86, 1 (1998)

Struder et al, A&A, 365, 18 (2001)

Tawa et al, PASJ, 60, 11 (2008)

Tessein et al, ApJ, 812, 68 (2015)

Tiengo "Reduction of soft protons background in Symbol-X:effect of thermal blankets and magnetic diverter", SX-IASFMI-TN-0001 Tech. Report (2007)

Turner et al, A&A 365 27 (2001)